

A Thesis Submitted for the Degree of PhD at the University of Warwick

Permanent WRAP URL:

<http://wrap.warwick.ac.uk/135409>

Copyright and reuse:

This thesis is made available online and is protected by original copyright.

Please scroll down to view the document itself.

Please refer to the repository record for this item for information to help you to cite it.

Our policy information is available from the repository home page.

For more information, please contact the WRAP Team at: wrap@warwick.ac.uk

**THE ELECTRICAL CHARACTERISATION
OF
Si AND Si/Si_{1-x}Ge_x/Si STRUCTURES
GROWN BY
MOLECULAR BEAM EPITAXY**

By

James Cordeaux Brighten BSc (Hons.)

*Thesis submitted in partial fulfilment
of the requirements for the Degree of
Doctor of Philosophy
of the
University of Warwick*

**Physics Department
University of Warwick**

July 1993

Dedicated to my Parents

"Scientists and Artists perpetually live on the edge
of mystery, always being surrounded by it."

J. Robert Oppenheimer

ABSTRACT

Si/Si_{1-x}Ge_x strained layer heterostructures offer great promise for applications in field-effect and bipolar devices; however, their usefulness depends on a knowledge of the purity and perfection of both the bulk and heterointerfacial regions. Very little work has been published on the characteristics of the Si/Si_{1-x}Ge_x heterointerface via electrical means, the practice to date being to fabricate devices and indirectly assess the interface via the quality of the device characteristics. The present work has focused on the direct electrical characterisation of Si and Si/Si_{1-x}Ge_x/Si layers grown by Molecular Beam Epitaxy (MBE), in order to investigate the band offset at the Si/Si_{1-x}Ge_x heterointerface and electrically active centres in both the bulk and heterointerfacial regions.

Sputtered Ti Schottky barriers were found to provide suitable rectifying barriers for electrical measurements on the MBE layers. Current-Voltage (I-V) characteristics revealed excessive reverse leakage currents in early work carried out; this was attributed to metallic contamination located preferentially in the alloy region. The use of liners around the Si and Ge charges reduced the in-diffusion of metallics and dramatic improvements were found in the material quality as observed from the I-V characteristics. The large extracted barrier heights from C-V measurements reflected the stability and reproducibility of the Schottky contacts and provided rectifying barriers of sufficient quality to access the bulk epilayers via depletion-capacitance techniques.

Capacitance-Voltage (C-V) profiling allowed heterojunction features in the apparent free carrier distribution to be observed, for the first time, in Si/Si_{1-x}Ge_x/Si layers for $0 < x \leq 0.2$. Numerical integration of these profiles allowed valence band offsets to be extracted which were in good agreement with those predicted theoretically. The effects of traps on C-V measurements were observed in Si and Si/Si_{1-x}Ge_x/Si layers; considerable carrier compensation was apparent, occurring to a greater extent in the alloy layers. Use of C-V simulations allowed the reconstruction of apparent free carrier distributions, using the extracted valence band offset, interface charge density and trap distributions (the latter determined by Deep Level Transient Spectroscopy (DLTS)) as input parameters; simulations were also used to assess the validity of the experimentally determined heterojunction parameters in the presence of interfacial traps.

DLTS studies were used to determine the distribution and nature of deep states in both Si and Si/Si_{1-x}Ge_x/Si structures. Well defined deep level peaks were observed in the bulk Si and Si_{1-x}Ge_x regions whilst distortion occurred to the spectra in the Si/Si_{1-x}Ge_x heterointerfacial region. This latter distortion is attributed to the significant band bending that occurs in this region. Apparent trap concentrations increased with Ge composition and also showed an increase in the Si_{1-x}Ge_x as compared to the Si regions. Broadening of the deep level spectra was investigated via simulation in terms of carrier emission from a band of energies in the band-gap and allowed a correction to the underestimated trap concentrations. The donor-like nature of the well defined features, determined from the logarithmic filling and field-independent behaviour and their dependence on growth temperature and anneal, suggested the origin of the electrical activity could lie with point defect/dislocation interactions. Structural analysis carried out on the structures investigated here indicated the presence of Fe and O; it is considered that both impurities, in point defect form, could interact with the threading and misfit dislocations present to produce the electrical activity observed.

CONTENTS

ABSTRACT		i
CONTENTS		ii
TABLES AND FIGURES		v
ACKNOWLEDGEMENTS		x
DECLARATION		xi
CHAPTER 1	INTRODUCTION	1
	REFERENCES	6
CHAPTER 2	BAND STRUCTURE ENGINEERING: THE INCORPORATION OF Ge INTO Si	
2.1	INTRODUCTION	8
2.2	BAND STRUCTURE AND BAND ALIGNMENTS	8
2.3	RELAXATION MECHANISMS	11
2.4	GROWTH CONSIDERATIONS	14
2.4.1	GROWTH MODE	15
2.4.2	DEFECTS IN Si AND SiGe MBE LAYERS	17
2.4.2.1	IMPURITY INCORPORATION	17
2.4.2.2	STRUCTURAL DEFECTS	20
2.5	ELECTRONIC PROPERTIES OF IMPURITIES AND DEFECTS	20
	REFERENCES	25
CHAPTER 3	THEORETICAL AND EXPERIMENTAL CONSIDERATIONS	
3.1	INTRODUCTION	29
3.2	ELECTRICAL CHARACTERISATION	29

3.2.1	THE SCHOTTKY BARRIER	29
3.2.2	CURRENT TRANSPORT MECHANISMS	31
3.2.3	CAPACITANCE-VOLTAGE PROFILING	33
3.2.3.1	DEPLETION CAPACITANCE	33
3.2.3.2	DOPING PROFILES	35
3.2.3.3	TRAPPING STATES	37
3.2.3.4	HETEROJUNCTIONS	41
3.2.3.5	SIMULATIONS	44
3.2.4	DEEP LEVELS	45
3.2.4.1	CARRIER KINETICS	45
3.2.4.2	TRANSIENT RESPONSE	46
3.2.4.3	CAPACITANCE TRANSIENTS	48
	AND DEEP LEVELS	
3.2.4.4	DEEP LEVEL TRANSIENT SPECTROSCOPY	49
3.2.4.5	MAJORITY CARRIER CAPTURE	51
3.2.4.6	LIMITATIONS	52
3.2.5	LAYER GROWTH AND	53
	EXPERIMENTAL SET-UP	
3.3	STRUCTURAL ANALYSIS	54
3.3.1	TRANSMISSION ELECTRON MICROSCOPY	54
3.3.2	DEFECT REVEAL ETCH TECHNIQUES	55
3.3.3	X-RAY DIFFRACTION	55
	REFERENCES	56
 CHAPTER 4	 CARRIER DISTRIBUTIONS IN SI AND SiGe	
4.1	INTRODUCTION	58
4.2	C-V DETERMINED APPARENT FREE	58
	CARRIER DISTRIBUTIONS	
4.3	AN ASIDE: THE SCHOTTKY BARRIER	62

4.4	EXPERIMENTAL RESULTS	65
4.5	DISCUSSION	68
	REFERENCES	85
CHAPTER 5	DEEP LEVEL DISTRIBUTIONS IN Si AND SiGe	
5.1	INTRODUCTION	87
5.2	DEEP LEVELS IN Si, SiGe AND III-V ALLOY SYSTEMS	87
5.3	EXPERIMENTAL RESULTS	93
5.4	STRUCTURAL AND CHEMICAL ANALYSIS	98
5.5	DEEP LEVEL MODELLING	100
5.6	DISCUSSION	110
	REFERENCES	125
CHAPTER 6	CONCLUSIONS AND FUTURE WORK	128
APPENDICES		132

TABLES AND FIGURES

TABLES

	On or after page
4.1 Extracted band offsets and interface charge densities according to Fig 4.13a-c	72
4.2 Extracted band offsets and interface charge densities according to Fig 4.14a-c	75
5.1 Extracted broadening parameters (from model II.) for the -1/-2V measurement window from sample #28/17	107
5.2 Extracted broadening parameters for deep level spectra from sample #28/17	109
5.3 Deep level lineshape broadening	113
5.4 Deep level parameters for states A, B, C and D compared to previously published work	121

FIGURES

1.1 Energy band diagram for a P-p isotype heterojunction	1
1.2 Energy band diagram for a P-p isotype heterojunction in the presence of interfacial charge	3
2.1a Bandstructure of Silicon	8
2.1b Bandstructure of Germanium	8
2.2 Schematic illustrating lattice matching	9
2.3 Calculated strain-induced band-gap reduction	9
2.4 Band line-ups for various strained Si/Si _{1-x} Ge _x couples	10
2.5 Schematic of lattice mismatch	11
2.6 Strained layer critical thickness	12
2.7 Schematic of an MBE system	14
2.8 Ideal growth conditions for Si _{1-x} Ge _x on Si	16

FIGURES	On or after page
2.9 Band bending due to a repulsive coulomb potential	22
3.1 Schottky barrier formation	29
3.2 Equivalent circuit representation	37
3.3a Energy band diagram for a uniform acceptor trap distribution	37
3.3b Energy band diagram for a uniform donor trap distribution	37
3.4 Influence of uniform and non-uniform trap distributions on the apparent free carrier profile	40
3.5a Energy band diagram for a P-p isotype heterojunction	41
3.5b Band bending for two reverse bias situations for a P-p isotype heterojunction	41
3.5c Carrier removal in the vicinity of the heterojunction for an incremental reverse bias, ΔV_R	41
3.5d True and apparent hole carrier distributions in the vicinity of the heterojunction	41
3.6 Carrier transitions between deep levels and band edges	45
3.7a Energy band diagram for the fill bias, V_{FILL}	47
3.7b Trap occupancy for V_{FILL} and V_{REV} applied biases	47
3.7c Energy band diagram for the reverse measurement bias, V_{REV}	47
3.8 Illustration of the DLTS boxcar integrator response	50
3.9 Sample schematic diagrams	53
4.1a Interface charge density and conduction band offset for an InGaAs/InP heterostructure	59
4.1b Apparent free carrier profiles for the InGaAs/InP heterostructure	59

FIGURES

	On or after page
4.2 Non-ideal and improved Schottky characteristics for Si/Si _{1-x} Ge _x /Si heterostructures	62
4.3 Schottky reverse characteristics illustrating a) leakage current and b) depletion capacitance	63
4.4 Apparent free carrier distributions for sample #24/21	66
4.5 Apparent free carrier distributions for sample #28/20	66
4.6 Apparent free carrier distributions for sample #28/17	66
4.7 Apparent free carrier distributions for sample #24/27	67
4.8a Extracted valence band offsets for various Ge compositions	67
4.8b Extracted interface charge densities for various Ge compositions	67
4.9 Apparent free carrier distributions for sample #28/16	67
4.10 Apparent free carrier distributions for sample #24/19	67
4.11 Matching of simulated and experimental apparent free carrier distributions for sample #24/21	69
4.12 Matching of simulated and experimental apparent free carrier distributions for sample #28/20	70
4.13 Simulated apparent free carrier distributions for traps positioned at the heterojunction	71
4.14 Simulated apparent free carrier distributions for an asymmetric trap distribution at the heterojunction	74
4.15 Matching of simulated and experimental apparent free carrier distributions for various Ge compositions: extracted interface charge positioned at the heterointerface for the simulations	76

FIGURES

	On or after page
4.16 Matching of simulated and experimental apparent free carrier distributions for various Ge compositions: extracted interface charge asymmetrically positioned at the heterointerface for the simulations	77
4.17 Matching of simulated and experimental apparent free carrier distributions for sample #28/17 incorporating bulk traps	79
4.18a Measured device capacitance versus temperature	82
4.18b Measured device conductance at the transition temperature	82
4.18c Measured device capacitance at the transition temperature	82
5.1 Typical deep level spectra for sample #24/21	93
5.2 Arrhenius plot of the well defined deep levels for sample #24/21	93
5.3 Apparent deep level distributions for sample #24/21	94
5.4 Apparent deep level distributions for sample #28/20	94
5.5 Logarithmic filling behaviour for deep levels A, B and C	94
5.6 Deep level spectra following annealing treatment of sample #24/21	94
5.7 Typical deep level spectra for sample #28/17	95
5.8a Apparent deep level distributions for sample #24/19	96
5.8b Apparent deep level distributions for sample #28/15	96
5.8c Apparent deep level distributions for sample #28/16	96
5.8d Apparent deep level distributions for sample #28/17	96
5.8e Apparent deep level distributions for sample #28/22	96
5.9 Logarithmic filling behaviour for deep levels A, B and D	98
5.10 X-ray rocking curves for strained and relaxed Si/Si _{1-x} Ge _x /Si structures	98

FIGURES

	On or after page
5.11 Defect counts from defect etched material	99
5.12 TEM micrographs for strained and relaxed Si/Si _{1-x} Ge _x /Si structures	99
5.13a Variation in trap occupancy	101
5.13b Energy band diagram according to model I.	101
5.14 Simulated and experimental match for the well defined deep level spectra from sample #28/17 (from model I.)	104
5.15 Gaussian distribution broadening according to model II.	105
5.16 Weighted deep level spectral broadening	106
5.17 Simulated and experimental match for the well defined deep level spectra from sample #28/17 (from model II.)	107
5.18 Simulated and experimental match for the distorted deep level spectra from sample #28/17 (from model II.)	108
5.19 Band bending in the vicinity of the valence band discontinuity	116
5.20 Experimentally determined coulomb potentials for the deep levels A, B and D	117
5.21 Band bending associated with the coulomb potential	117

ACKNOWLEDGEMENTS

I would like to thank Dr T. E. Whall and Prof. E. H. C. Parker for their support and guidance throughout the period of my doctoral research.

Furthermore, thanks are due to both Prof. A. R. Peaker and Prof. B. Hamilton for extended use of facilities at UMIST. I am particularly indebted to Dr. I. D. Hawkins (UMIST) for guidance and discussions throughout all of this work.

I would like to acknowledge the work carried out on my behalf by Dr. R. A. A. Kubiak and Dr. P. J. Phillips (Warwick) for the MBE layer growth, Dr. S. M. Newstead (Warwick) for X-ray characterisation and Dr. P. D. Brown (University of Cambridge) for TEM measurements.

I also thank all members, past and present, at both the University of Warwick and UMIST who have helped during the period of this work.

Last, but not least, I thank my parents and Meriam for their never-ending support and encouragement throughout this work.

DECLARATION

This thesis is submitted to the University of Warwick in support of my application for the degree of Doctor of Philosophy. It contains an account of my own research work carried out in the Department of Physics at the University of Warwick and the Department of Electrical Engineering and Electronics at UMIST between October 1988 and July 1993.

The work presented in this thesis is the result of my own research except where specifically stated in the text and preceding acknowledgement.

Much of this work has been or is in the process of being published and includes:

"The Electrical assessment of p-isotype Si/SiGe/Si heterostructures grown by MBE"

J. C. Brighten, I. D. Hawkins, A. R. Peaker, R. A. Kubiak, P. J. Phillips, T. E. Whall and E. H. C. Parker Thin Sol. Films 222 (1992) 116

"The determination of valence band discontinuities in Si/Si_{1-x}Ge_x/Si heterojunctions by Capacitance-Voltage techniques"

J. C. Brighten, I. D. Hawkins, A. R. Peaker, E. H. C. Parker and T. E. Whall

J. Appl. Phys. 74 (1993) (to be published 1.8.93)

"The determination of valence band discontinuities and interface charge densities in Si/Si_{1-y}Ge_y/Si heterojunctions"

J. C. Brighten, I. D. Hawkins, A. R. Peaker, R. A. Kubiak, E. H. C. Parker and T. E. Whall Semicond. Sci. Technol. 8 (1993) 1487

"Deep Level Transient Spectroscopic investigations of Boron-doped Si and Si/Si_{1-x}Ge_x/Si layers grown by MBE"

J. C. Brighten, I. D. Hawkins, A. R. Peaker, R. A. Kubiak, E. H. C. Parker and T. E. Whall (to be presented at the International conference on Solid State Devices and Materials, Japan August 28 - September 1, 1993)

"Characterisation of Si/Si_{1-x}Ge_x/Si heterostructures by capacitance-transient spectroscopy"

J. C. Brighten, I. D. Hawkins, A. R. Peaker, R. A. Kubiak, E. H. C. Parker and
T. E. Whall (submitted to J. Appl. Phys.)

CHAPTER 1

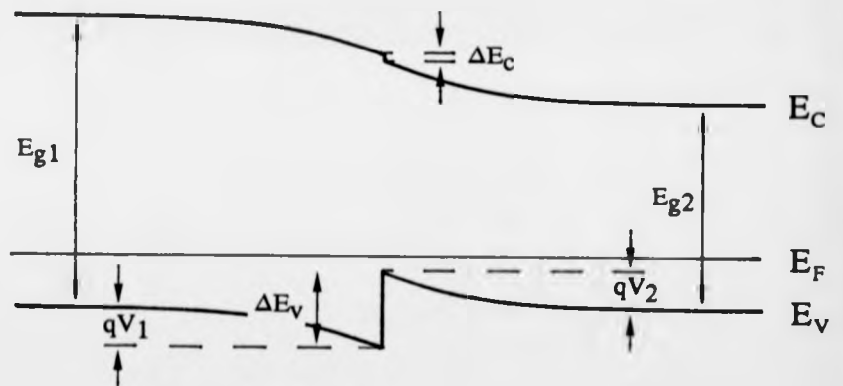
INTRODUCTION

The importance of the incorporation of heterointerfaces into high performance semiconductor devices has long been recognised [1.1] and has met with considerable success in the III-V compound material system [1.2-4]. The move into the high performance realm has involved minimising the non-active part of the device volume to the extent that the device turns from a collection of semiconductor regions separated by interfaces into a collection of interfaces separated by minimal semiconductor layer thicknesses. This vividly illustrates the importance of the heterointerface and has led to considerable flexibility in device design through the ability to engineer the band structure and band alignments by changing material parameters.

From the device physics viewpoint, the most important aspect of the heterointerface (and possibly the point of departure for many real situations!) is the energy band diagram at the join between the two dissimilar band-gap materials. In a homojunction, the energy gap does not vary across the junction (ignoring band-gap narrowing due to high doping levels) and so the conduction and valence bands are continuous. However, in a heterostructure combining two different semiconductor materials, an abrupt transition ie. over only a few monolayers may be considered to occur in the band alignment. This is shown for the hypothetical case of a P-p isotype heterojunction in Fig 1.1, in which the main discontinuity occurs in the valence band edge. The offset is assumed to be a characteristic property of the semiconductor pair, independent of doping level but possibly dependent upon crystallographic orientation and exact atomic arrangement at the interface. Far from the interface, the band edges are governed by the requirement of electrical neutrality which fixes their position with respect to the Fermi level; at the heterointerface, transfer of free charge carriers from

Fig 1.1

Energy band diagram for a P-p isotype heterojunction. The major band offset occurs in the valence band and is denoted by ΔE_v ; ΔE_c is minimal and the conduction band is almost continuous across the heterointerface. E_{g1} and E_{g2} denote the wide and narrow band-gaps respectively whilst the built-in potential associated with the heterojunction dipole is given by $V_1 + V_2$.



the wide band-gap semiconductor into the well on the narrow band-gap side induces the band bending shown and creates a charge dipole across the heterojunction. Such potential barriers and associated dipoles can combine with potentials created by non-uniform doping and applied bias to significantly influence carrier transport both perpendicular and parallel to the heterointerface.

Whilst such III-V compound semiconductors have recently been shown to excel over Si in terms of high speed and optical applications, both the material and electronic properties of Si maintain its dominance in current VLSI technology. Clearly, the advantages to be gained from the matching of compound semiconductors to Si are great and this has generated considerable work in recent years as reviewed by Bean [1.5]. Problems with crystallographic or chemical incompatibility have limited the possible alloys which could be used; of these, the strained layer $\text{Si}_{1-x}\text{Ge}_x$ material system shows most promise.

Although chemically compatible, the difference in lattice constant between Si (0.357nm) and Ge (0.357nm) requires strained layer growth to achieve coherent lattice matching between Si and $\text{Si}_{1-x}\text{Ge}_x$; whilst the difference in lattice constants places a restriction on the thickness to which layers may be grown before strain relief occurs, the effects of strain on band structure and band alignments at the Si/ $\text{Si}_{1-x}\text{Ge}_x$ heterointerface indicate great potential for this material system [1.5, 1.6].

Work by Smith *et al.* [1.7] and Won *et al.* [1.8] predicted enhanced performance over conventional Si Bipolar Junction Transistors (BJTs) using a strained $\text{Si}_{1-x}\text{Ge}_x$ base region in a Heterojunction Bipolar Transistor (HBT) structure; this was demonstrated in extensive work that followed [1.9-11] and promises to match or even surpass III-V HBT device capabilities.

The modulation doping experiments of People *et al.* [1.12] and Abstreiter *et al.* [1.13] prompted work into p- and n-channel $\text{Si}_{1-x}\text{Ge}_x$ Modulation doped Field Effect Transistors (MODFETs) [1.14, 1.15]. p-channel devices gave performances comparable to state-of-the-art Si MOSFETs; further work on similar modulation doped

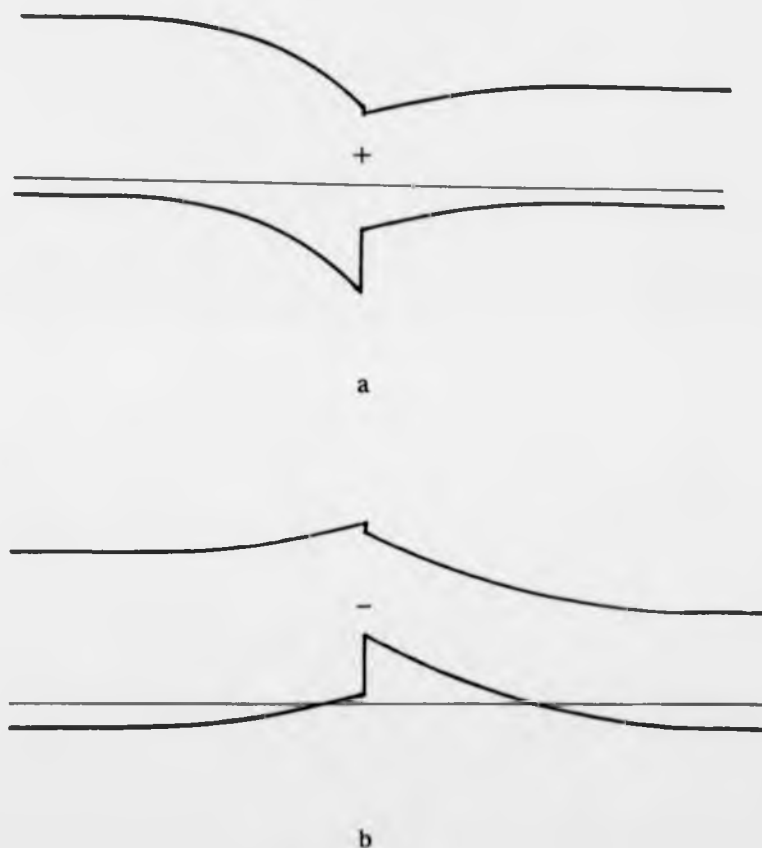
structures has indicated substantial enhancements in carrier mobilities parallel to the heterointerface for both confinement of holes [1.16, 1.17] and electrons [1.18, 1.19].

Although the realisation of practical light-emitting devices is hindered by the indirect band-gap of both Si and $\text{Si}_{1-x}\text{Ge}_x$ layers, the strain-induced reduction in $\text{Si}_{1-x}\text{Ge}_x$ band-gap and large refractive index makes this system suitable for waveguide detectors [1.20, 1.21]. Work has been carried out to investigate efficient light-emitting sources and includes zone-folding in short period superlattices [1.22], doping with rare earths [1.23] and anodised porous Si [1.24]. This latter work is still in its infancy and, as yet, optical integration with Si technology has not successfully been achieved.

Further reading may be found in the reviews by Jain *et al.* [1.25] and Abstreiter [1.26].

Clearly, the quality of the heterointerface will be a major influencing factor in such structures and departures from the lattice-matched, abrupt band line-up illustrated in Fig 1.1 will have a significant effect. For lattice mismatch, band alignments become unknown quantities and the generation of heterointerfacial misfit dislocations can act to degrade device performance if the heterojunction falls within the active device region [1.27]: if, as a consequence, recombination-generation (R-G) centres are introduced, the gain of HBT devices will be reduced [1.2, 1.28, 1.29]. Furthermore, the order of lattice growth may also affect the electrical quality of the heterointerface: in-plane mobilities for Si grown on $\text{Si}_{1-x}\text{Ge}_x$ are superior to $\text{Si}_{1-x}\text{Ge}_x$ grown on Si, which is considered to be the result of surface segregation of dopant atoms [1.30]. Such imperfections may introduce charged states at the heterointerface; Fig 1.2a&b illustrate the case for the P-p isotype heterojunction in the presence of positive (+) and negative (-) interfacial charge respectively. Such a situation can lead to considerable band bending in the vicinity of the charged states, producing a double depletion effect for positive charge whilst negative charge obliterates the barrier to produce a potential well. These and other important considerations are discussed in detail by Kroemer [1.31] and Milnes [1.32].

Fig 1.2 Energy band diagrams for the P-p isotype heterojunction as considered in Fig 1.1 in the presence of: a) positive and b) negative interfacial charge.



Given the importance of achieving lattice matched $\text{Si}/\text{Si}_{1-x}\text{Ge}_x$ layers of high crystalline quality and low interfacial charge density, very little fundamental work has so far been carried out investigating basic electrical properties of this material system. Most often, the ability to produce operational devices (by far the most prolific being HBTs) has been taken as an indicator of bulk layer/heterointerfacial electrical quality; the fact remains that HBT work in the $\text{Si}/\text{Si}_{1-x}\text{Ge}_x/\text{Si}$ field has not achieved its full potential on a reproducible basis and may reflect fundamental material problems which have yet to be overcome or fully evaluated. Indeed, the upsurge of interest in deep levels in the $\text{Si}_{1-x}\text{Ge}_x$ band-gap is readily apparent from the recent literature (see section 5.2). Such levels can have a significant effect on the electrical quality of the material, compensating intentional shallow dopants and acting as trapping or R-G centres.

The purpose of this study was to investigate the electrical material quality in both Si and $\text{Si}/\text{Si}_{1-x}\text{Ge}_x/\text{Si}$ layers grown by Molecular Beam Epitaxy (MBE) using depletion capacitance techniques. Information thus obtained should allow evaluation of the valence band discontinuity and give a direct insight into the electrically active states, which could affect subsequent device performance, both in the bulk regions and in the vicinity of the heterojunction. The structure of this thesis is organised as follows:

Chapter Two describes the concept of band engineering in the $\text{Si}/\text{Si}_{1-x}\text{Ge}_x$ material system by modifications to the grown-in strain; the limitations to strained layer growth are considered. The MBE growth technique is introduced and factors influencing the $\text{Si}/\text{Si}_{1-x}\text{Ge}_x$ layer growth and unintentional defect/impurity incorporation are discussed. The different electronic properties associated with dislocation and point defect related band-gap states are also given.

Chapter Three introduces various theoretical and experimental considerations. The ability to determine apparent free carrier distributions from a measure of the reverse bias depletion capacitance is detailed, with particular emphasis on the influence of trapping states. The analysis routinely used to extract interface charge density and band

offsets from the measured apparent free carrier distributions is considered. The time-dependent occupancy of such trapping states is introduced; such changing occupancy may be observed using the Deep Level Transient Spectroscopy (DLTS) technique which allows the extraction of trap activation, concentration, spatial position and capture cross-section. Finally, structural characterisation techniques used in this work are briefly reviewed.

Chapter Four presents the first systematic investigations for extraction of valence band discontinuity and interface charge density associated with the Si/Si_{1-x}Ge_x heterojunction from Capacitance-Voltage (C-V) measurements. Good agreement with theoretically predicted band offsets were found and trends between interface charge density and Ge composition are considered. Capacitance simulations using a model designed by Hawkins (see section 3.2.3.5 [3.13]) have allowed the influence of traps on carrier profiles to be examined; reconstruction of experimental carrier profiles is also investigated.

Chapter Five presents deep level distributions in Si/Si_{1-x}Ge_x/Si layers as determined by DLTS. Distortion observed in the deep level spectra on profiling through the heterointerface is discussed in terms of the expected band bending in this region. Broadening of the spectra may also be considered in terms of carrier emission from energy bands as opposed to discrete energy levels; this is determined from modelling of the deep level spectra and has allowed broadening parameters and corrections to trap concentrations to be assessed. Trends in deep level concentrations and Ge composition are discussed; possible sources for the electrical activity are also considered.

Chapter Six summarises the conclusions of the present work and discusses possibilities for future investigations.

REFERENCES

- 1.1 H. Kroemer Proc. IEEE 70 (1982) 13
- 1.2 D. V. Morgan and A. A. Rezazadeh GEC J. Res. 6 (1988) 37
- 1.3 D. E. Kren, A. A. Rezazadeh, P. K. Rees and J. N. Tothill
Elec. Lett. 29 (1993) 961
- 1.4 Y. -K. Chen, R. N. Nottenburg, M. B. Panish,
R. A. Hamm and D. A. Humphreys IEEE Elec. Dev. Lett. 10 (1989) 267
- 1.5 J. C. Bean in "Silicon Molecular Beam Epitaxy" Vol II
Ed. E. Kasper and J. C. Bean (CRC Press, Florida 1988) Chapter 11
- 1.6 R. People IEEE J. Quant. Elec. 22 (1986) 1696
- 1.7 C. Smith and A. D. Welbourn Bipolar Circuits Tech. Meet. Dig.
Technical papers (1987) 57
- 1.8 T. Won and H. Morkoc IEEE Elec. Dev. Lett. 10 (1989) 33
- 1.9 H. Kibbel, E. Kasper, P. Narozny and H. -U. Schreiber
Thin Sol. Films 184 (1990) 163
- 1.10 C. A. King, J. L. Hoyt and J. F. Gibbons
IEEE Trans. Elec. Dev. 36 (1989) 2093
- 1.11 E. Kasper, H. Kibbel and U. König
Proc. Mat. Res. Soc. Symp. 220 (1991) 451
- 1.12 R. People, J. C. Bean and D. V. Lang J. Vac. Sci. Technol. A3 (1985) 846
- 1.13 G. Abstreiter, H. Brugger, T. Wolf, H. Jorke and H. Herzog
Phys. Rev. Lett. 54 (1985) 2441
- 1.14 T. P. Pearsall and J. C. Bean IEEE Elec. Dev. Lett. 7 (1986) 308
- 1.15 H. Daembkes, H. Herzog, H. -J. Jorke, H. Kibbel and E. Kasper
IEEE Trans. Elec. Dev. 33 (1986) 633
- 1.16 P. J. Wang, B. S. Meyerson, F. F. Fang, J. Nocera and B. Parker
Appl. Phys. Lett. 55 (1989) 2333
- 1.17 D. W. Smith, C. J. Emeleus, R. A. A. Kubiak,
T. E. Whall and E. H. C. Parker Appl. Phys. Lett. 61 (1992) 1453

- 1.18 Y. J. Mii, Y. H. Xie, E. A. Fitzgerald, D. Monroe, F. A. Thiel,
B. E. Weir and L. C. Feldman Appl. Phys. Lett. 59 (1991) 1611
- 1.19 F. Schäffler, D. Többen, H. -J. Herzog, G. Abstreiter and B. Höllander
Semicond. Sci. Technol. 7 (1992) 260
- 1.20 B. Jalai, A. F. J. Levi, F. Ross and E. A. Fitzgerald
Electronics Lett. 28 (1992) 269
- 1.21 T. L. Lin, E. W. Jones, T. George, A. Ksendzov and M. L. Huberman
Proc. Mat. Res. Soc. Symp. 220 (1991) 477
- 1.22 G. Abstreiter NATO Advanced Study Institute (1990) unpublished
- 1.23 H. Efeoglu PhD. Thesis UMIST (1992)
- 1.24 S. Gardelis, J. S. Rimmer, P. Dawson, B. Hamilton, R. A. Kubiak,
T. E. Whall and E. H. C. Parker Appl. Phys. Lett. 59 (1991) 2118
- 1.25 S. C. Jain and W. Hayes Semicond. Sci. Technol. 6 (1991) 547
- 1.26 G. Abstreiter Physics World 5 (1992) 36
- 1.27 D. B. Holt J. Phys. Colloq. C6 (1979) 189
- 1.28 T. Tatsumi, H. Hirayama and N. Aizaki Appl. Phys. Lett. 52 (1988) 895
- 1.29 H. -U. Schreiber, B. G. Bosch, E. Kasper and H. Kibbel
Electronics Lett. 25 (1989) 185
- 1.30 T. Mishima, C. W. Fredriksz, G. F. A. Van de Walle, D. J. Gravesteijn,
R. A. Van de Heuvel and A. A. Van Gorkum Appl. Phys. Lett. 57 (1990) 2567
- 1.31 H. Kroemer Surf. Sci. 132 (1983) 543
- 1.32 A. G. Milnes Sol. St. Elec. 29 (1986) 99

CHAPTER 2

BAND STRUCTURE ENGINEERING: THE INCORPORATION OF Ge INTO Si

2.1 INTRODUCTION

$\text{Si}_{1-x}\text{Ge}_x/\text{Si}$ heterosystems provide considerable flexibility in designing new devices because of the ability to vary material parameters either side of the heterojunction; this allows significant changes to be introduced in the band structure and band alignments as a result of the built-in strain associated with lattice-matched growth. Depending upon the Ge content of the alloy layers, the usefulness of strained SiGe layers necessitate two-dimensional growth, good morphology and crystalline quality, subject to the constraints imposed by the critical thickness, h_c of the alloy layer (above which the strain associated with the lattice-matched growth is relieved by the introduction of misfit dislocations). Clearly it is important to understand the structure and stability of such layers in order to discuss the electrical characterisation presented later.

Since the improved flexibility has resulted in a more complex system, this chapter will detail the concept of "band-gap engineering" and the potential problems associated with its incorporation into the Si MBE growth technique.

2.2 BAND STRUCTURE AND BAND ALIGNMENTS

The band structures for bulk, unstrained Si and Ge are shown in Fig 2.1a&b respectively. The valence band maxima at $k=0$ are composed of the four-fold degenerate ($J = \frac{3}{2}$) upper set of states and the two-fold degenerate ($J = \frac{1}{2}$) lower set of states (the latter being separated from the former by spin-orbit splitting); note the anisotropy of the bands and the associated light and heavy hole masses of the larger and

Fig 2.1a Band structure of Silicon (after [2.1]).

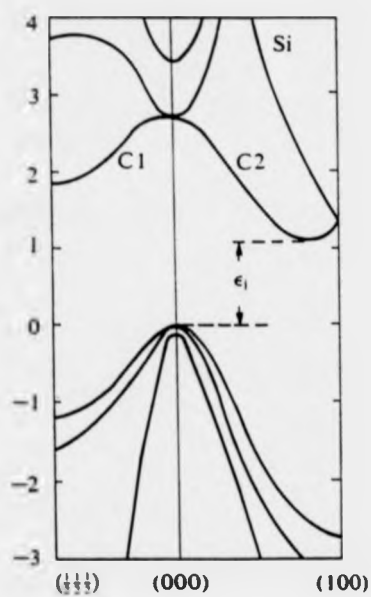
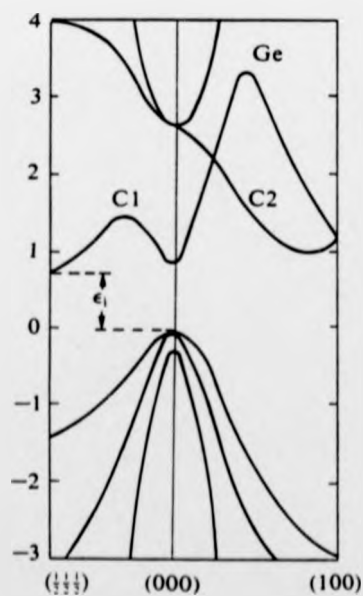


Fig 2.1b Band structure of Germanium (after [2.1]).



smaller curvature bands respectively for the upper set of states. The ellipsoidal conduction band minima are six-fold degenerate in Si and located in $\langle 100 \rangle$ directions 80% toward the X zone boundary whilst those in Ge are eight-fold degenerate and located in $\langle 111 \rangle$ directions at the L zone boundary.

Work by People [2.2] suggested a dramatic strain-induced lowering of the fundamental $\text{Si}_{1-x}\text{Ge}_x$ band-gap. For example, growth of lattice matched $\text{Si}_{1-x}\text{Ge}_x$ onto cubic $\langle 001 \rangle$ Si produced a biaxial in-plane compression (along $\langle 010 \rangle$ and $\langle 100 \rangle$ directions) and a tetragonal extension in the $\langle 001 \rangle$ growth direction as shown in Fig 2.2. The tetragonal distortion is well described by elasticity theory and, combining alloy dependent components of the strain tensor with the relevant deformation potentials, allows the shifts in band edges in the alloy to be determined. The situation considered here results in a splitting of the upper ($J = \frac{3}{2}$) states with the heavy hole state, given in the standard representation $|J, M_J\rangle$ of $|\frac{3}{2}, \pm \frac{3}{2}\rangle$, being the uppermost valence band edge; restricting the range of x to $0 < x \leq 0.75$ such that the alloy conduction band is Si-like, strain may be considered to split the six-fold degeneracy such that the lowest conduction band minima is four-fold degenerate (note these minima lie in the plane of growth in $[010], [0\bar{1}0], [100]$ and $[10\bar{0}]$ directions). People [2.2] combined these considerations with the results of Braunstein *et al.* [2.4] to obtain the strain-induced reduction in fundamental $\text{Si}_{1-x}\text{Ge}_x$ band-gap as a function of Ge composition as shown in Fig 2.3; the cross hatched region indicates the degree of uncertainty in the calculation.

Photocurrent spectroscopy measurements [2.5] showed remarkably good agreement with the work of People and suggested the main offset occurred wholly in the valence band edge. Investigations on electron and hole confinement by People *et al.* [2.6] also indicated $\Delta E_v \gg \Delta E_c$ and that the band alignment was type I in nature (see Fig 2.4a) ie. the narrower band-gap $\text{Si}_{1-x}\text{Ge}_x$ falls within the wider band-gap Si. More recently, People *et al.* [2.7] predicted band alignments for strained Si/Si_{1-x}Ge_x layers lattice matched to $\langle 001 \rangle$ Si_{1-y}Ge_y buffer layers. They obtained valence band offsets from the work of Van de Walle *et al.* [2.8] who investigated band discontinuities at

Fig 2.2

A schematic of a coherent interface for lattice-matched layers. The in-plane lattice constant of the $\text{Si}_{1-x}\text{Ge}_x$ is matched to that of Si; note the extension to the lattice constant perpendicular to the interface as a consequence of lattice matching (after [2.3]).

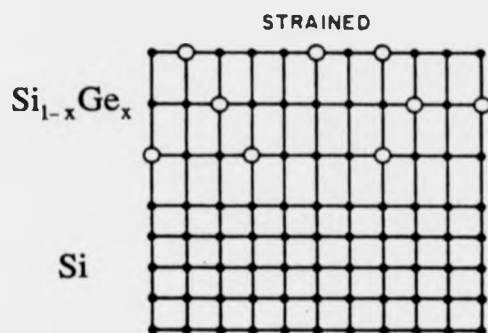
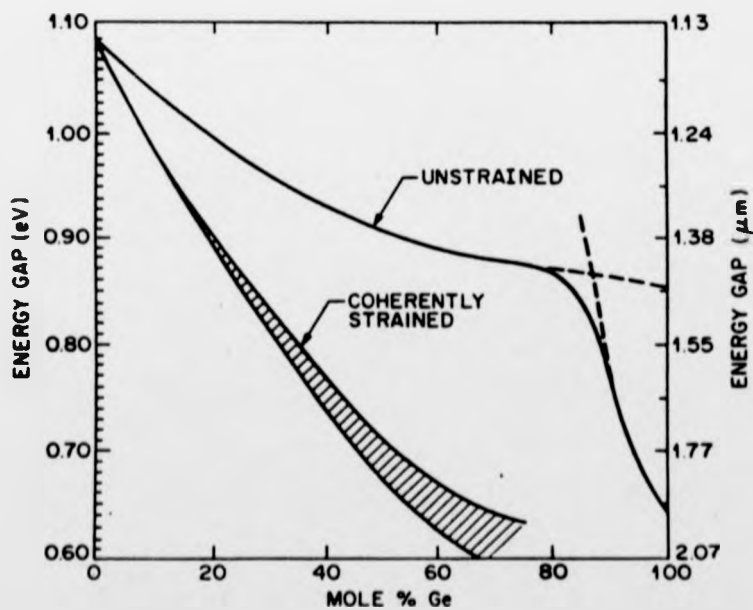


Fig 2.3

Calculated strain-induced band-gap reduction (after [2.2]).



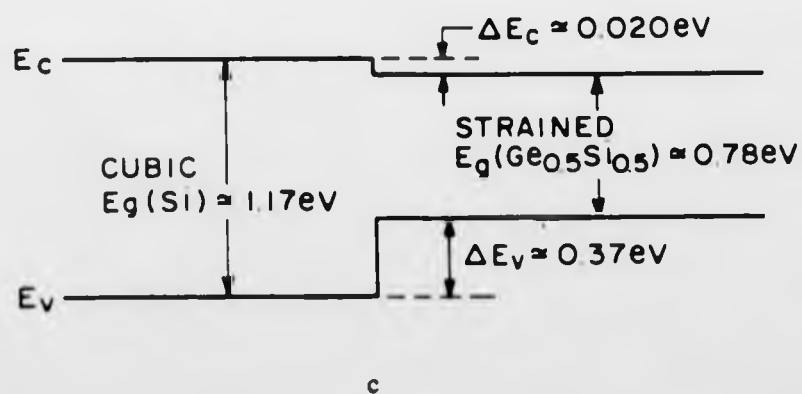
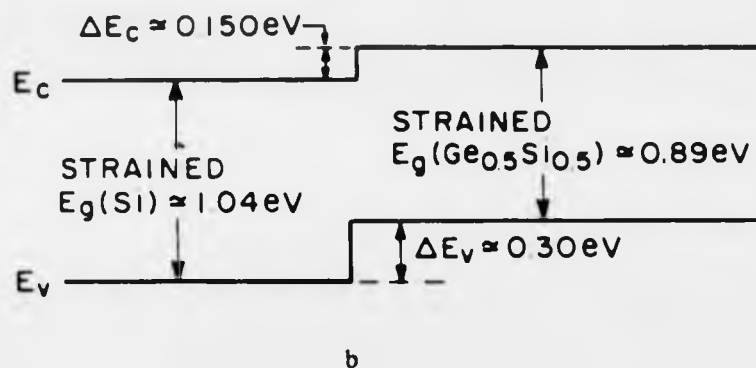
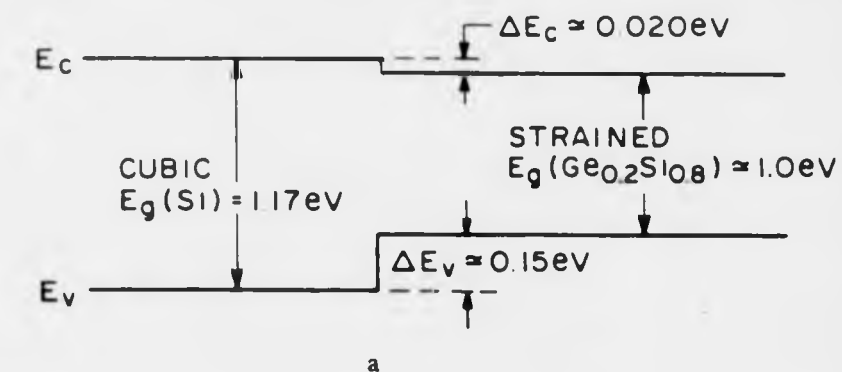
Si/Ge heterointerfaces using self-consistent calculations which allowed the electronic interfacial structure to be taken into account (thus providing a superior model as compared to previous approaches [2.9, 2.10]). Assuming a linear interpolation of the form:

$$\begin{aligned} \Delta E_v (\text{Si/Si}_{1-x}\text{Ge}_x \text{ lattice matched to } \langle 001 \rangle \text{ Si}_{1-y}\text{Ge}_y) \\ = (0.74 - 0.53y)x \end{aligned} \quad (2.1)$$

and combining this with previous work on the strained band-gap reduction allowed a variety of band alignments to be determined Fig 2.4a-c. These examples clearly illustrate the sensitivity of the band alignment to the state of the strain existing in the Si layer. In the case of lattice matched growth of $\text{Si}_{1-x}\text{Ge}_x$ on cubic $\langle 001 \rangle$ Si, the main offset occurs in the valence band Fig 2.4a. The work of Jorke *et al.* [2.11] paradoxically indicated the band alignment to be type II in nature ie. the $\text{Si}_{1-x}\text{Ge}_x$ conduction band edge lying above the Si conduction band edge; this reflected the strain existing in the Si layer and type II alignment is indeed predicted in such a situation as is illustrated in Fig 2.4b. Since the early work by People *et al.* and Van de Walle *et al.*, theoretical predictions of band discontinuities and band structure for a variety of strain situations and crystallographic orientations have been made [2.12-15].

Experimental efforts to determine band alignments have primarily involved the X-ray photoelectron spectroscopy technique [2.16-18]. Whilst the work provides good agreement with the theoretical work of People *et al.* and Van de Walle *et al.*, the margins of experimental error are large and can only provide an approximate assessment of the band offsets. Denhoff *et al.* [2.19] employed electrochemical C-V profiling to provide apparent free carrier distributions from which conduction band offsets could be extracted (see section 3.2.3.4); however, only approximate agreement was obtained due to poorly defined uniform carrier concentrations either side of the heterojunction. Khorram *et al.* [2.20] exploited the fact that emission of carriers over a barrier was a thermally activated process to determine valence band offsets for $\text{Si}_{1-x}\text{Ge}_x$ lattice matched to cubic Si; good agreement was found with theoretical predictions. Note it was assumed that the barrier to carrier movement was defined by the valence band

Fig 2.4 Band line-ups produced by a variety of strained Si/Si_{1-x}Ge_x couples (after [2.7]).



offset alone for all temperatures ie. negligible band bending occurs in the vicinity of the heterojunction.

2.3 RELAXATION MECHANISMS

The previous section indicated the effects of strain on the band-gap as a function of the Ge content of the alloy. This involved lattice-matched strained layer growth to produce a coherent interface Fig 2.2. If a critical thickness, h_c is exceeded, this built-in strain is partially or wholly relieved by the formation of misfit dislocations Fig 2.5 and the interface is seen to lose its coherency.

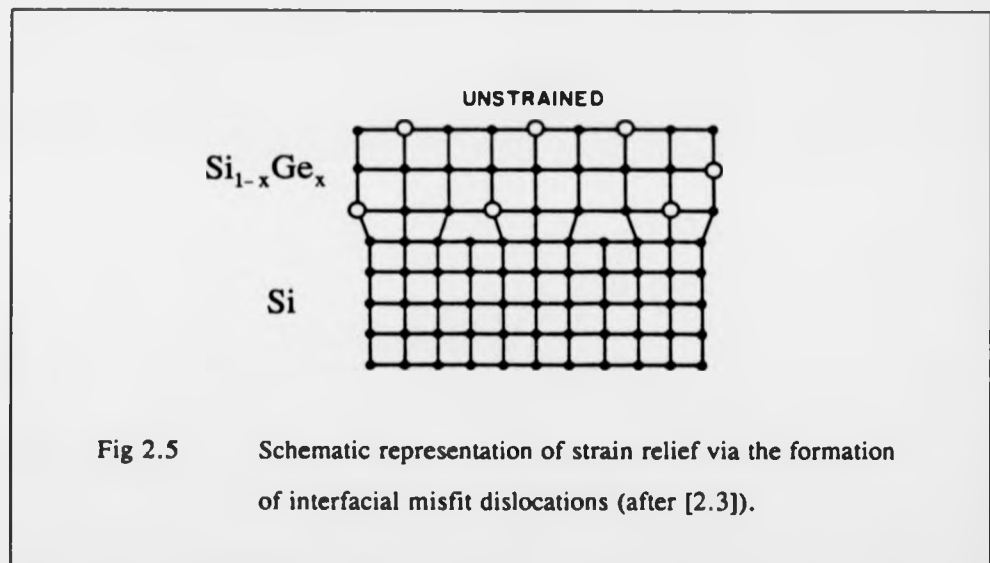


Fig 2.5 Schematic representation of strain relief via the formation of interfacial misfit dislocations (after [2.3]).

Equilibrium theories as proposed by Matthews *et al.* [2.21] and Van der Merwe [2.22] predicted lattice-matched growth of dissimilar crystals provided the lattice mismatch was small and the critical thickness was not exceeded.

Van der Merwe considered the energy associated with the superimposed homogeneous strain and misfit dislocations to be additive; under the condition of equilibrium, h_c was calculated by minimising the total energy of the system.

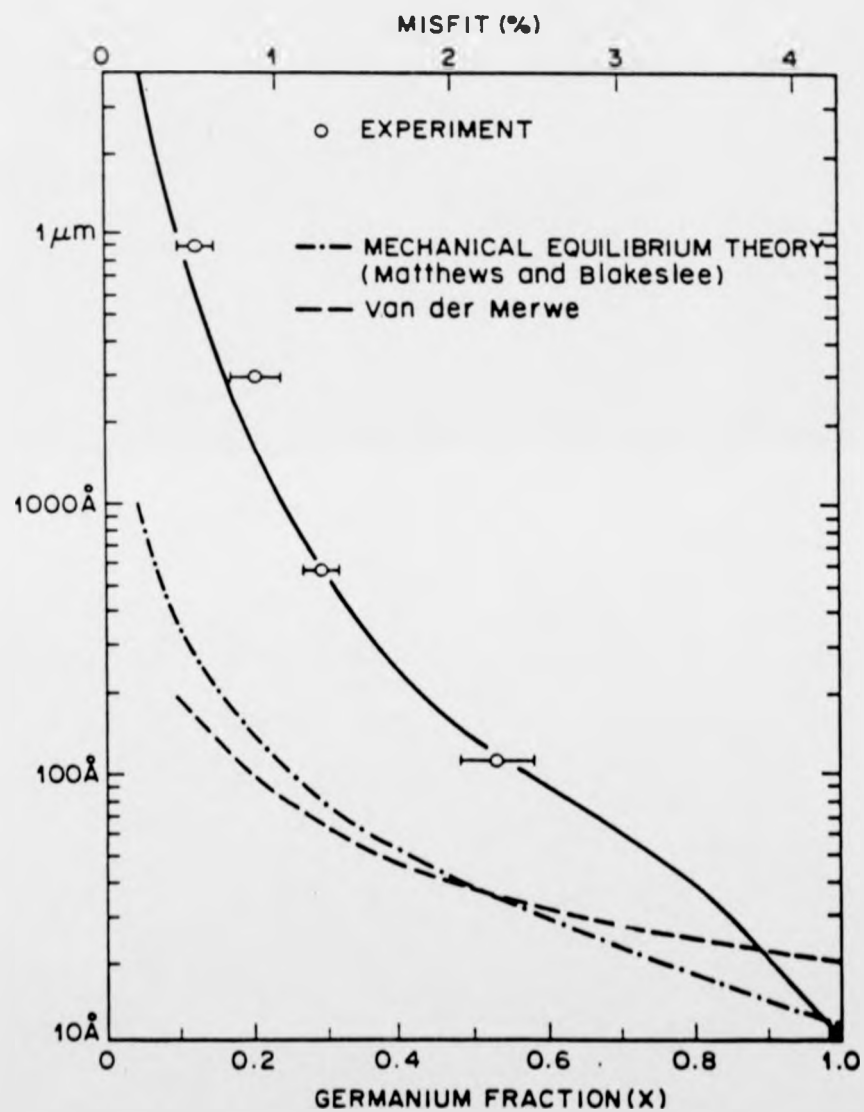
Matthews *et al.* investigated the mechanisms and types of dislocation found for relaxation of lattice coherency in GaAs and GaAs_{0.5}P_{0.5} multilayer thin films. The creation of dislocation arrays to accommodate misfit between layers was considered to be principally the result of glide of threading dislocations: a substrate dislocation could be replicated in the growing epilayer, gliding back and forth under the influence of coherency strain so generating interfacial misfit dislocations. Although this mechanism predicts the geometry of the arrays observed, it could not explain the density of such arrays in the epilayer. It was proposed that pairs of threading dislocations converted into dislocation arrays as a result of the nucleation of dislocation half-loops; nucleation of dislocation half-loops was expected for suitably large growth temperature and misfit strain, the latter being influenced by defect density causing the localised high stresses necessary for dislocation nucleation. The balance between the force exerted by the misfit strain and the force exerted by the dislocation line tension allowed a value for h_c to be determined.

The theoretical values of h_c for lattice matched Si_{1-x}Ge_x on cubic Si, according to the equilibrium theories, are shown in Fig 2.6 and are compared to the experimental work of People *et al.* [2.23]; the discrepancies may be considered in terms of [2.24]:

- (i) Insufficient resolution of the measurement technique to detect small degrees of relaxation;
- (ii) Equilibrium not being achieved such that the layers are considered to be in a metastable state.

Even if equilibrium is achieved for $h=h_c$, complete relaxation of strain will not occur at this particular thickness. The criterion that total energy be minimised suggests that relaxation will occur continuously and is only complete for $h \rightarrow \infty$. Thus the resolution limit of the measuring technique will ultimately determine the experimental values for h_c since the detected dislocation density may correspond to layer thicknesses $h \gg h_c$. Photoluminescence and the Hall effect provided a much greater sensitivity to the onset of relaxation [2.25] and revealed initial dislocation nucleation at thicknesses consistent with the predictions of the equilibrium theories.

Fig 2.6 Comparison between theoretical and experimental strained layer critical thickness versus Ge composition (after [2.3]).



The previous equilibrium theories do not take into account the existence of a barrier impeding the relaxation process; this was incorporated into non-equilibrium models describing the metastable nature of the layers. The insufficient density of threading dislocations required to source the large number of interfacial misfit dislocations needed for strain relaxation means layers will remain almost completely coherent for thicknesses $\gg h_c$ until a higher critical thickness, h_e is reached, at which significant relaxation will occur. People *et al.* [2.23] derived an expression for h_e , taking into account the extra strain energy required to overcome the barrier to initiate misfit generation. This provided a good match to the experimental data shown in Fig 2.6. Dodson *et al.* [2.26] considered the rate of relaxation to depend upon the dislocation mobility, density and growth and cooling times in which relaxation occurs. This model has been quite successful in accounting for experimental critical layer thicknesses. An alternative model was proposed by Maree *et al.* [2.27], based on similar considerations made by Matthews *et al.* concerning the nucleation of dislocation loops at the growing surface.

The overall picture is contradictory, with evidence of layers existing in a metastable state yet dislocations nucleating at equilibrium critical layer thicknesses. The key to understanding this may be in the non-uniform strain relaxation as observed by Tuppen *et al.* [2.28]. Using a standard defect reveal etch, the onset of relaxation was observed to occur in patches, at a point just above h_c ; these patches enlarged with increasing layer thickness until the entire surface was covered. The thickness of other regions of the sample where the patches were not observed was found to be much greater than h_c , indicating the strained integrity of the layers had been maintained there. These results suggested that if no barrier existed to the nucleation of dislocations, relaxation would occur for thicknesses consistent with that predicted by equilibrium theories. Indeed, the occurrence of the patches was directly related to the defect density in the epitaxial Si underlying the $\text{Si}_{1-x}\text{Ge}_x$ layer and was attributed to the ineffective oxide removal from the substrate surface before growth. The large areas free of misfit lines also indicated spontaneous nucleation of a dislocation loop at the free surface was

not energetically favourable. The orientations of the dislocations were such that for growth in the $\langle 001 \rangle$ direction, interfacial misfit dislocations lay along the $\langle 110 \rangle$ direction with threading components in $\langle 011 \rangle$ and $\langle 101 \rangle$ directions.

Houghton *et al.* [2.29] investigated the relaxation of single and multilayer $\text{Si}/\text{Si}_{1-x}\text{Ge}_x$ structures grown on $\langle 100 \rangle$ Si substrates subjected to post-growth anneals. Whilst most layers relaxed by 60° $\langle 011 \rangle$ misfit components at the first strained layer/buffer interface, superlattice structures with strained layers exceeding their individual critical thickness exhibited misfit dislocations at several interfaces in the structure. TEM revealed heterogeneous nucleation sites at the substrate/buffer interface in the form of carbon (C) and oxygen (O) precipitates and these were considered responsible for the generation of interfacial misfit segments; experimentally determined critical thicknesses were close to those predicted by Matthews *et al.*

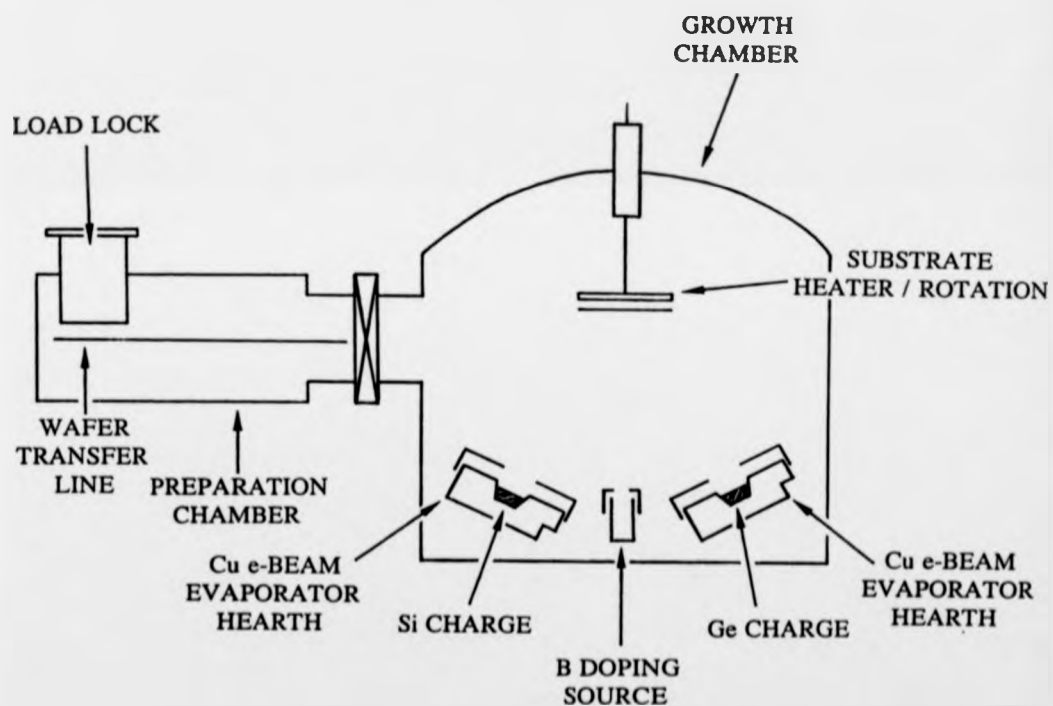
2.4 GROWTH CONSIDERATIONS

It is now appropriate to discuss the growth of such strained layers with a necessary bias towards the MBE technique by which the samples used in this study were grown.

Sample structures were grown lattice matched to cubic $\langle 100 \rangle$ Si; for the $\text{Si}_{1-x}\text{Ge}_x$ alloy layers, the major offset is expected in the valence band edge with a type I alignment. The use of uniform p-type Boron (B) doping for both Si and $\text{Si}/\text{Si}_{1-x}\text{Ge}_x/\text{Si}$ epilayers allows various characterisation techniques to be applied (see Chapter 3), providing information on both the heterointerfacial and bulk regions.

A schematic of the UHV MBE growth system is shown in Fig 2.7; only a brief description of the design and operation will be given - further details can be found in the work of Kubiak *et al.* [2.30]. Si and Ge fluxes are established using electron beam evaporation from elemental sources seated in water-cooled copper hearths; the B-doping flux is coevaporated from a B-loaded graphite crucible which is resistively heated; shutters provide instantaneous exposure or cut-off of these fluxes, thus providing careful control over abrupt atomic and dopant profiles. The UHV system reduces unwanted

Fig 2.7 Schematic of the V90S UHV MBE system used in this study.



impurity adsorption from residual gases, allowing low growth temperatures to be employed; this minimises the effects of dopant and atomic species diffusion and is particularly important in maintaining the strained integrity of $\text{Si}_{1-x}\text{Ge}_x$ epilayers during growth. The substrate holder is heated to achieve the desired 2D layer-by-layer growth and substrate rotation at approximately 60rpm provides the required uniformity over the wafer area.

Whilst the MBE growth technique can thus provide the necessarily atomically abrupt and well defined $\text{Si}/\text{Si}_{1-x}\text{Ge}_x$ heterointerfaces, the exact incorporation of the B and Ge species in the vicinity of the heterojunction and the degree of impurity contamination are unknown. These and other influencing factors will now be considered.

2.4.1 GROWTH MODE

Growth temperature greatly influences the mechanisms by which growth and subsequent unintentional impurity incorporation occurs and is crucial to understanding the electrical activity of the epitaxial layers. Epilayer growth is achieved by lateral motion of surface steps representing the dynamic movement of the surface impinging matrix or impurity species. As growth temperature is raised, the dominant growth mode in Si MBE changes from 3D to layer by layer (2D nucleation and growth) to step flow. The demarcation temperatures are ill-defined for these different growth modes and both experimental and theoretical results are conflicting, a result of the different starting conditions and parameters on which they depend; an extensive review has been provided by Sidebotham [2.31].

In contrast, higher growth temperature and/or larger Ge percentages were found to promote rough 3D growth in SiGe MBE [2.32, 2.33]. These results are summarised in Fig 2.8; for low T_s , the crystallinity of the layers is degraded as for MBE Si growth whereas it is considered to be energetically favourable to form clusters of the alloy at high T_s . The optimum conditions for good morphology and crystal quality would appear to be satisfied for $T_s \approx 550^\circ\text{C}$. Conflicting results were observed by Sakamoto

et al. [2.34] who reported similar 3D growth but at $T_s=450^\circ\text{C}$. Despite this, T_s can be found for which good quality heterostructures may be grown experimentally [2.32] - a fact which seems to be missing from the work of Venkatasubramanian *et al.* [2.35] who conclude that conventional MBE growth techniques are incompatible with the growth of good quality heterostructures. 3D growth may also affect the critical thickness previously considered; growth should be carried out not only in the pseudomorphic form

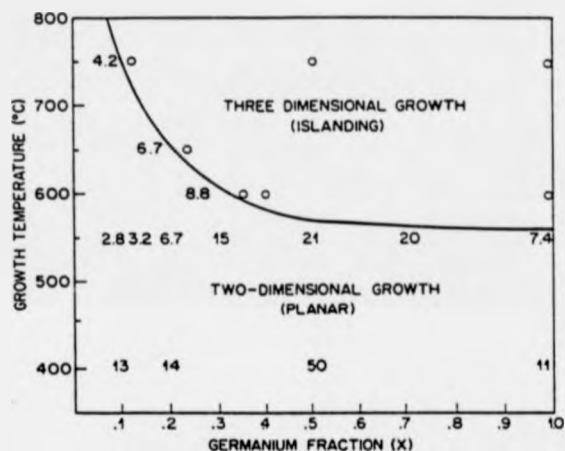


Fig 2.8 Ideal growth conditions for $\text{Si}_{1-x}\text{Ge}_x$ on Si (after [2.32]). Numerical values indicate degree of crystallinity as determined by RBS: 0 (high), 100 (low).

but also layer-by-layer deposition in order to achieve flat and abrupt interfaces, free of misfit dislocations. The transition layer thickness from 2D to 3D growth was found to be a function of Ge content and growth temperature [2.36] and in all cases was smaller than the critical thickness of People *et al.* [2.23] Fig 2.6.

2.4.2 DEFECTS IN Si AND SiGe MBE LAYERS

The type and density of defects in MBE Si are expected to be different to those grown by conventional techniques, a result of the non-equilibrium conditions present during growth; changes in the growth conditions, substrate cleans and substrate crystalline quality can all further affect the epitaxially grown layer.

All atoms in a perfect lattice are at specific atomic sites; however, point defects can occur, causing departures from this ideal situation. Intrinsic point defects describe vacant atomic sites or vacancies and associated interstitial atoms, resulting from the removal of an atom from an atomic site and its introduction into a non-lattice site. They may be introduced into a crystalline structure simply by virtue of temperature with the interstitial defect remaining mobile down to very low temperatures. Extrinsic point defects describe the incorporation of impurity atoms into the crystalline host structure and may exist in a substitutional form, replacing an atom from the host structure or an interstitial form, where the impurity atom is at a non-lattice site. Extended defects describe defects with dimensions greater than zero and encompass dislocations, particulates, precipitates and dislocation-related inhomogeneities such as stacking faults. Since the MBE grown layers primarily exhibit threading and misfit dislocation defects, other extended defects will not be considered in detail.

Such defects are of importance since they can introduce levels into the band-gap which can either modify the free carrier distribution if they act as shallow dopants or form recombination-generation centres if sited close to mid-gap; both can significantly degrade the electrical quality of the material if the impurities are unintentionally introduced.

2.4.2.1 IMPURITY INCORPORATION

Phenomenologically based formulations have been used to describe dopant behaviour in Si, balancing the competing processes of arrival, desorption, incorporation and surface accumulation of dopant atoms. Work by Pindoria *et al.* [2.37] indicated most shallow dopant species would surface accumulate if the solid solubility was

exceeded. Kubiak *et al.* [2.38] found that surface accumulation would increase with increasing growth temperature, reaching a critical temperature, T_c which marked the transition between kinetically limited incorporation and equilibrium limited incorporation (since for $T > T_c$ dopants will desorb). Attempts to increase the surface coverage resulted in inclusion of precipitates in the growing epilayer.

It was proposed [2.37] that surface accumulation would be reduced in SiGe alloys since the larger Ge atom should increase the size threshold at which accumulation occurred; this was verified by Parry *et al.* [2.39].

Such work can provide clues as to the way unintentional impurities may be incorporated into the epitaxial layers. If surface segregation is low at the growth temperature, incorporation of the impurity in the epilayer is readily achieved as an isolated point defect. However, if the surface segregation is large, the impurity will be incorporated in a different manner and is more likely to form a precipitate. Such highly mobile impurities may also be gettered onto dislocations at the growth temperature. Robbins *et al.* [2.40] noted a temperature dependent interaction between residual surface contamination and initially deposited Si adatoms. They suggested fast adatom diffusion at high temperatures led to long range step growth and this motion concentrated mobile contamination by segregation at the leading edge, so producing large precipitates. At lower growth temperatures, diffusion and step flow occurred over shorter distances, so producing individual impurity incorporation as point defects or only small precipitates.

C and O have been observed in bulk Si MBE grown layers at concentrations similar to those found in Czochralski material [2.41]. Higher concentrations have been observed at epilayer/substrate interfaces and whilst C is considered electrically inactive, occupying a substitutional site, O can form precipitates at which dislocations have been observed to nucleate and has also exhibited donor-like behaviour [2.42]. Both contaminants can be reduced by appropriate pre-growth substrate cleans [2.43].

Unintentional doping in Si MBE systems is usually n-type and attributed to Phosphorous (P), thought to originate from the stainless steel used in construction of the

UHV MBE system [2.31, 2.41]. This is observed to decrease in mature MBE systems where doping levels $< 10^{14} \text{ cm}^{-3}$ have been found.

Transition metal contamination can be a considerable problem, being extremely detrimental to Si MBE layers. The growth occurs in an environment surrounded by metallic components, some of which undergo radiant heating, and it becomes unavoidable to eliminate all metallics during growth. Pindoria [2.44] reports contamination from Tantalum (Ta), Copper (Cu), Chromium (Cr), Iron (Fe) and Manganese (Mn) in Si MBE layers ranging between mid- 10^{14} - mid- 10^{15} cm^{-3} as determined by NAA and SIMS. Corresponding deep level concentrations, as determined via DLTS, were several orders of magnitude lower which suggested the bulk of the metallic contamination to be in an electrically inactive form. At the elevated temperatures of growth, surface and grown-in metallic contamination have the ability to diffuse, so producing volume contamination. During the cooling process, transition metals may remain dissolved or precipitate out; both situations may be detrimental to the electrical quality of the material [2.45]. The determining factors are the solubilities (S) and diffusivities (D) of the transition metals in Si, which are seen to increase exponentially with temperature [2.46]. Extrapolated solubilities at 300K are low in contrast to the dramatic increase in solubility at elevated temperatures, whereas diffusivity does not disappear at 300K. As a consequence, transition metals may remain in solution, form complexes or precipitate depending upon the diffusivity of the metal, whether the solubility limit has been exceeded and the cooling rate employed. The diffusivities of heavy transition metals Cu, Nickel (Ni) and Cobalt (Co) are sufficiently high to enable both out-diffusion of the metal and precipitation by homogeneous nucleation. These metals cannot easily be quenched in to form electrically active defects and so generally remain undetected via such techniques as DLTS. Note that work by Broniatowski *et al.* [2.47] suggested that metal precipitates could act as multicarrier traps as a result of band bending within the bulk Si, analogous to rectifying contacts. The diffusivities of lighter transition metals Scandium (Sc), Fe etc. are too small to permit out diffusion and homogeneous precipitation; as the diffusion of these

elements proceeds via an interstitialcy mechanism, such elements are more likely to be quenched in on interstitial sites, forming electrically active point defects which may be detected. Calculations for the band-gap positions of transition metal point defect levels have yielded good agreement for some interstitial and substitutional sites as compared to experimentally observed transitions, although experimental data, particularly for substitutional point defects, is not available [2.48].

2.4.2.2 STRUCTURAL DEFECTS

Dislocation densities are typically found in the range 10^2 - 10^4 cm^{-2} in Si MBE layers [2.49, 2.50]; consideration of structures incorporating metastable SiGe layers will be subject to the degree and mechanisms by which the strained layers relax and was discussed in the previous section. Such defects can originate from both the epitaxial process as well as from the substrate; Si epilayers grown on $\langle 100 \rangle$ substrates are found to have lower defect densities compared to those grown on $\langle 111 \rangle$ substrates [2.50] whilst the threading dislocation density in Si/SiGe epilayers of 10^4 cm^{-2} was attributed to nucleation sites associated with Si inclusions assumed to originate from the chamber walls during growth [2.51]. Dislocations intrinsic to the substrate can extend into the growing epilayer and may be minimised by the use of dislocation free substrates or reducing the thermal stresses to which the substrate is subjected during growth [2.52]. Dislocations may also nucleate at the epilayer/substrate interface as a result of C/O contamination and may be reduced by appropriate pre-growth substrate cleans as detailed previously.

2.5 ELECTRONIC PROPERTIES OF IMPURITIES AND DEFECTS

The preceding sections have considered the origins of impurities and defects in MBE Si. Their influence on the electrical quality of the epilayers will now be considered.

For p-type material, interest lies with the equilibrium occupation of impurity and defect-induced band-gap states since it is the occupancy of such states which are

observed via the DLTS technique (see Chapter 3). Furthermore, assuming the simplest case of states being monovalent ie. occupied by a single hole, only donor-like states will be in an ionised form when considering the equilibrium occupancy.

Point defects incorporated into the crystalline lattice may be considered to introduce discrete energy localised states within the band-gap. For a donor-like state in an ionised form ie. occupied by a hole, negligible band-bending is expected, except for high concentration, localised defects.

In contrast, line defects, such as dislocations, may be considered to produce a much more pronounced band bending for relatively low band-gap state concentrations due to the highly localised, interacting charge states. Consider the case shown in Fig 2.9 for a dislocation introducing donor-like states into the band-gap in p-type material with a shallow doping concentration, N_A . If the states lie above the Fermi level, they may be considered as occupied by holes, and consequently in an ionised form whereas if they lie below the Fermi level, the states are unoccupied and are considered neutral. Assuming a small spatial separation between the occupied states, the dislocation-related states may be viewed as a uniform line charge of charge Q per unit length. The positively charged line repels conduction holes and a cylindrical space-charge region forms around the line charge; the average (negative) space-charge per unit volume in the cylinder is given by $q(N_A - N_D)$, where q is the electronic charge and N_D is the donor concentration. From the condition of neutrality, the space-charge cylinder radius, R may be defined as [2.53]:

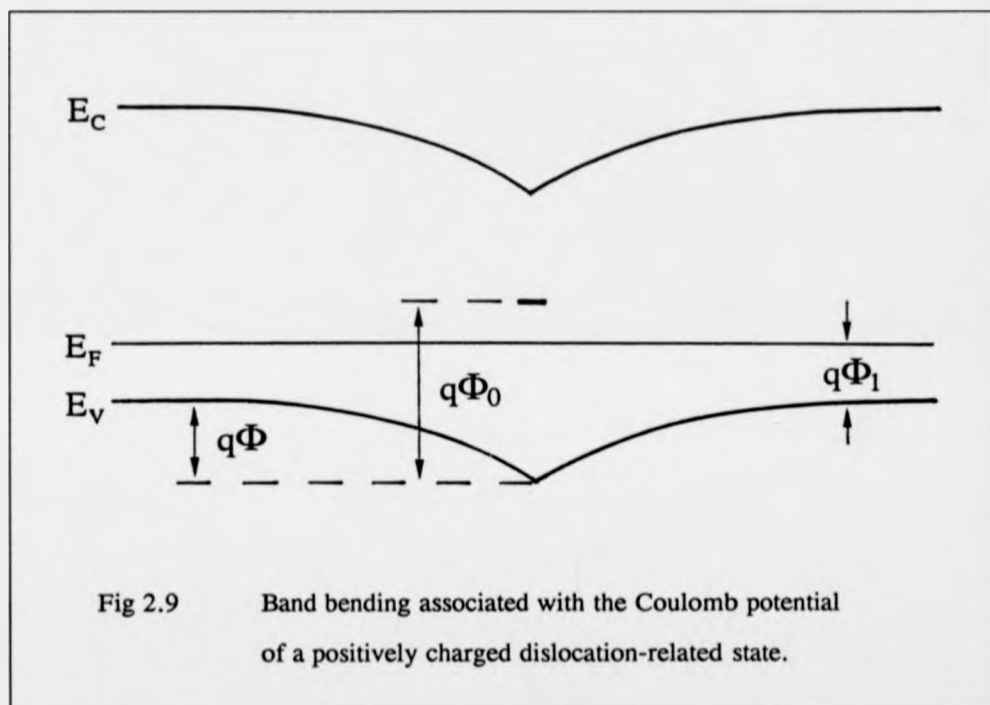
$$\pi R^2 (N_A - N_D) = \frac{1}{a} \quad (2.2)$$

where a is the spacing between occupied sites. Note that the boundary of the space-charge cylinder is not clearly defined for finite temperatures, since free hole carriers spill into the space-charge region. The build-up of the line charge shifts the energy of the trapped holes in the vicinity of the dislocation and is represented by the bending of the conduction and valence bands downwards; the defect level may be considered to be

shifted in energy by an amount $q\Phi$ where [2.54]:

$$q\Phi = \frac{qQ}{2\pi\epsilon_0\epsilon_r} \left(\ln \left[\frac{L_D Q}{q} \right] - 0.5 \right) \quad (2.3)$$

where L_D is the local Debye length in the vicinity of the defect. Significant band bending will occur for only small fractions of the dislocation-related network being occupied by holes and becoming charged.



Consider three simple cases of dislocation occupation:

- (i) $q\Phi_0 < q\Phi_1$ the dislocation state is below the Fermi level and the dislocation is uncharged; in this situation little electrical activity would be observed.
- (ii) $q\Phi_0 > q\Phi_1$ and N_A is such that the band bending caused by the filled states is sufficient to make the states intersect with the Fermi level, resulting in partial occupation of the dislocation states. This occupation will vary with temperature as the position of the Fermi level changes; such a state could be detected by DLTS but active state concentrations would be in error as only occupied centres would be detected by

such techniques. Since DLTS measurements involve scanning temperature, dislocation features would undergo distortion due to the changing state occupancy.

(iii) $q\Phi_0 > q\Phi_1$ and N_A is such that all the dislocation states are full and the band bending is insufficient to make the centres intersect with the Fermi level. In this situation, the dislocation charge is independent of temperature and DLTS measurements will accurately measure active state concentrations, since all the states will fill during the filling pulse.

The increased complexity of dislocation-related states, as compared to isolated point defects, is clear since the equilibrium occupancy of such states are controlled by the coulomb potential (see section 3.2.4.5) and it is possible that a dislocation may exhibit all three regimes of behaviour defined in (i), (ii) and (iii), depending upon the temperature, local doping level and line concentration of defect states.

This simple model of interacting dislocation-related states was considered by Figielski [2.55] to form a band of energy levels, as opposed to discrete energy levels, as a result of the overlapping wave function for such closely spaced states. However, such states are not now considered intrinsic to the dislocation core ie. each active state being related to the individual dangling bonds as proposed by Read [2.53]. Work by Jaros *et al.* [2.56] showed that such energy bands associated with dangling bonds were $\approx 0.5\text{eV}$ in width and, hence, it was inconceivable that well resolved peaks could be observed via spectroscopic studies such as DLTS. It is now generally accepted that the interaction between dislocations and point defects is the significant factor in determining the electrical activity of dislocations. This becomes a complex regime and will depend upon dislocation density and the type of impurities present, as will be considered in Chapter 5.

The ability of extended defects and, in particular, dislocations in both Si and SiGe to act as sinks for metal impurities is well documented [2.57, 2.58]. The various interaction mechanisms between point defects and dislocations was discussed by Bullough *et al.* [2.59] who proposed the elastic interaction arising from the difference in size between solute and solvent atoms to be the dominant gettering mechanism. Thus,

impurities can be drawn into the strain field associated with the dislocation core and create what is known as a Cottrell atmosphere [2.60].

One final comment regarding the band of energies associated with dislocation-related states is that the band-bending produced by the charging of each state will be experienced by all the others on the defect, with the result that the occupation of deeper levels could produce band-bending sufficient to lower shallow states below the Fermi level. Thus, such shallow states which, ordinarily, are charged, would be rendered electrically neutral, in a similar way to compensation effects which can occur in the semiconductor bulk.

CONCLUSION

The band offset is a bulk property and depends upon the macroscopic strain present in the two materials far from the heterointerface. Our knowledge of such alignments combined with the predicted strain-induced band edge splitting allows a considerable degree of confidence in predicting the band structure for arbitrary heterostructures. This flexibility in design is dependent upon lattice matched strained layer growth; the ability to grow such layers beyond the equilibrium critical thickness, h_c with minimal misfit dislocation generation is dependent upon the density and distribution of heterogeneous nucleation sites, which can exist both at the substrate/epilayer interface and the free growing surface. The use of the UHV MBE growth technique with appropriate substrate preparation and careful choice of growth temperature should minimise both dislocation nucleation sites and unintentional impurity incorporation into the growing layers; one should, however, remain aware of the possible departures from the ideal defect/impurity-free single crystal growth. A tendency for strain relief to occur at the lowest heterointerface between cubic Si and strained $\text{Si}_{1-x}\text{Ge}_x$ is observed experimentally, such that the in-plane lattice constant is enlarged at subsequent upper heterointerfaces, where minimal misfit dislocation nucleation is observed. Such changes in lattice parameter and hence strain, through the formation of misfit dislocations, is likely to have a significant effect on band offsets.

REFERENCES

- 2.1 J. S. Blakemore "Solid State Physics" 2nd Ed. (CUP, Cambridge 1985) 366
- 2.2 R. People Phys. Rev. B 32 (1985) 1405
- 2.3 J. C. Bean in "Silicon Molecular Beam Epitaxy" Vol II
Ed. E. Kasper and J. C. Bean (CRC press, Florida 1988) Chapter 11
- 2.4 R. Braunstein, A. R. Moore and F. Herman Phys. Rev. 102 (1958) 695
- 2.5 D. V. Lang, R. People, J. C. Bean and A. M. Sergent
Appl. Phys. Lett. 47 (1985) 1333
- 2.6 R. People, J. C. Bean and D. V. Lang
Proc. 1st Int. Symp. on Si MBE (Electrochem. Soc., New Jersey 1985) 364
- 2.7 R. People and J. C. Bean Appl. Phys. Lett. 48 (1986) 538
- 2.8 C. G. Van de Walle and R. M. Martin
J. Vac. Sci. Technol. B3 (1985) 1256
- 2.9 W. R. Frensley and H. Kroemer J. Vac. Sci Technol. 13 (1976) 810
- 2.10 W. A. Harrison and J. Tersoff J. Vac. Sci Technol. B4 (1986) 1068
- 2.11 H. Jorke and H. J. Herzog
Proc. 1st Int. Symp. on Si MBE (Electrochem. Soc., New Jersey 1985) 352
- 2.12 C. G. Van de Walle and R. M. Martin Phys. Rev. B 34 (1986) 5621
- 2.13 R. J. Turton, M. Jaros and I. Morrison Phys. Rev. B 38 (1988) 8397
- 2.14 J. M. Hinckley and J. Singh Phys. Rev. B 42 (1990) 3456
- 2.15 L. Colombo, R. Resta and S. Baroni Phys. Rev. B 44 (1991) 5572
- 2.16 W. -X. Ni, J. Knall and G. V. Hansson Surf. Sci. 189/190 (1987) 379
- 2.17 W. -X. Ni and G. V. Hansson Phys. Rev. B 42 (1990) 3030
- 2.18 E. T. Yu, E. T. Croce, D. H. Chow, D. A. Collins, M. C. Phillips,
T. C. McGill and J. O. McCaldin J. Vac. Sci. Technol. B8 (1990) 908
- 2.19 M. W. Denhoff, J. -M. Baribeau, D. C. Houghton and K. Rajan
J. Cryst. Growth 81 (1987) 445
- 2.20 S. Khorram, C. H. Chern and K. L. Wang
Proc. Mat. Res. Soc. Symp. 220 (1991) 181

- 2.21 J. W. Matthews and A. E. Blakeslee J. Cryst. Growth 27 (1974) 118
- 2.22 J. H. Van de Merwe J. Appl. Phys. 34 (1963) 117
- 2.23 R. People and J. C. Bean Appl. Phys. Lett. 47 (1985) 322
- 2.24 S. C. Jain, J. R. Willis and R. Bullough Advances in Physics 39 (1990) 127
- 2.25 I. J. Fritz Appl. Phys. Lett. 51 (1987) 1080
- 2.26 B. W. Dodson and J. Y. Tsao
Proc. 2nd Int. Symp. on Si MBE (Electrochem. Soc., New Jersey 1988) 105
- 2.27 P. M. J. Marée, J. C. Barbour, J. F. Van der Veen, K. L. Kavanagh,
C. W. T. Bulle-Lieuwma and M. P. A. Vieggers
J. Appl. Phys. 62 (1987) 4413
- 2.28 C. G. Tuppen, C. J. Gibbings and M. Hockly
J. Cryst. Growth 94 (1989) 392
- 2.29 D. C. Houghton, D. D. Perovic, J. -M. Baribeau and G. C. Weatherly
J. Appl. Phys. 67 (1990) 1850
- 2.30 R. A. A. Kubiak, E. H. C. Parker and S. S. Iyer in
"Silicon Molecular Beam Epitaxy" Vol I Ed. E. Kasper and J. C. Bean
(CRC press, Florida 1988) Chapter 2
- 2.31 E. C. Sidebotham PhD Thesis UMIST (1990)
- 2.32 J. C. Bean, L. C. Feldman, A. T. Fiory, S. Nakahara and I. K. Robinson
J. Vac. Sci. Technol. A2 (1984) 436
- 2.33 Y. Fukuda and Y. Kohama Jap. J. Appl. Phys. 26 (1987) L597
- 2.34 K. Sakamoto, T. Sakamoto, S. Nagao, G. Hashiguchi,
K. Kuniyoshi and Y. Bando Jap. J. Appl. Phys. 26 (1987) 666
- 2.35 R. Venkatasubramanian and R. Khoie
Proc. Mat. Res. Soc. Symp. 220 (1991) 129
- 2.36 X. Wang, G. L. Zhou, T. C. Zhou, C. Sheng and M. R. Yu
Proc. Mat. Res. Soc. Symp. 220 (1991) 241
- 2.37 G. Pindoria, R. A. A. Kubiak, S. M. Newstead and D. P. Woodruff
Surf Sci. 234 (1990) 17

- 2.38 R. A. A. Kubiak and C. P. Parry Proc. Mat. Res. Soc. Symp. 220 (1991) 63
- 2.39 C. P. Parry, R. A. A. Kubiak, S. M. Newstead,
E. H. C. Parker and T. E. Whall Proc. Mat. Res. Soc. Symp. 220 (1991) 79
- 2.40 D. J. Robbins, A. J. Pidduck, A. G. Cullis, N. G. Chew, R. W. Hardeman,
D. B. Gasoon, C. Pickering, A. C. Daw, M. Johnson and R. Jones
J. Cryst. Growth 81 (1987) 421
- 2.41 S. L. Delage, S. S. Iyer and G. J. Scilla
Proc. 2nd Int. Symp. on Si MBE 88 (1988) 459
- 2.42 K. V. Ravi EMIS Datareview RN=15730 (1987) 252
- 2.43 Y. H. Xie, Y. Y. Wu and K. L. Wang Appl. Phys. Lett. 48 (1986) 287
- 2.44 G. Pindoria PhD. Thesis University of Warwick (1990)
- 2.45 K. Graff Mat. Sci. & Eng. B4 (1989) 63
- 2.46 E. R. Weber Appl. Phys. A30 (1983) 1
- 2.47 A. Broniatowski and C. Haut Phil. Mag. Lett. 62 (1990) 407
- 2.48 F. Beeler, O. K. Anderson and M. Scheffler Phys. Rev. B 41 (1990) 1603
- 2.49 J. H. McFee, R. G. Schwartz, V. D. Archer, S. N. Finegan and L. C. Feldman
J. Electrochem. Soc. 130 (1983) 214
- 2.50 T. Tatsumi, N. Aizaki and H. Tsuya Jap. J. Appl. Phys. 24 (1985) L227
- 2.51 F. M. Ross, R. Hull, D. Bahnck, J. C. Bean, L. J. Peticolas,
R. A. Hamm and H. A. Huggins J. Vac. Sci. Technol. B10 (1992) 2008
- 2.52 Y. Ota Thin Sol. Films 106 (1983) 3
- 2.53 W. T. Read Phil. Mag. 45 (1954) 775
- 2.54 P. R. Wilshaw and T. S. Fell Inst. Phys. Conf. Series 104 (from Int. Symp.
Struct. Prop. Disloc. Semicond., Oxford 1989) 85
- 2.55 T. Figielski Phys. Stat. Sol. (a) 121 (1990) 187
- 2.56 M. Jaros and M. J. Kirton Phil. Mag. 46 (1982) 85
- 2.57 J. S. Kang and D. K. Schroder J. Appl. Phys. 65 (1989) 2974
- 2.58 A. S. Salih, H. J. Kim, R. F. Davis and G. A. Rozgonyi
Appl. Phys. Lett. 46 (1985) 419

- 2.59 R. Bullough and R. C. Newman in "Progress in Semiconductors" 8
Ed. A. F. Gibson and R. E. Burgess (Wiley, New York 1964) 100
- 2.60 A. H. Cottrell "Dislocations and Plastic flow in Crystals"
(Clarendon press, Oxford 1953) 134

CHAPTER 3

THEORETICAL AND EXPERIMENTAL CONSIDERATIONS

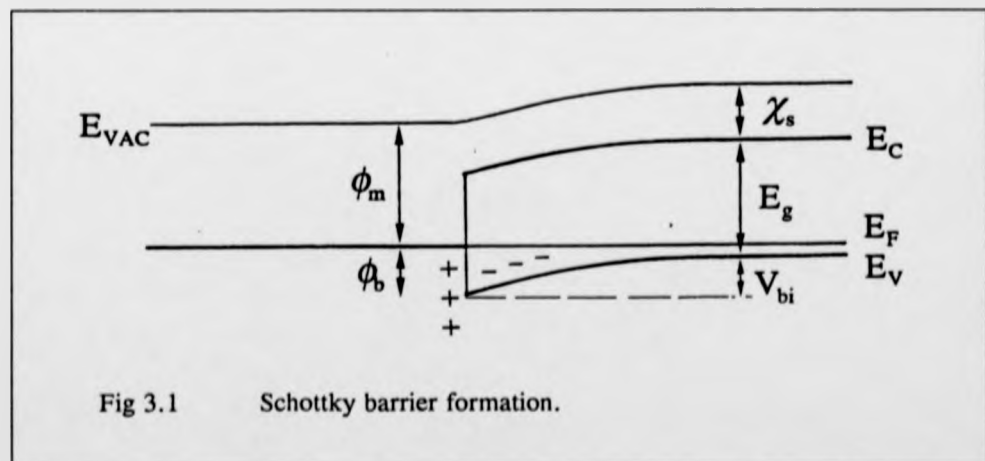
3.1 INTRODUCTION

The use of measurements of electrical capacitance for characterisation of semiconductors relies on the properties and capacitance of a depletion region associated with a reverse biased PN or Schottky diode. The work reported here is based on the formation of metal-p-type semiconductor Schottky barriers; theoretical considerations made herein are relevant to the Schottky barrier with minor adjustments necessary for the case of the PN diode.

3.2 ELECTRICAL CHARACTERISATION

3.2.1 THE SCHOTTKY BARRIER

When a metal is brought into contact with a p-type semiconductor, holes are transferred from the semiconductor into the metal such that the Fermi levels become coincident Fig 3.1. This creates a positive charge of excess holes in the metal balanced



by a negative charge of the ionised shallow acceptor dopants within the semiconductor. At the interface, the vacuum level is the same for both materials, so a step must exist between the Fermi level in the metal and the semiconductor valence band edge. This defines the barrier height to thermionic emission of holes from the metal into the semiconductor as [3.1]:

$$\phi_b = E_g + \chi_s - \phi_m \quad (3.1)$$

where E_g is the band-gap of the semiconductor, ϕ_m is the metal work function and χ_s is the electron affinity of the semiconductor. The band bending that results in the semiconductor depends upon the doping level; for zero externally applied bias, the band bending or built-in voltage, V_{bi} may be defined as:

$$V_{bi} = \phi_b - \frac{E_F - E_V}{q} \quad (3.2)$$

where E_F is the Fermi energy, E_V is the valence band edge and q is the electronic charge. In reality, it was found that the barrier height was less dependent on the metal work function than as proposed in (3.1). An explanation for this was put forward by Bardeen [3.2] who suggested the discrepancy was due to "pinning" of the barrier height by surface states such that:

$$\phi_b \approx E_g - \phi_0 \quad (3.3)$$

where ϕ_0 is defined as the neutral level of the surface states relative to the valence band edge. Indeed, the electronic band structure as depicted in Fig 3.1 represents the ideal Schottky barrier situation; on removal from the UHV MBE system, a native oxide approximately 5nm thick will form on the semiconductor surface. Whilst this interfacial oxide is thin enough to allow carrier tunneling and hence approximates to Fig 3.1, one should remain aware of the fact that interface states are likely to be a property of the oxide-semiconductor interface. The process of subsequent metal deposition can further influence the electronic band structure if the interface is non-abrupt.

Thus, it is clear that barrier heights are determined by a combination of mechanisms dependent upon the crystallographic and metallurgical properties of the interface.

3.2.2 CURRENT TRANSPORT MECHANISMS

In the Schottky diode, the current-limiting process is assumed to be the transfer of carriers over the barrier between the semiconductor and the metal. For a diode of area A , the Current-Voltage (I-V) relationship is given by [3.3]:

$$I = I_0 \exp\left(\frac{qV_A}{nkT}\right) \cdot (1 - \exp\left(-\frac{qV_A}{kT}\right)) \quad (3.4)$$

I_0 is the zero-bias saturation current given by:

$$I_0 = A^* \cdot T^2 \cdot A \exp\left(-\frac{q[\phi_b - \Delta\phi_b]}{kT}\right) \quad (3.5)$$

where V_A is the externally applied bias and A^* is the Richardson constant for thermionic emission. The quantity $\phi_b - \Delta\phi_b$ is the effective barrier height seen by holes under both forward and reverse bias; the bias dependence of the barrier height is represented by the term $\Delta\phi_b$. The parameter n defines the ideality factor of the Schottky diode and describes the deviation away from thermionic emission as the dominant current transport mechanism under forward bias. Several situations may be considered for which n may deviate from unity as a consequence of the effective barrier height being reduced, such as image force lowering and interfacial layers [3.3]. Of greater interest are the possible effects of recombination-generation centres within the layers:

Recombination-Generation effects

Using similar considerations to those developed for electron-hole transitions via deep states in PN diodes [3.4], low forward bias can reveal an additional recombination component to the measured current as:

$$I_R = I_{0R} \exp\left(\frac{qV_A}{2kT}\right) \left\{ 1 - \exp\left(-\frac{qV_A}{kT}\right) \right\} \quad (3.6)$$

where the zero bias recombination current, I_{0R} is given by:

$$I_{0R} = \frac{qn_i A W}{2\tau_n} \quad (3.7)$$

n_i being the intrinsic carrier concentration, τ_0 is the carrier lifetime and W is the depletion width. From (3.4) and (3.6) the ratio of thermionic to recombination current

components may be expressed as:

$$\frac{I}{I_R} = K \left(T^2 \tau_0 \exp \left\{ \frac{q(E_g + V_A - 2\phi_b)}{2kT} \right\} \right) \quad (3.8)$$

where K is a constant and the E_g term is introduced through its relation to the intrinsic carrier concentration. $(E_g + V_A - 2\phi_b)$ is negative for small forward biases; thus, the ratio will increase with bias and temperature and hence, recombination current components will be more important at lower bias and temperatures such that $n \rightarrow 2$.

For reverse biases, electron-hole pairs created at deep states give rise to a generation current component:

$$I_G = \frac{qn_i W A}{2\tau_0} \quad (3.9)$$

From (3.4), the reverse current should saturate at I_0 independent of reverse bias whereas I_G shows a voltage dependence through the term W which is proportional to $(V_A)^{1/2}$. From (3.4) and (3.9), the ratio of thermionic to generation current component may be expressed as:

$$\frac{I}{I_G} = K' \left(\frac{T^2 \tau_0}{V_A^{1/2}} \right) \exp \left\{ \frac{q(E_g - 2\phi_b)}{2kT} \right\} \quad (3.10)$$

where K' is a constant. Generation current components are more apparent at lower temperatures through the increase in band-gap, E_g ; thermionic current components dominate at higher temperatures.

Furthermore, assumptions made may require modification to the recombination-generation current components defined here. The deep level energy is considered coincident with the intrinsic Fermi level, and this allows definition of the carrier lifetime as [3.4]:

$$\tau_0 = 1/\sigma v_{th} N_T \quad (3.11)$$

where σ is the capture cross section assumed the same for both electrons and holes, v_{th} is the thermal velocity of the carriers and N_T is the deep level concentration. These are gross assumptions since in reality the capture cross sections for electrons and holes will

not be the same and the spatial distribution of deep levels will not necessarily be uniform.

The suitability of a diode for capacitance measurements can thus be gauged from its I-V characteristics. The series resistance of the diode can be measured from the slope of the forward bias I-V characteristic whilst the low leakage required for capacitance measurements can be determined from the reverse bias I-V characteristic. These will be considered further in the next section.

3.2.3 CAPACITANCE-VOLTAGE PROFILING

3.2.3.1 DEPLETION CAPACITANCE

The depletion of free hole carriers, leaving behind a distribution of negatively charged acceptors will result in the band bending shown in Fig 3.1. Poissons equation [3.5] relates the electric field, $E(x)$ to the space-charge density, $\rho(x)$ at position x such that:

$$\frac{dE(x)}{dx} = \frac{\rho(x)}{\epsilon_0 \epsilon_r} \quad (3.12)$$

From the definition of electrostatic potential one may determine the depletion depth, x_d associated with such band bending, which defines the transition between the depletion region and the neutral bulk of the semiconductor:

$$x_d = \left(\frac{2\epsilon_0 \epsilon_r}{qN_A} \cdot V \right)^{1/2} \quad (3.13)$$

where N_A is the acceptor dopant concentration, ϵ_0 is the absolute permittivity and ϵ_r is the dielectric constant. V is reduced for positively applied forward bias and is increased for negatively applied reverse bias; since interest lies only with the reverse bias depletion capacitance, the total potential may be defined as $V = V_A + V_{bi}$, where V_A is the applied bias and V_{bi} is the built-in potential; note V is a positive quantity.

In order to define a depletion capacitance, it is useful to consider the case of a linear dielectric where charge stored is related to the applied voltage by a constant capacitance, C_L which is voltage independent. For a depletion layer, on the other hand,

the fixed space-charge per unit area, Q shows a dependence of $V^{1/2}$ [3.6] and hence a constant capacitance cannot be defined. However, a differential capacitance may be defined at a particular reverse bias, $V_A = V_R$ such that:

$$C = A \cdot \lim_{\Delta V \rightarrow 0} \frac{\Delta Q}{\Delta V} = A \cdot \frac{dQ}{dV} \quad (3.14)$$

where A is the diode area. For a small increment dV at reverse bias V_R , the depletion width increment causes a linear increase in fixed space-charge per unit area, dQ ; this is a good approximation to the change in charge on a parallel plate capacitor of separation, x_d defined by total band bending, V . Thus, from Poissons equation:

$$V = V_R + V_{bi} = \frac{1}{\epsilon_o \epsilon_r} \int_0^{x_d} x \rho(x) dx \quad (3.15)$$

and assuming V_{bi} to be constant:

$$dV = dV_R = \frac{1}{\epsilon_o \epsilon_r} x_d \rho(x_d) dx_d \quad (3.16)$$

From $\rho(x_d)$ the increment in fixed space-charge per unit area is given by:

$$dQ(x_d) = \rho(x_d) dx_d \quad (3.17)$$

allowing the differential capacitance to be defined as:

$$C = A \cdot \frac{dQ}{dV} = \frac{\epsilon_o \epsilon_r A}{x_d} \quad (3.18)$$

Changing V , and hence x_d , changes the value of C ; the convention used herein is that the experimentally measured depletion capacitance is defined as a small signal or differential capacitance. Note that the capacitance is measured by the capacitance meter as the current flowing in the external circuit due to a change dV in bias, where the current relates to the change in dQ ie. the removal of free charge carriers.

The voltage differential of Q (from [3.6]) allows the capacitance to be defined as:

$$C = A \left(\frac{q N_A \epsilon_o \epsilon_r}{2} \right)^{1/2} \left[V - \frac{kT}{q} \right]^{-1/2} \quad (3.19)$$

Thus, a plot of C^{-2} versus V should give a gradient proportional to the doping level and the intercept on the voltage axis should allow determination of the Schottky barrier height.

3.2.3.2 DOPING PROFILES

The doping profile can now be determined by the dependence of the capacitance on reverse bias. Assume the reverse bias is increased from V_R to $V_R + \Delta V_R$, causing a corresponding increase in depletion depth, Δx_d , with the result that the capacitance measured at V_R and $V_R + \Delta V_R$ decreases by ΔC . By similar considerations to (3.16):

$$\Delta V_R = -\frac{qN_A(x_d)}{\epsilon_o \epsilon_r} \cdot x_d \Delta x_d \quad (3.20)$$

assuming $\rho(x_d) = -qN_A(x_d)$ is constant over the increment Δx_d where $\Delta x_d \ll x_d$.

Re-arranging (3.20) gives:

$$N_A(x_d) = -\frac{\epsilon_o \epsilon_r}{q} \cdot \frac{\Delta V_R}{x_d \Delta x_d} \quad (3.21)$$

Differentiating (3.18) with respect to x_d and substituting for Δx_d in (3.21) gives:

$$N_A(x_d) = \frac{C^3}{q\epsilon_o \epsilon_r A^2} \cdot \frac{\Delta V_R}{\Delta C} \quad (3.22)$$

This is the standard equation for determining "net acceptor density" from a measure of the small signal capacitance at reverse bias, V_R and the rate of change of capacitance with reverse bias (from a point-by-point measurement of C versus V_R).

A major assumption made in the previous analysis is that the semiconductor is split into two well defined regions, namely the space-charge region and neutral bulk, separated by an abrupt transition at x_d . Because carrier diffusion will occur from the neutral region into the space-charge region, the depletion edge is non-abrupt and the carrier distribution into the depletion region is given by [3.7]:

$$p(x) = N_A \exp\left\{-\frac{1}{2}\left(\frac{x_d - x}{L_D}\right)^2\right\} \quad \text{for } x < x_d \quad (3.23)$$

where the carrier spilling into the depletion region falls off according to the

characteristic Debye length, L_D given by:

$$L_D = \left\{ \frac{\epsilon_0 \epsilon_r kT}{q^2 N_A} \right\}^{1/2} \quad (3.24)$$

The Debye length is indicative of the abruptness of the carrier distribution at x_d . The depletion approximation with an abrupt transition at x_d is satisfied for $x_d \gg L_D$. Kennedy *et al.* [3.8] recognised that Capacitance-Voltage (C-V) profiling can only measure the free carrier concentration as opposed to the shallow dopant distribution, particularly for non-uniform doping steps. This follows from the fact that free carriers will re-distribute themselves at doping steps and the degree to which features can be resolved may be considered in terms of the characteristic Debye length. Furthermore, Johnson *et al.* [3.9] showed that C-V measurements, for changes in $p(x)$ over distances less than the Debye length, yielded an apparent free carrier distribution, $p^*(x)$ which differed from $p(x)$, where the * denotes apparent values obtained from (3.22). In these circumstances it is difficult to relate $p^*(x)$ to the true free carrier or dopant distribution. The problems associated with C-V measurements through such charge dipoles are considered further in section 3.2.3.4.

Practical measurements of the capacitance and its derivative ultimately limit the accuracy of the values obtained for the carrier distribution; whilst it is necessary to have a sufficiently large capacitance change, ΔC for improved accuracy in $p(x)$, this should not be to the detriment of $\Delta C/\Delta V_R$ and loss of depth resolution.

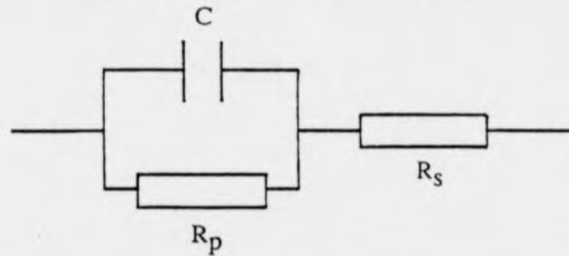
Limitations may also lie with the test diode itself. Apparent capacitance, C_m is measured as the imaginary component of the complex admittance of the sample where [3.10]:

$$C_m = C \left[\left(1 + \frac{R_s}{R_p} \right)^2 + \left(\frac{\omega}{\omega_0} \right)^2 \right] \quad (3.25)$$

The equivalent circuit model is shown in Fig 3.2 where R_s is the series resistance, $G = 1/R_p$ is the parallel conductance and $\omega_0 = 1/CR_s$. For $R_s = 0$, $C_m = C$; however, if $R_s \neq 0$ then $C_m < C$ due to the combination of series and parallel components plus a

Fig 3.2

Schottky diode equivalent circuit representation.



frequency dependant term. As well as using I-V characteristics to determine R_s and R_p , the effect of such components can be monitored from a measure of the phase, θ between the measurement signal current and voltage where:

$$\tan^{-1} \theta = \frac{\text{Im } Y}{\text{Re } Y} = \frac{\omega / \omega_o}{\left(R_s / R_p \right) \left(1 + R_s / R_p \right) + \left(\omega / \omega_o \right)^2} \quad (3.26)$$

Clearly, an accurate measurement of the capacitance is obtained for $R_s/R_p \ll 1$ and $\omega R_s C \ll 1$; this gives a phase approaching 90° as would be expected for a similar analysis of (3.25) excluding R_s .

An in-depth consideration of these and other error sources are detailed by Blood *et al.* [3.11].

3.2.3.3 TRAPPING STATES

Apparent free carrier distributions as discussed in the previous section can be subject to further distortion through the response of trapping states to the measured capacitance and its derivative. The space-charge distributions and associated energy band diagrams for uniformly p-doped material in the presence of uniform acceptor trap and donor trap distributions are shown in Fig 3.3a&b respectively. Assuming the depletion approximation to apply here, abrupt steps are indicated in the space-charge distribution at the depletion edge, x_d and the crossing point of the trap energy level, E_T

Fig 3.3a Energy band diagram and space-charge distribution for a single acceptor trap in uniform p-type material.

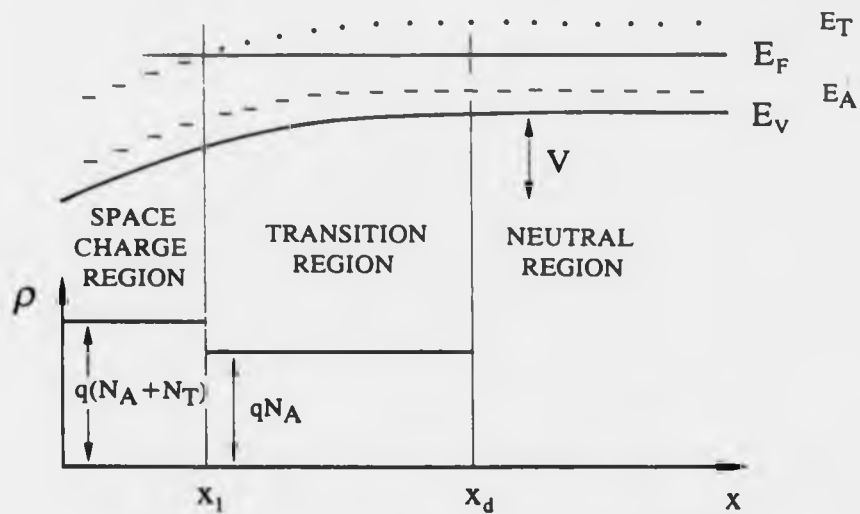
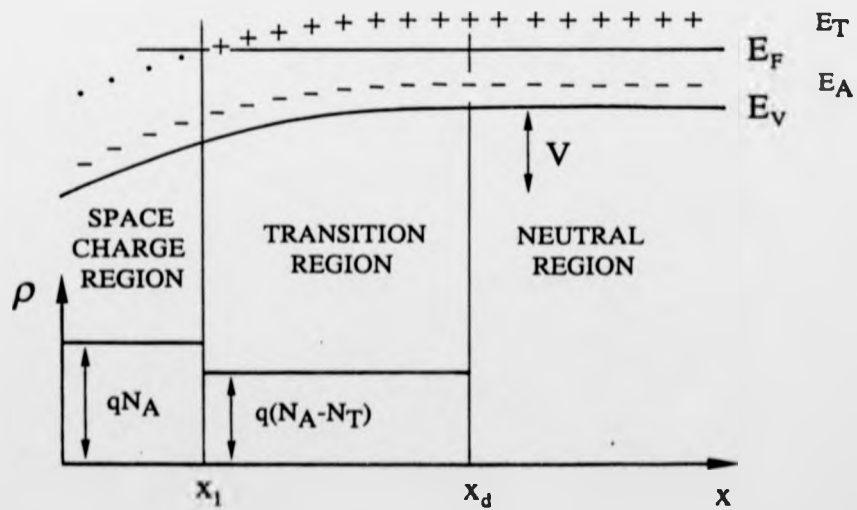


Fig 3.3b Energy band diagram and space-charge distribution for a single donor trap in uniform p-type material.



with the Fermi level, E_F at x_1 . If N_A denotes the shallow acceptor dopant concentration, N_T denotes the trap concentration and traps are considered to ionise for $E_T < E_F$, then the space-charge distributions may be considered as:

$$\text{Acceptor Traps: } 0 < x < x_1 \quad \rho(x) = -q(N_A + N_T)$$

$$x_1 < x < x_d \quad \rho(x) = -qN_A$$

$$\text{Donor Traps: } 0 < x < x_1 \quad \rho(x) = -qN_A$$

$$x_1 < x < x_d \quad \rho(x) = -q(N_A - N_T)$$

x_1 defines the point at which the band-bending is equivalent to the separation between the trap energy, E_T and the Fermi level, E_F . Thus:

$$qV(x_1) = E_v(x_d) - E_v(x_1) = E_T - E_F$$

and using (3.13):

$$\lambda = x_d - x_1 = \left[\frac{2\epsilon_0\epsilon_r}{q^2 N_A} (E_T - E_F) \right]^{1/2} \quad (3.27)$$

where λ defines the transition distance.

We are now in a position to consider the effect of the trapping states on the measured small signal capacitance, as defined in (3.18). The voltage, dV_R will modulate the space charge region at both x_1 and x_d . Free holes are swept away at x_d , increasing the space-charge in the vicinity of x_d by $-qN_A dx$ and $-q(N_A - N_T)dx$ for acceptor and donor traps respectively. At x_1 , holes may be emitted for $E_T < E_F$ if the trap emission rate, e_p is greater than the measurement signal angular frequency, $\omega_{osc}(dV_R)$. During the measurement cycle, both acceptor and donor traps may discharge holes when $E_T < E_F$, contributing $-qN_T dx$ to the space charge then refill for $E_T > E_F$ with a capture rate defined by $c_p(x_1)$. That capture occurs at all highlights the effects of the Debye tail of carriers spilling from the neutral bulk into the space-charge region; indeed, the analysis here chooses to allow the presence of holes for refilling purposes yet ignores their effect in the calculation of the net space-charge. Capture and emission are considered in detail in the next section for capacitance-transient measurements.

At x_d , the net negative fixed charge density is given by (following the notation

of Blood *et al.* [3.12]):

$$-N^-(x_d) = -N_A(x_d) + \sum N_T(x_d) \quad (3.28)$$

where $N_T(x_d)$ is the hole trap concentration at x_d such that for acceptors, $N_T(x_d)=0$ whilst $N_T(x_d)=N_T(x_d)$ for donors. Considering the simplest case of single trap levels, the charge fluctuations at x_1 and x_d (as a consequence of modulation by dV_R) may be expressed (from (3.16) and (3.17)) as:

$$dQ = \rho(x)dx = -q[N^-(x_d)dx_d + u_{osc}N_T(x_1)dx_1] \quad (3.29)$$

$$dV_R = \frac{1}{\epsilon_o \epsilon_r} x \rho(x)dx = -\frac{q}{\epsilon_o \epsilon_r} [N^-(x_d)x_d dx_d + u_{osc}N_T(x_1)x_1 dx_1] \quad (3.30)$$

where u_{osc} denotes the response of the traps such that $u_{osc}=0$ for $e_p < \omega_{osc}(dV_R)$ and $u_{osc}=1$ for $e_p > \omega_{osc}(dV_R)$. From (3.18), the small signal capacitance may be defined as:

$$C = \frac{\epsilon_o \epsilon_r A [N^-(x_d) + u_{osc}N_T(x_1)]}{[N^-(x_d)x_d + u_{osc}N_T(x_1)x_1]} \quad (3.31)$$

where it is assumed that $dx_d = dx_1$. The measured depletion depth is thus given (from (3.18)) as:

$$x_{meas} = \frac{[N^-(x_d)x_d + u_{osc}N_T(x_1)x_1]}{[N^-(x_d) + u_{osc}N_T(x_1)]} \quad (3.32)$$

Clearly for $u_{osc}=0$, traps do not contribute to the measured capacitance and $x_{meas}=x_d$. When $u_{osc}=1$, the traps will cause an increase in the measured capacitance; from (3.32) the measured depletion depth is moved closer to the surface such that $x_{meas} < x_d$. The overall effect is that x_{meas} has become a charge-weighted average between x_1 and x_d when traps are able to respond to the capacitance measurements.

The distortion that will occur in the free carrier concentration obtained using (3.22) will now be considered. For the situation where $e_p > \omega_{osc}(dV_R) > \omega_{mod}(\Delta V_R)$, significant distortion can occur, particularly for non-uniform trap distributions: for an increase in reverse bias such that the rising edge of the trap distribution is modulated by dV_R , the increase in measured capacitance and subsequent decrease in $\Delta C/\Delta V_R$

produces an increase in $p^*(x^*)$ (from (3.22)) and the profile will move back on itself. Once the falling edge of the trap distribution is swept through by the depletion edge, such that all the traps have ionised, $x_{\text{meas}} \rightarrow x_d$, the capacitance measured shows a decrease and $\Delta C/\Delta V_R$ shows a corresponding increase, resulting in a dip in $p^*(x^*)$. These effects were predicted via computer simulation by Hawkins [3.13] and Pittroff [3.14]. Note the use of the x^* to denote apparent depth similar to that employed for apparent free carrier concentration. Furthermore, if the traps are able to respond to the incremental change in reverse bias, ΔV_R such that $e_p > \omega_{\text{mod}}(\Delta V_R)$ then, for a given voltage step, ΔV_R , a correspondingly smaller increment in depletion width will occur if the bias has to ionise additional trapped charge. Analogous to previous considerations made in (3.30) for small signal modulation, dV_R :

$$\Delta V_R = -\frac{q}{\epsilon_o \epsilon_r} [N^-(x_d)x_d \Delta x_d + u_{\text{mod}} N_T(x_1)x_1 \Delta x_1] \quad (3.33)$$

where u_{mod} denotes the response of traps such that $u_{\text{mod}}=0$ for $e_p < \omega_{\text{mod}}(\Delta V_R)$ and $u_{\text{mod}}=1$ for $e_p > \omega_{\text{mod}}(\Delta V_R)$. From (3.21):

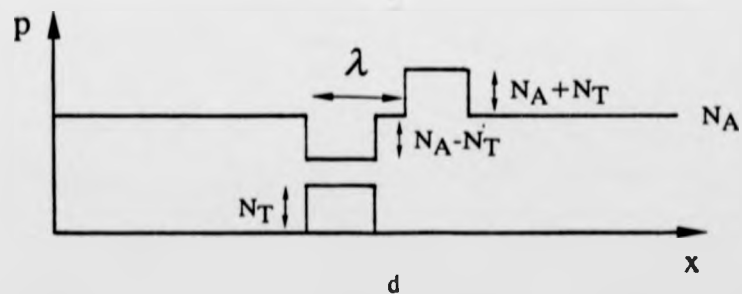
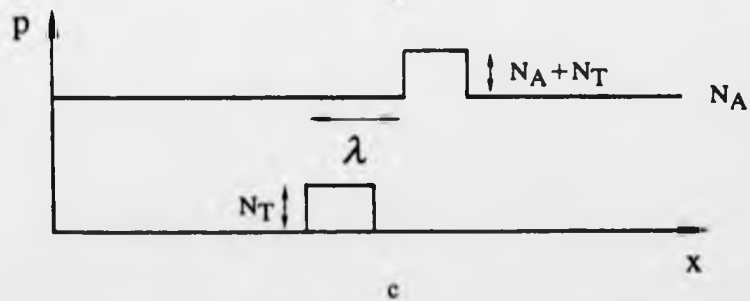
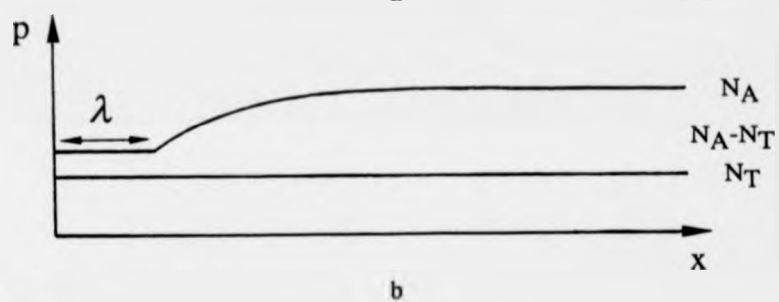
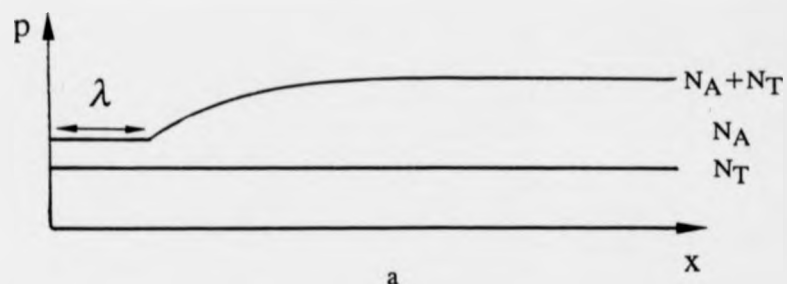
$$p^*(x^*) = N^-(x_d) + u_{\text{mod}} N_T(x_1) \cdot \frac{\Delta x_1}{\Delta x_d} \cdot \frac{x_1}{x_d} \quad (3.34)$$

Clearly for $u_{\text{mod}}=1$, the apparent free carrier concentration has an additional component $N_T(x_1)$ (assuming that $\Delta x_1 = \Delta x_d$ and $x_1 \equiv x_d$ for large reverse bias).

The particular case for $\omega_{\text{osc}}(dV_R) > e_p > \omega_{\text{mod}}(\Delta V_R)$ was considered by Kimerling [3.15] and is illustrated in Fig 3.4a&b for uniform acceptor and donor trap distributions respectively, superimposed on a uniform acceptor dopant distribution. Note that because $\omega_{\text{osc}}(dV_R) > e_p$, $x_{\text{meas}} = x_d$. For small reverse bias such that $E_T > E_F$, $p^*(x^*) = N^-$; for large reverse bias, $p^*(x^*) \rightarrow N^- + N_T$. Thus, the observed effect is an increase in the apparent free carrier concentration with depth. For non-uniform acceptor trap distributions Fig 3.4c, the contribution to $p^*(x^*)$ is not observed until $E_T < E_F$; thus, the block trap distribution is shifted by λ to greater depth. For a non-uniform donor trap distribution Fig 3.4d, $p^*(x^*)$ is a combination of the initial compensation profile, $N_A - N_T(x_d)$ before trap ionisation (for $E_T > E_F$) and the

Fig 3.4

Apparent free carrier distributions for uniform p-type material for a variety of trap distributions: a) uniform acceptor traps, b) uniform donor traps, c) non-uniform acceptor traps and d) non-uniform donor traps.



contribution due to the traps ionising, $(x_1/x_d)N_T(x_1)$ (for $E_T < E_F$), causing the anomalous peak which bears no relation to the true acceptor dopant distribution.

Hence, the apparent free carrier concentration as deduced from (3.22) is subject to distortion in the presence of traps through their contributions to the measured capacitance and its voltage derivative. By use of fixed ω_{osc} and ω_{mod} , the effect of traps may be monitored by changing the measurement temperature, T since $e_p \propto \exp\left(-\frac{1}{T}\right)$. This allows three trap response regimes to be defined thus:

$$e_p > \omega_{osc}(dV_R) > \omega_{mod}(\Delta V_R) \quad \text{LOW FREQUENCY (LF)}$$

$$\omega_{osc}(dV_R) > e_p > \omega_{mod}(\Delta V_R) \quad \text{HIGH FREQUENCY (HF)}$$

$$\omega_{osc}(dV_R) > \omega_{mod}(\Delta V_R) > e_p \quad \text{VERY HIGH FREQUENCY (VHF)}$$

The VHF regime gives $p^*(x^*) = N^-(x_d)$; no change is observed in the apparent free carrier profile for acceptor traps whilst for donor traps, the apparent free carrier profile is compensated.

3.2.3.4 HETEROJUNCTIONS

The limitations imposed by C-V measurements of the apparent free carrier distribution due to the assumption of the depletion approximation have been considered by Kroemer *et al.* [3.16].

The analysis may be extended to the case of a P-p isotype heterojunction as shown in Fig 3.5a. Applying a reverse bias, V_R to a Schottky barrier on the wide band-gap side of the heterojunction, the depletion edge may be considered to extend to x_i Fig 3.5b; on incrementing the bias by ΔV_R such that the depletion now extends to x_{i+1} , a distribution $\Delta p(x')$ of holes are removed from the depletion and accumulation regions. The depletion approximation lumps these contributions together as ΔQ at apparent depth $x' = (x_i + x_{i+1})/2$ Fig 3.5c. Hence, the apparent free carrier distribution, $p^*(x^*)$, determined in this way, bears little resemblance to the true carrier distribution, $p(x)$ Fig 3.5d.

Fig 3.5a Energy band diagram of a P-p isotype heterojunction.

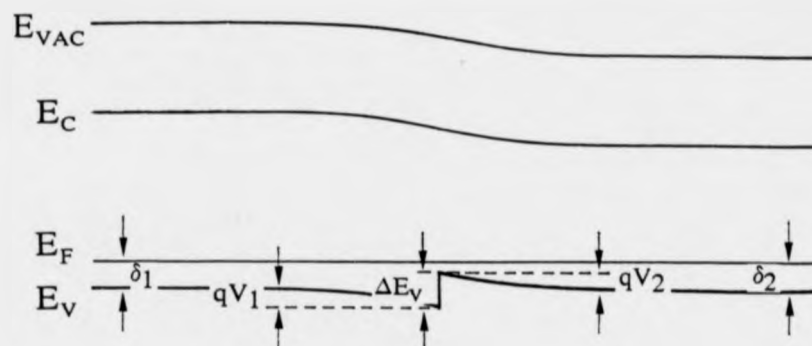


Fig 3.5b Energy band diagram of the same P-p isotype heterojunction shown for two reverse bias situations causing depletion to depths x_i and x_{i+1} .

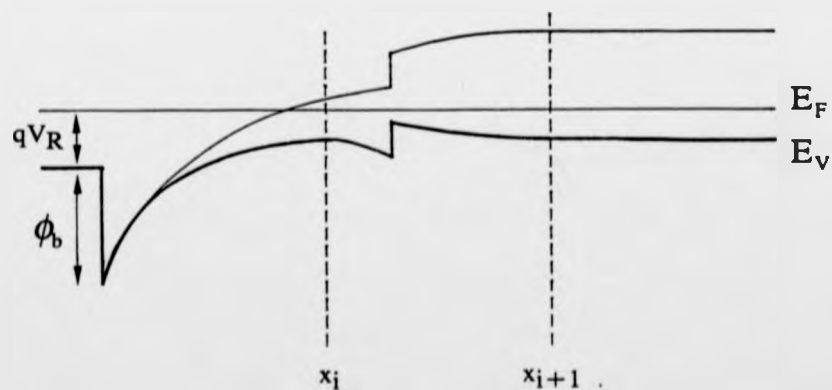


Fig 3.5c

Incremental bias, ΔV_R removes carrier distributions shown here as the shaded regions; the depletion approximation "converts" these distributions into a block form, ΔQ at apparent position, x' .

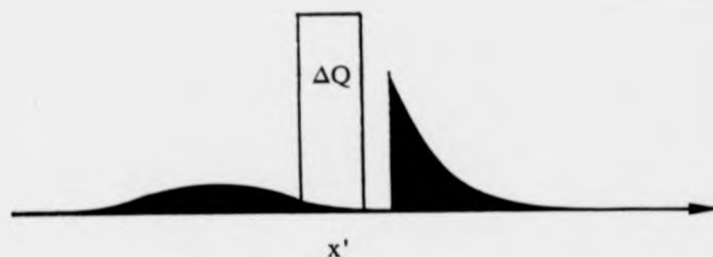
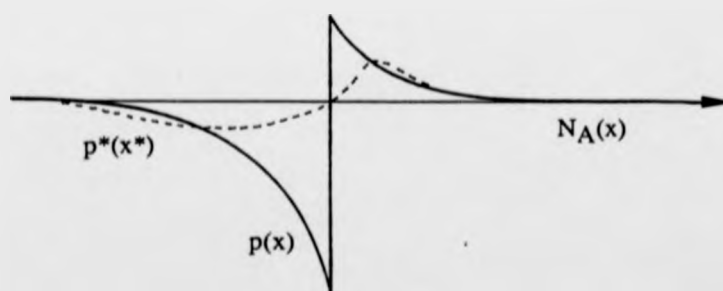


Fig 3.5d

Deviations from the uniform acceptor doping level, $N_A(x)$ illustrating the true hole distribution, $p(x)$ and the measured apparent hole distribution, $p^*(x^*)$.



Despite the differences between $p(x)$ and $p^*(x^*)$, each step in bias, ΔV depletes an amount of charge, ΔQ which is considered to be conserved in moving from $p(x)$ to $p^*(x^*)$ [3.16]; thus, it follows that the total charge is conserved and:

$$\int_a^b p(x) dx = \int_a^b p^*(x^*) dx \quad (3.35)$$

Similarly, the equality of voltage increments, ΔV requires the total moment of the charge distribution also be conserved, giving:

$$\int_a^b x p(x) dx = \int_a^b x^* p^*(x^*) dx^* \quad (3.36)$$

This analysis shows that for free carrier variations on a scale less than a few L_D , the most information that may be obtained from the C-V profile is the sum and the first moment of the carrier distribution. The analysis is therefore of limited use as it does not allow a reconstruction of the true $p(x)$; however, it was further shown by Kroemer *et al.* [3.17] that for the charge dipole set up at a heterojunction, such analysis could be used to extract the band offset and interface charge densities.

From (3.15), the built-in potential, $\Delta\phi$, associated with the charge dipole of the heterojunction, may be defined as:

$$\Delta\phi = \frac{q}{\epsilon_0 \epsilon_r} \int_{x_1}^{x_2} (p(x) - N_A(x))(x - x_1) dx \quad (3.37)$$

and from (3.36):

$$\Delta\phi = \frac{q}{\epsilon_0 \epsilon_r} \int_{x_1}^{x_2} (p^*(x^*) - N_A^*(x^*))(x^* - x_1) dx^* \quad (3.38)$$

where the * denotes apparent values inferred from the apparent free carrier distribution such that $N_A^*(x^*)$ is the apparent background doping level at apparent position, x^* (taken from the uniform $p^*(x^*)$ either side of the heterojunction) and x_1 is the heterojunction position; note the integration limits are defined either side of the heterojunction.

In the presence of ionised traps, $N_T(x_1)$ at x_1 , the space charge density is

modified from that used in (3.38):

$$\rho(x^*) = q(p'^*(x^*) - N_A^*(x^*) \pm N_T(x_I)) \quad (3.39)$$

The + indicates donor traps whilst the - indicates acceptor traps. Note that $p'^*(x^*)$ has changed from $p^*(x^*)$ due to the presence of the traps. From the condition for charge neutrality, it is possible to extract the interface charge density:

$$\sigma_I = \pm \int_{x_1}^{x_2} N_T(x_I) dx^* = - \int_{x_1}^{x_2} (p'^*(x^*) - N_A^*(x^*)) dx^* \quad (3.40)$$

The corresponding built-in potential is now given by:

$$\Delta\phi = \frac{q}{\epsilon_0 \epsilon_r} \int_{x_1}^{x_2} (p'^*(x^*) - N_A^*(x^*) \pm N_T(x_I))(x^* - x_I) dx^* \quad (3.41)$$

It is important to note this is equivalent to (3.38) if $N_T(x_I)$ is symmetrically distributed about x_I and the resultant distortion to the apparent free carrier distribution, $p'^*(x^*)$ is similarly symmetrical about x_I .

The general case for ionised traps may be given by:

$$\rho(x^*) = q(p'^*(x^*) - N_A^*(x^*) \pm N_T^*(x^*)) \quad (3.42)$$

If the ionised trap distribution is close to but not at x_I , it is incorrect to use (3.38) to determine the built-in potential of the heterojunction since $p^*(x^*)$ has been modified to $p'^*(x^*)$. Thus, a correction is required in the presence of ionised traps close to the heterojunction in order to determine $\Delta\phi(0)$ (equivalent to (3.38)), the zero denoting the absence of ionised traps. Leu *et al.* [3.18] considered this problem and, although not immediately obvious from their work, provided a correction term:

$$p^*(x^*) = p'^*(x^*) \pm N_T^*(x^*) \quad (3.43)$$

where $p^*(x^*)$ is a measure of the apparent free carrier distribution due to the ionised acceptor dopants alone. This gives:

$$\Delta\phi(0) = \Delta\phi(\sigma) \pm \frac{q}{\epsilon_0 \epsilon_r} \int_{x_1}^{x_2} N_T^*(x^*)(x^* - x_I) dx^* \quad (3.44)$$

where $\Delta\phi(\sigma)$ is evaluated from (3.38) substituting $p'^*(x^*)$ for $p^*(x^*)$ and represents the built-in potential in the presence of ionised traps close to the heterojunction. If $N_T^*(x^*)$

is known and falls within the integration limits, correction can be made to the measured $\Delta\phi$.

This makes it possible to extract the valence band offset, ΔE_V since the built-in potential, $\Delta\phi(0)$ associated with the heterojunction alone may be defined as:

$$q\Delta\phi(0) = \Delta E_V + \delta_2 - \delta_1 \quad (3.45)$$

where δ_1 and δ_2 represent the separation of the Fermi level from the valence band edge in the shallow and deep bulk semiconductor regions respectively either side of the heterojunction (see Fig 3.5a).

3.2.3.5 SIMULATIONS

Because of the resolution limitations that can occur in C-V profiling and subsequent distortions due to trap distributions, interpretation of the apparent free carrier distributions can become very difficult. For this reason, computer simulations have become increasingly used to maximise information in the form of an iterative matching between experiment and simulation. The model employed in this work was developed at UMIST by Hawkins [3.13] and is based on a "no depletion approximation" model. Analysis was developed relating C and $\Delta C/\Delta V_R$ to the space-charge density, ρ which could be both integrated and differentiated with respect to V. Thus by breakdown of ρ into fixed charge and mobile carriers, analytically determined values for C and $\Delta C/\Delta V_R$ could be substituted into (3.22) to provide the apparent free carrier distribution for a range of voltage increments corresponding to deeper depletion. Whilst the model incorporates band offsets, trap and dopant distributions of variable occupancy and degenerate and non-degenerate statistics, certain limitations are evident. Trap response at the measurement signal frequency may be simulated, allowing the significant distortion discussed for the LF response regime in section 3.2.3.3 to be seen. However, trap distributions cannot overlap and the program will only simulate carrier profiles either in the LF regime (assuming all traps follow the measurement signal frequency) or HF regime (assuming no traps can follow the measurement signal frequency). Minority carrier effects and resistive voltage drops are also ignored.

3.2.4 DEEP LEVELS

Impurity and defect states in semiconductors may be considered to introduce shallow and deep energy levels within the band-gap. Shallow levels are introduced by simple hydrogenic impurities close to the band edge such that the carriers are weakly bound and are likely to be thermally ionised at 300K. Of greater importance are deep levels which reside at energies $> 0.05\text{eV}$ from the band edge and are not necessarily ionised at 300K. It is these levels which were considered in the section on C-V profiling as trapping levels and will now be discussed further. Note that the following analysis is based upon discrete non-interacting trapping levels as a result of point defects within the semiconductor material.

3.2.4.1 CARRIER KINETICS

The processes determining the occupancy of deep levels are those of capture and emission of electrons and holes Fig 3.6. In thermal equilibrium, these processes should

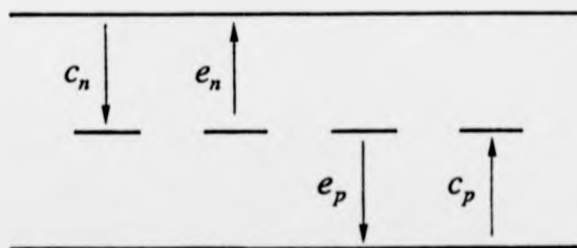


Fig 3.6 Deep level occupancy as determined by carrier transitions between band edges and deep levels.

balance; defining p_T as the number of states occupied by holes then:

$$\frac{dp_T}{dt} = (e_n + c_p)(N_T - p_T) - (c_n + e_p)p_T = 0 \quad (3.46)$$

where e_n , e_p , c_n , c_p are the respective emission and capture rates for electrons (n) and holes (p) and N_T is the total trap concentration. Hole occupancy is considered as the material under investigation is doped p-type; this is readily rewritten in terms of states

unoccupied by electrons since $p_T = N_T - n_T$, where n_T is the number of states occupied by electrons.

Rearranging (3.46) and using Fermi-Dirac considerations to define hole fractional occupancy gives:

$$\frac{e_p}{c_p} = \frac{g_1}{g_0} \cdot \exp\left(\frac{E_F - E_T}{kT}\right) \quad (3.47)$$

for a deep state of energy, E_T above the valence band edge with degeneracy, g_1 when empty of holes and g_0 when occupied. This illustrates the dynamic nature of e_p relative to c_p and noting that $c_p = \sigma_p < v_{th} > p$, where σ_p defines the hole capture cross section, $< v_{th} >$ the mean thermal velocity and p the free hole concentration [3.19], the hole emission rate may be given by:

$$e_p(T) = \sigma_p < v_{th} > \frac{g_1}{g_0} N_V \exp\left(-\frac{E_T - E_V}{kT}\right) \quad (3.48)$$

where N_V is the density of hole states.

3.2.4.2 TRANSIENT RESPONSE

The general rate equation (3.46) defines the time dependence of the hole occupancy of the trap which may be rewritten:

$$\frac{dp_T}{dt} = a(N_T - p_T) - bp_T \quad (3.49)$$

where $a = \sum$ rates of hole gain ($e_n + c_p$) and $b = \sum$ rates of hole loss ($c_n + e_p$). If $p_T = p_T(0)$ at $t=0$, then the general solution of (3.49) is:

$$p_T(t) = \frac{a}{a+b} \cdot N_T - \left\{ \frac{a}{a+b} \cdot N_T - p_T(0) \right\} \exp[-(a+b)t] \quad (3.50)$$

The steady state occupancy ($t=\infty$) is given by $p_T(\infty) = \frac{a}{a+b} \cdot N_T$ and thus:

$$p_T(t) = p_T(\infty) + \{p_T(0) - p_T(\infty)\} \exp\left[-\frac{t}{\tau}\right] \quad (3.51)$$

where the time constant, $\tau = (a+b)^{-1} = (e_n + c_n + e_p + c_p)^{-1}$. $p_T(t)$ shows that if the occupancy is momentarily perturbed from $p_T(\infty)$ to $p_T(0)$, relaxation to an equilibrium occupancy, $p_T(\infty)$ will occur with a rate constant $(a+b)$.

The study of carrier capture and emission properties of such deep levels form an important class of analysis techniques. Use of a Schottky barrier allows the capacitance transient associated with the return to equilibrium of the occupation of deep levels (following an initial non-equilibrium condition) to be monitored; this is to be considered later. If the Schottky barrier is considered on p-type material, a majority carrier trap will fill by hole capture; this is achieved by reducing the reverse bias such that holes are injected into the previously depleted region and are available for capture onto deep levels. By then increasing the reverse bias once again, a non-equilibrium situation is created and the traps emit with a characteristic rate defined by (3.48) to re-establish the equilibrium occupancy. Minority carrier traps are considered inactive, assuming no source of electrons are available.

Certain considerations should now be made before the relationship between capacitance transients and trap occupancy are detailed. Consider the band bending for a small reverse bias (V_{FILL}) shown in Fig 3.7a, with acceptor dopant concentration, N_A and donor trap concentration, N_T energetically positioned at E_T above the valence band edge. Beyond the depletion edge at x_0 , $c_p > e_p$ and traps are fully occupied. Within the depletion region, the free hole concentration falls off according to (3.23); this causes a decrease in the capture rate from the definition of c_p . The equilibrium occupancy is shown in Fig 3.7b, decreasing with distance into the depletion region; from (3.47), $c_p(x_2) \equiv e_p$ and the equilibrium occupancy $p_T(x_2) = N_T/2$. If L_D is small with respect to x_0 , $p(x)$ changes rapidly and the transition in trap occupancy can be considered as an abrupt step at x_2 (analogous to considerations made in the previous section concerning the depletion approximation), where $x_2 = x_0 - \lambda$ (from (3.27)); in this case $p_T(x_2) \rightarrow N_T$.

For $x > x_0$, $p(x)$ is uniform and capture is characterised by the uniform rate constant, c_p whereas for $x < x_0$, the capture rate decreases with distance ($x_0 - x$) and, as a consequence, the time required to fill the traps to an equilibrium occupancy is longer compared to that for $x > x_0$. From the instant that the bias is reduced to V_{FILL} , the point at which occupancy $N_T/2$ is achieved moves slowly from x_0 to x_2 . The time this

Fig 3.7a Energy band diagram for uniform p-type material with an applied reverse bias, V_{FILL} intended to fill all trapping states for $x > x_2$.

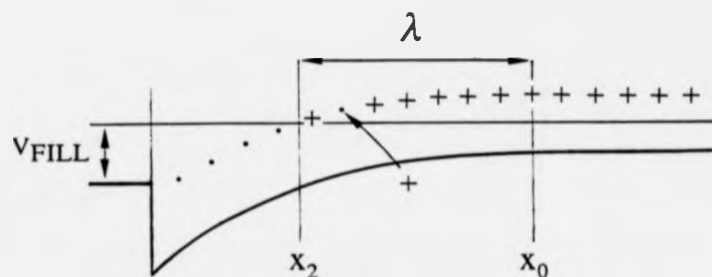


Fig 3.7b Trap occupancy for the cases of fill, (V_{FILL}) and reverse, (V_{REV}) applied measurement bias.

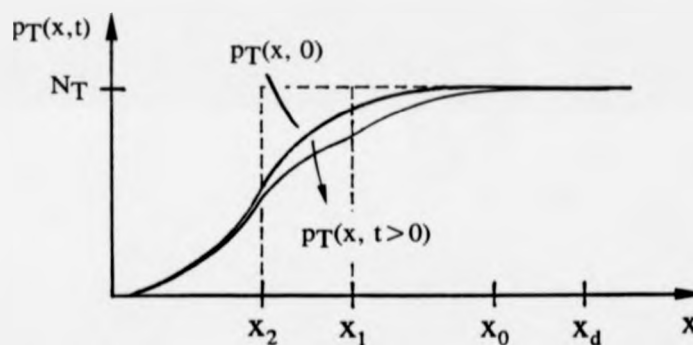
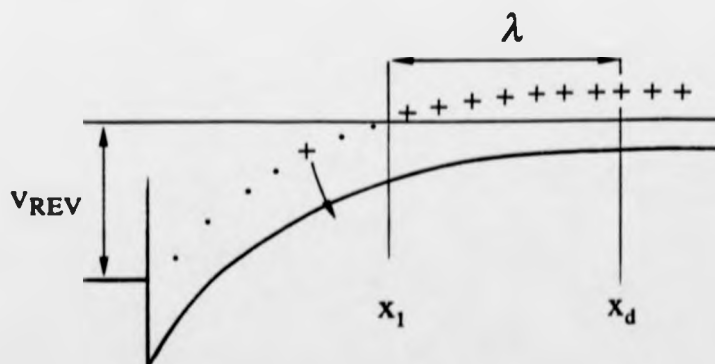


Fig 3.7c Energy band diagram for uniform p-type material with an applied reverse bias, V_{REV} intended to induce trap emission from states for $x_2 < x < x_1$.



takes is $\cong 1/e_p$ (see (3.61)) and hence the definition of a well defined transition region of width λ is only applicable in the steady state.

In Fig 3.7a, the traps are considered filled with holes for $x > x_2$. If a large reverse bias, V_{REV} is now applied producing depletion to depth x_d , changes in occupancy will occur Fig 3.7c. Traps in the region $x < x_1$ now have $E_T < E_F$ and so emission dominates. For $x > x_1$, capture dominates and the traps remain occupied (assuming an abrupt transition at x_1).

These considerations are of importance since they can result in deep level concentrations being underestimated and the region over which emission occurs becoming ill-defined.

3.2.4.3 CAPACITANCE TRANSIENTS AND DEEP LEVELS

The relation between measured steady-state capacitance and trap concentration has been discussed in the previous section 3.2.3.3. For carrier emission from deep levels, the resulting change in space-charge density will produce a capacitance change. This will now be considered for the case of a fixed reverse bias, V_{REV} causing the initial non-equilibrium situation and the resultant change in space-charge density $\rho(x,t)$ towards equilibrium.

Consider the simplest case for deep levels in p-type material where they will exist in one of two charge states. Acceptor deep levels can be negatively charged or neutral whilst donor traps can be positively charged or neutral. Thus, the change in space-charge density as a function of time, following the application of a reverse bias V_{REV} , can be defined as:

$$\rho(x,t) = -q(N_A(x) + [N_T(x) - p_T(x,t)]) \quad \text{Acceptor deep levels}$$

$$\rho(x,t) = -q(N_A(x) - p_T(x,t)) \quad \text{Donor deep levels}$$

From Poissons equation and assuming uniform distributions of N_A and N_T :

$$V(t) = \frac{1}{\epsilon_0 \epsilon_r} \int_0^{x_d(t)} x \rho(x, t) dx \quad (3.52)$$

$$= -\frac{q}{2\epsilon_0 \epsilon_r} \{N_A x_d^2(t) + N_T x_1^2(t) - p_T(t)[x_1^2(t) - x_2^2(t)]\}$$

The case of acceptor traps is illustrated here following the approach of Blood *et al.* [3.20]; the analogous situation for donor traps yields the same answer for capacitance transient and trap concentration for $N_T < N_A$. By finding the time derivative of (3.52) and noting $dV(t)/dt=0$, then the time dependence of the depletion width and consequently, the depletion capacitance may be found. Thus the capacitance transient, $\Delta C(t)$ may be defined as:

$$\frac{\Delta C(t)}{C} = \frac{C(\infty) - C(t)}{C} = -\frac{1}{2} \left\{ \frac{x_1^2 - x_2^2}{x_d^2} \right\} \frac{p_T(\infty) - p_T(t)}{N_A} \quad (3.53)$$

From (3.51), the general case for emission from a majority carrier trap with $p_T(0)=N_T$ and $p_T(\infty)=0$ may be written:

$$\Delta C(t) = \Delta C_0 \exp(-e_p t) \quad (3.54)$$

$$\text{where } \frac{\Delta C_0}{C} = \frac{1}{2} \left\{ \frac{x_1^2 - x_2^2}{x_d^2} \right\} \cdot \frac{N_T}{N_A} \quad (3.55)$$

Thus the capacitance transient is an exponential function of time, with an amplitude directly related to the trap concentration. Use of (3.55) in conjunction with (3.27) allows trap distributions to be determined by judicious choice of fill and reverse measurement biases; this is exploited by the DLTS technique which will now be discussed. However, one should be aware that if the restrictions in deriving (3.54) are not met, then the capacitance transient cannot be described by a simple exponential.

3.2.4.4 DEEP LEVEL TRANSIENT SPECTROSCOPY

Lang [3.21] introduced a very convenient way of measuring emission rates based on monitoring the capacitance transients as a function of temperature (from (3.48) the emission rate varies rapidly with temperature), which has become known as Deep Level

Transient Spectroscopy (DLTS). A boxcar integrator was used to measure the capacitance at two different times, t_1 and t_2 , resulting in an output signal, S given by:

$$S = k[C(t_1) - C(t_2)] \quad (3.56)$$

where k accounts for the gain of the system. A series of capacitance transients are shown in Fig 3.8; the quantity S is maximised for a time constant τ of the order t_1, t_2 . This may be written explicitly for the condition $dS/d\tau = 0$ such that:

$$\tau = \frac{t_2 - t_1}{\ln(t_2/t_1)} = e_p(T_m)^{-1} \quad (3.57)$$

where e_p is the hole emission rate at temperature, T_m . Thus, the emission rate corresponding to the maximum of a trap peak, as observed by this technique, is a precisely determined quantity; this may be used along with the temperature corresponding to the peak maxima, to determine the deep level activation energy, $E_{act} = E_T - E_V$. Since $\langle v_{th} \rangle N_C \propto T^2$, (3.48) may be written as:

$$\ln\left(\frac{e_p}{T^2}\right) = c - \frac{E_{act}}{kT} \quad (3.58)$$

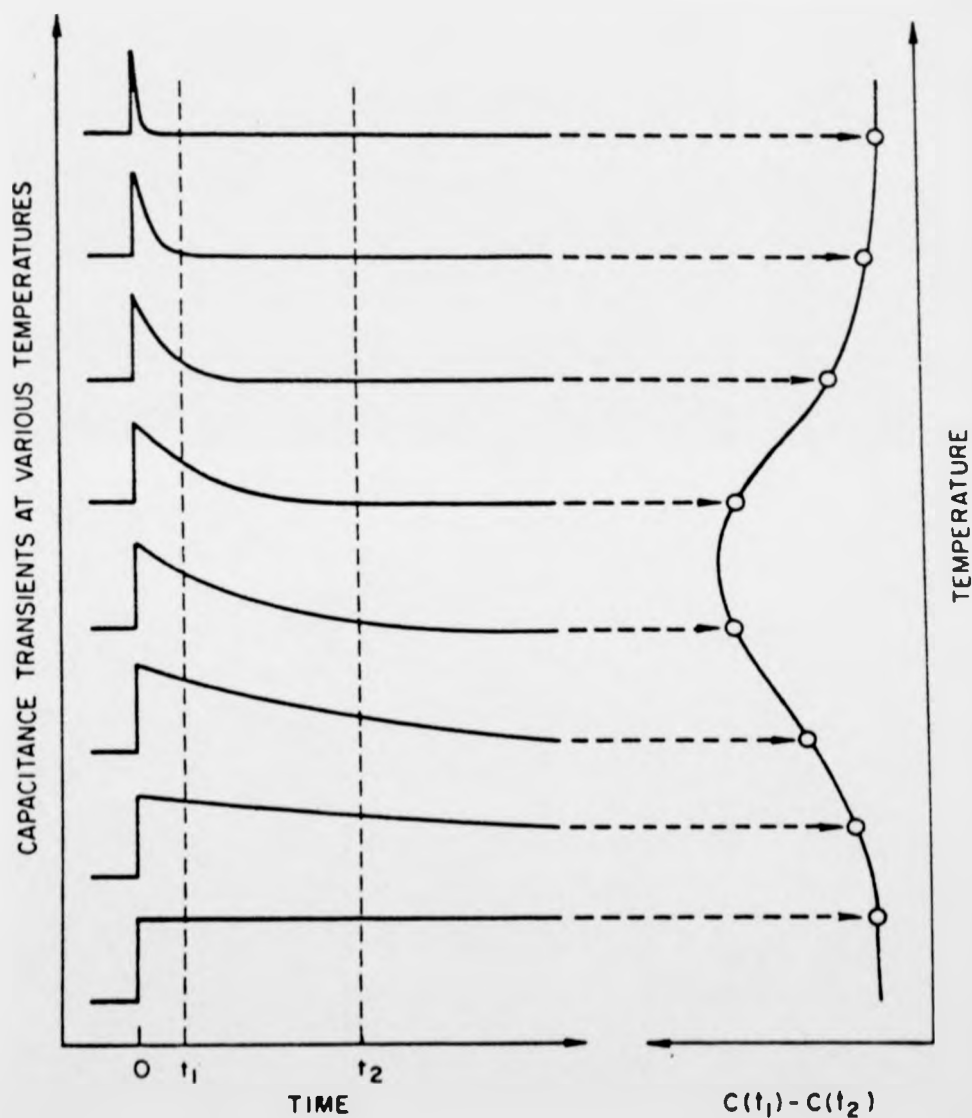
where c is a constant; a plot of $\ln(e_p/T^2)$ versus $1/T$ is known as an Arrhenius or activation plot. However, the activation energy determined here is not the actual energetic displacement of the deep level from the valence band edge since both the prefactor and E_{act} are likely to be functions of temperature. Thus, in reality, it is better to consider the rate of thermal emission of holes in terms of a change in the Gibbs free energy of ionisation, ΔG from (3.48) [3.22]:

$$e_p(T) = s_p(T) N_V(T) \langle v_{th}(T) \rangle \exp\left[\frac{\Delta S}{k}\right] \exp\left[-\frac{\Delta H}{kT}\right] \quad (3.59)$$

where the thermodynamic identity $\Delta G(T) = \Delta H - T\Delta S$ for changes in enthalpy, ΔH and entropy, ΔS is invoked. Assuming the prefactor to be temperature independent, the slope of the Arrhenius plot gives ΔH ; however, this is not equivalent to $\Delta G(T) = E_T(T) - E_V(T)$ because of the temperature dependence of the $\Delta G(T)$ term. The ΔH value is an average over the measurement temperature range and the enthalpy

Fig 3.8

Illustration of the boxcar integrator response for various capacitance transients; the signal is maximised for a transient time constant of the order t_1, t_2 (after [3.21]).



term obtained at temperature, T is given by $\Delta H(T) = \Delta G(T) + T\Delta S$. This is the $T=0$ intercept of the tangent to the $\Delta G(T)$ curve ie. $\Delta G(0)$.

Such considerations have to be made in order to compare to deep level energies determined via isothermal optical methods and in the determination of the capture cross section from the Arrhenius plot. However, E_{act} obtained from the conventional analysis may be considered a fingerprint to the identity of the deep level when compared to the extensive literature on DLTS and supplemented by additional characterisation techniques.

3.2.4.5 MAJORITY CARRIER CAPTURE

The most common method of studying majority carrier capture at deep levels is to perform DLTS, stabilised at the peak temperature, and monitor the change in peak height as a function of filling time, t_F . The DLTS signal is proportional to the number of trapped holes at the beginning of the emission transient, $p_T(0)$ which is equivalent to the trap occupancy $p_T(t_F)$ at the end of the filling time. The DLTS emission transient may be defined as a function of time from (3.53):

$$\frac{\Delta C(t=0)}{C} = \frac{1}{2} \left\{ \frac{x_1^2 - x_2^2}{x_2^2} \right\} \cdot \frac{p_T(t_F)}{N_A} \quad (3.60)$$

assuming that the emission observation time, t is sufficiently long that the density of trapped holes, $p_T(t=\infty)$ is negligible at the start of the next capture pulse. From (3.51):

$$p_T(t_F) = N_T \left\{ 1 - \exp\left(-\frac{t_F}{\tau}\right) \right\} \quad (3.61)$$

The number of holes captured is exponential in filling time, where it is assumed that $p_T(t_F=\infty) = N_T$. As the filling pulse length is reduced, a point is reached where the traps fail to fill completely; thus the fraction of traps not filled at time, t_F is given by:

$$1 - \frac{p_T(t_F)}{p_T(\infty)} = 1 - \frac{\Delta C(t_F)}{\Delta C(\infty)} = \exp\left\{-\frac{t_F}{\tau}\right\} \quad (3.62)$$

Hence a plot of $\ln\left[1 - \frac{\Delta C(t_F)}{\Delta C(\infty)}\right]$ versus t_F will allow determination of the hole capture cross section, since the slope gives $\tau^{-1} = p < v_{th} > \sigma_p$.

The above analysis is based on non-interacting deep level states; in the case of dislocations, carrier capture is considered to proceed subject to the occupancy of the deep levels. The charge on the deep levels gives rise to a macroscopic electrostatic barrier $q\Phi$ (see section 2.5) and thus the concentration of free holes with sufficient energy to surmount the potential barrier and reach the trapping site is described by $p = p_0 \exp(-q\Phi/kT)$. The rate equation for hole capture may be written (from (3.46), assuming c_p to be the dominant mechanism):

$$\frac{dp_T}{dt_F} = \sigma_p < v_{th} > p(N_T - p_T) \exp\left\{-\frac{q\Phi(t_F)}{kT}\right\} \quad (3.63)$$

The solution to this is of the form [3.23]:

$$p_T(t_F) = K \ln[t_F] \quad (3.64)$$

where K is a constant. Hole trap occupancy increases with the logarithm of filling time; however, no valid capture-cross section may be determined in this case.

3.2.4.6 LIMITATIONS

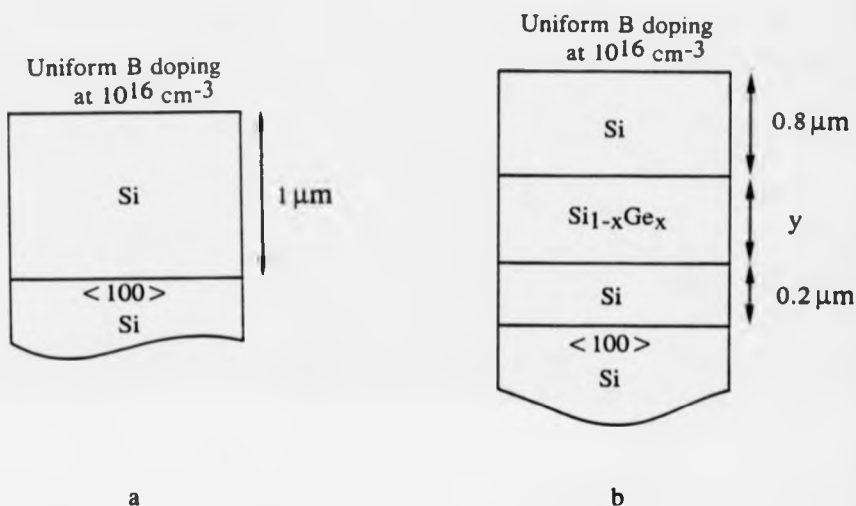
The preceding analysis is based on the fact that $N_T \ll N_A$ in order that the capacitance transient is described by an exponential. For high trap concentrations [3.24], alloy systems [3.25] and extended defects [3.26], non-exponential transient behaviour has been observed. In these situations, care has to be taken in the interpretation of the results. Trap profiling and capture cross section measurements are subject to error through the ill-defined region over which trap response is assumed to occur (through incomplete capture and emission from the deep levels, due to the Debye tail of carriers). The mixing of trap signals due to similar emission rates can produce broadened deep level spectra and it becomes difficult to deconvolute the signals [3.27]. Other problems relate to the device itself i.e. leakage currents, series resistance [3.28] and instrumentation shortcomings [3.29].

3.2.5 LAYER GROWTH AND EXPERIMENTAL SET-UP

Samples were grown in a Vacuum Generators V90S MBE system at the University of Warwick. Substrates used in this work were 100cm diameter p^+ (0.001-0.012 Ω cm) $\langle 100 \rangle$ CZ Si. No chemical precleans were used as these were found to have little significant effect on epilayer quality. Substrates were subjected to an in-situ 860°C Si flux clean prior to growth; substrate temperature was then reduced to the required value and growth continued, so avoiding sudden changes in temperature or growth rate. Growth was carried out at either 530°C or 630°C and uniform B-doping at 10^{16} cm^{-3} used throughout for both Si and Si/Si_{1-x}Ge_x/Si structures, shown in Fig 3.9a&b respectively, used in this work. The doping level was chosen such that rectifying Schottky contacts could be achieved; relatively thick structures were employed to allow sufficient resolution of the heterojunction features (from the apparent free carrier distributions) according to L_D and the unknown distortion that might be encountered in the vicinity of the heterojunction. Whilst the Si_{1-x}Ge_x layers were grown beyond the equilibrium critical thickness, h_c (from section 2.3), X-ray characterisation (see section 3.3.3 and 5.4) indicated the Si/Si_{1-x}Ge_x/Si layers to be in the metastable strained regime. Wafers were cleaved into 1cm² sections and 1mm diameter Ti Schottky contacts sputtered onto the episurface - note no preclean was used before contacts were deposited. Without breaking vacuum, Al was deposited onto the Ti contacts. Ohmic contacts to the highly doped p^+ substrate were made using Al deposited on the wafer backside. These samples were subsequently stuck onto contact-patterned mica sheets, allowing the Schottky contacts to be bonded.

Samples were then mounted onto the Cu stage of the cryostat using heat sink compound on the mica backside to provide good thermal contact. The cryostat employed a platinum resistor to monitor the sample temperature during the heating or cooling cycles; cooling was provided by liquid N₂, with its flow rate adjusted by a temperature controller. I-V and C-V measurements were made using an HP 4140A DC Voltage source and an HP 4192A Low Frequency impedance analyser at 1Mhz respectively, with control and data acquisition provided by an HP 9600 microcomputer.

Fig 3.9 Schematic diagrams of the sample structures used in this study: a) Si and b) Si/Si_{1-x}Ge_x/Si. Sample details are given in the table underneath.



Sample Identity	Growth Temperature T_s (°C)		Ge Fraction x	Layer Thickness y (μm)
24/19 (b)	630	(0.15 nm s ⁻¹)	0.1	0.5
24/21 (a)	530	"	-	-
24/27 (b)	"	"	0.08	0.45
28/15 (b)	"	"	0.03	0.5
28/16 (b)	"	"	0.2	0.1
28/17 (b)	"	"	0.12	0.25
28/18 (b)	"	"	0.14	0.25
28/20 (a)	"	"	-	-
28/21 (b)	"	"	0.1	0.4
28/22 (b)	630	"	0.06	0.5

A Biorad-Polaron DL4600 Deep Level Transient Spectroscopy system was used to generate a repetitive pulse sequence, with transient sampling at times t_1 , t_2 and t_3 providing two rate window signals for a single temperature scan. The bias conditions (1V measurement window) were provided by an HP 8116A Pulse Generator; this was also used in conjunction with a fast pulse interface unit to provide capture measurements by applying a varying fill pulse between 3ms-500ns to the sample. Capacitance measurements were provided by a modified Boonton 72B capacitance meter.

3.3 STRUCTURAL ANALYSIS

3.3.1 TRANSMISSION ELECTRON MICROSCOPY

Transmission electron microscopy (TEM) provides the most direct way of imaging defects in Si layers with very high resolution. High energy electrons are accelerated to potentials between 100-2000kV and focused by a magnetic condenser lens system to form a spot 100-0.1 μ m in diameter. This beam incident on a suitably prepared sample (thinned and in cross-section) will undergo diffraction according to the geometrical requirements of Bragg's law. Electrons which emerge from the back of the sample are then focused by an objective lens onto a fluorescent plate. The TEM image formed is the result of those transmitted electrons which have passed through the sample without suffering significant scattering. The contrast is provided by changes in crystallographic orientation or structure since electrons will be scattered by these regions; this provides a direct image of the local defect or disorder and can provide a resolution down to 0.2nm. For defect analysis, information on the diffraction conditions are obtained by operating the microscope to produce a diffraction pattern for particular defects observed in the image mode. This has allowed extensive studies into the nucleation and propagation of dislocations in semiconductors [3.30-32], providing valuable information particularly on the modes of relaxation in strained semiconductor systems.

3.3.2 DEFECT REVEAL ETCH TECHNIQUES

Preferential etching using a chemical etch for defect delineation is a quick yet extremely useful method of determining defect densities and types in semiconductor material. The sample is immersed in an etchant (in this work, a dilute Schimmel etch $1.5 \text{ H}_2\text{O} : 1 \text{ CrO}_3 (0.75\text{M}) : 2 \text{ HF}$ [3.33] was used) which dissolves the semiconductor matrix at a controlled rate, whilst defects and impurities are exposed at a different rate, resulting in well defined contours on the etched surface. By use of optical microscopy employing Nomarski interference contrast, the defects may be identified and their areal density determined.

It is important to realise that for insufficient defect delineation, the process of identification becomes difficult and hence defect count can be in error.

3.3.3 X-RAY DIFFRACTION

Double crystal X-ray diffraction provides a powerful probe to study the relaxation of strained epilayers. X-rays are directed onto a calibration crystal which conditions the incident beam to provide higher angular resolution; this beam is then incident onto the sample crystal which is "rocked" through a range of angles which includes the Bragg angle for the specimen. This provides a rocking curve which shows the main diffraction peaks, according to Bragg's law, plus higher order diffraction features. For strained layer growth of $\text{Si}_{1-x}\text{Ge}_x$ onto cubic Si, the lattice spacing perpendicular to the growth direction is different for $\text{Si}_{1-x}\text{Ge}_x$ as compared to Si; this results in two main diffraction peaks being observed on the rocking curves. From the separation of these main peaks, layer compositions and thicknesses may be determined. Interfacial dislocations are detected by measuring the corresponding strain or change in lattice constant, a_0 ; this permits a strain resolution up to $(\Delta a_0/a_0) \cong 10^{-4}$ to be observed and hence provides a relatively sensitive technique for detecting the onset of relaxation. Diffracting planes will suffer distortion through the formation of dislocations and, as a result, diffraction peaks are broadened. Further information may be found in the work of Powell [3.34].

REFERENCES

- 3.1 W. Schottky Naturwiss 26 (1938) 843
- 3.2 J. Bardeen Phys. Rev. 71 (1947)
- 3.3 E. H. Rhoderick and R. H. Williams "Metal-Semiconductor contacts" 2nd Ed. (Clarendon Press, Oxford 1988) 89-124
- 3.4 A. S. Grove "Physics and Technology of Semiconductor Devices" (John Wiley and Sons Inc., New York 1967) Chapter 6
- 3.5 G. W. Neudeck "The pn junction diode" (Addison Wesley Publishing Co., Massachusetts 1983) Chapter 2
- 3.6 P. Blood and J. W. Orton
"The Electrical Characterisation of Semiconductors: Majority Carriers and Electron states" (Academic Press Inc., San Diego 1992) 231
- 3.7 P. Blood Semicond. Sci. Technol. 1 (1986) 7
- 3.8 D. P. Kennedy and R. R. O'Brien IBM J. Res. Develop. 13 (1969) 212
- 3.9 W. C. Johnson and P. T. Panousis IEEE Trans. Elec. Dev. ED-18 (1971) 965
- 3.10 T. Humer-Hager Semicond. Sci Technol. 3 (1988) 553
- 3.11 (as 3.6) 315-331
- 3.12 (as 3.6) 297-299
- 3.13 I. D. Hawkins PhD. Thesis UMIST (1989)
- 3.14 W. Pittroff Phys. Stat. Sol. (a) 120 (1990) K53
- 3.15 L. C. Kimerling J. Appl. Phys. 45 (1974) 1839
- 3.16 H. Kroemer and W. -Yi. Chien Sol. St. Elec. 24 (1981) 655
- 3.17 H. Kroemer, W. -Yi. Chien, J. S. Harris Jr. and D. D. Edwall
Appl. Phys. Lett. 36 (1980) 295
- 3.18 L. Y. Leu and S. R. Forrest J. Appl. Phys. 64 (1988) 5030
- 3.19 G. L. Miller, D. V. Lang and L. C. Kimerling
Ann. Rev. Mater. Sci. 7 (1977) 377
- 3.20 (as 3.6) 371-375
- 3.21 D. V. Lang J. Appl. Phys. 45 (1974) 3023

- 3.22 O. Engström and A. Alm Sol. St. Elec. 21 (1978)1571
- 3.23 T. Wosiński J. Appl. Phys. 65 (1989) 1566
- 3.24 A. C. Wang and C. T. Sah J. Appl. Phys. 55 (1984) 565
- 3.25 P. Omling, L. Samuelson and H. G. Grimmeiss
J. Appl. Phys. 54 (1983) 5117
- 3.26 T. Figielski Phys. Stat. Sol. (a) 121 (1990) 187
- 3.27 C. Kisielowski and E. R. Weber Phys. Rev. B 44 (1991) 1600
- 3.28 E. V. Astrova and A. A. Lebedev Sov. Phys. Semicond. 19 (1985) 850
- 3.29 A. Marshall and H. G. Maguire
IEEE Trans. Instrument. Meas. 37 (1988) 596
- 3.30 D. C. Houghton, D. D. Perovic, J. -M. Baribeau and G. C. Weatherly
J. Appl. Phys 67 (1990) 1850
- 3.31 F. K. Legoues, J. A. Ott, K. Eberl and S. S. Iyer
Appl. Phys. Lett. 61 (1992) 174
- 3.32 F. M. Ross, R. Hull, D. Bahnck, J. C. Bean, L. J. Peticolas,
R. A. Hamm and H. A. Huggins J. Vac. Sci. Technol. B10 (1992) 2008
- 3.33 D. G. Schimmel J. Electrochem. Soc. 126 (1979) 479
- 3.34 A. R. Powell PhD. Thesis University of Warwick (1992)

CHAPTER 4

CARRIER DISTRIBUTIONS IN Si AND SiGe

4.1 INTRODUCTION

This chapter will focus upon Capacitance-Voltage (C-V) determined apparent free carrier distributions in Si and Si/Si_{1-x}Ge_x/Si layers grown by MBE. The effect of traps in the uniformly doped and heterojunction regions are considered and well defined features attributed to the band offset are observed. Integration of the carrier distributions through the heterojunction region has allowed valence band offset and interface charge density to be determined; the validity of these values is discussed in relation to simulated heterojunction carrier profiles in the presence of traps. Reconstruction of the experimentally determined apparent free carrier distributions using trap distributions determined in Chapter 5 are shown.

4.2 C-V DETERMINED APPARENT FREE CARRIER DISTRIBUTIONS

The ambiguity associated with the C-V determined apparent free carrier distribution in the presence of traps has been widely recognised [4.1-3]; however, it is only recently that, with the advent of C-V simulation models, reconstruction of the experimentally determined profiles has been possible. The increasing interest in band-engineered multilayer structures initiated much of this work and has led to a considerable degree of success in matching simulations to experimentally determined profiles [4.4-6]. However, the complexity of the profiles requires care in interpretation; certain trap distributions can, in particular situations, give rise to features in the apparent free carrier profiles not unlike the accumulation and depletion attributed to a heterojunction band offset [4.3, 4.7, 4.8].

The majority of the work on heterojunction band offsets determined from C-V work has been carried out in the III-V material system. Despite the maturity of this research area, discrepancies and anomalies exist in published results and there would appear to be some question as to the interpretation of results presented in particular cases. Kazmierski *et al.* [4.8] investigated the GaInAs/InP heterointerface; the dramatic changes observed in shape and position of the experimentally observed peak in the carrier profile as temperature was reduced were considered the result of interfacial trap response alone. Of note is the dramatic increase/decrease in extracted interface charge density/conduction band offset around the transition temperature at which the changes occur. Similar observations have been made by other workers but with different physical interpretations. Ogura *et al.* [4.9] found the same trends in extracted interface charge density/conduction band offset Fig 4.1a in InGaAs/InP as a result of changes in the carrier profile with temperature Fig 4.1b; however, in this case, the reduction in device capacitance at the transition temperature is considered in terms of the p^+-n junction depletion capacitance in series with the capacitance associated with the heterojunction. The heterojunction capacitance is thought to vary as a consequence of trap filling at the heterojunction; whilst this explains the effect of reducing the heterojunction capacitance at the ubiquitous transition temperature (in this case $\approx 160K$), it ignores the presence of lower concentrations of the same deep level near the p^+-n junction and their response at the measurement frequency. Interestingly, the transition from the LF to the HF regime occurs at approximately 160K; thus, this deep level will affect the measured capacitance for $T \geq 160K$, as is shown for all reverse biases, and could explain the change in shape and position of the experimentally determined carrier profile. Whilst this does not eliminate the possible effect of a changing heterojunction capacitance, it does illustrate the care needed in interpretation of such measurements in the presence of traps. Work by Forrest *et al.* [4.10] again revealed the dramatic change in extracted parameters around 150K for the $In_{0.53}Ga_{0.47}As/InP$ heterointerface; however, the change in shape and position of the carrier profile as temperature was reduced through this transition at 150K was not observed, despite similar trap

Fig 4.1a Temperature dependence of the extracted interface charge density and conduction band offset for an InGaAs/InP heterostructure (after [4.9]).

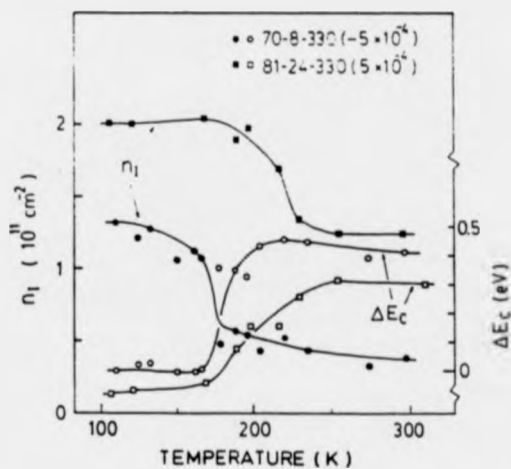
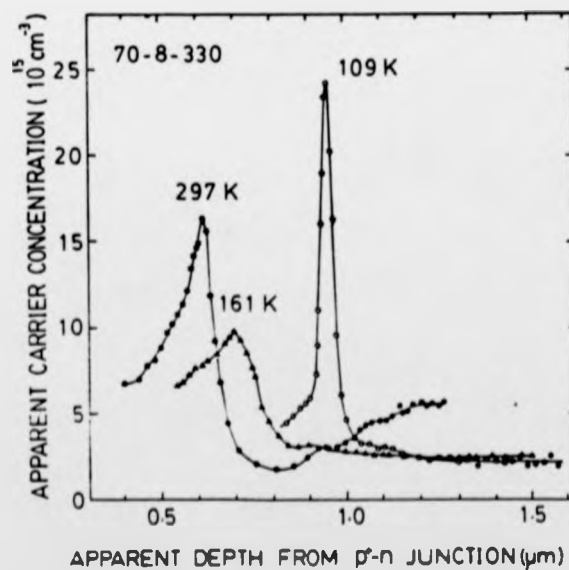


Fig 4.1b Apparent free carrier distributions from which values extracted in Fig 4.1a were obtained.



distributions to Ogura *et al.* The shift to lower temperature of this transition for a lower measurement frequency suggested some change in trap response, although this was not discussed; the physical significance of the reduction in conduction band offset was considered to be due to trap filling at low temperature, distorting the band structure and removing the effective band offset.

Work by t'Hooft *et al.* [4.11] considered the influence of dopant depth in the heterojunction region - reduced dopant ionisation as a consequence of the band bending would result in smaller degrees of accumulation and depletion in the vicinity of the heterojunction, resulting in the band offset being underestimated. Similar effects would occur for compensation of the shallow dopants since fewer free charge carriers are available in the heterojunction region.

Leu *et al.* [4.12] set out to investigate the possible distortion to heterojunction free carrier profiles in the presence of traps via simulations; this very thorough work provides amended equations from the analysis of Kroemer *et al.* [4.13] for the determination of trap density and conduction band offset in the presence of deep and shallow traps. The variation of the conduction band offset and interface charge density as a function of temperature/measurement frequency are discussed; it is proposed that the most accurate values of the conduction band offset are obtained within the low frequency or high temperature measurement regime. Part of the work presented later uses the simulation program [4.7] to determine the validity and applicability of their results in the Si and Si/Si_{1-x}Ge_x/Si material system investigated here. Further work by Leu *et al.* [4.14] considered the correction necessary to determine the conduction band offset for asymmetric trap distributions at the heterojunction with different doping levels either side of, and error in the actual position of, the heterojunction.

The relation between interface charge and bulk trap distributions, according to source purity and lattice mismatch, have also been investigated; once again, one must be aware that the distortion occurring to the free carrier distributions will ultimately affect the validity of the extracted interface charge density. Lee *et al.* [4.15] report low interface charge densities for the In_{0.53}Ga_{0.47}As/InP heterointerface, independent of

measurement temperature and lattice mismatch. Carrier profiles show clear accumulation and depletion features over the entire measurement range of temperatures, in contrast to previous results [4.10]. No electrical activity is considered associated with the lattice mismatch whilst it is clear that the use of high purity In source material reduced the interfacial charge. Similarly, work by Whitney *et al.* [4.16] showed no relation between lattice misfit and interfacial charge for the $\text{In}_{0.53}\text{Ga}_{0.47}\text{As}/\text{InP}$ heterointerface - however, changes in shape and position of the carrier profile were observed as a function of temperature. Deep level distributions showed a peak towards the interface, suggesting a strong correlation to the interface charge. This was also suggested by Okumura *et al.* [4.17]; however, unless the exact nature of traps ie. donor or acceptor-like is determined, this apparent relation between interface charge and trap distribution is meaningless. Fixed charge is bias and temperature independent and will not be detected by spectroscopic techniques like DLTS; only interfacial traps with a variable occupancy will be detected by both DLTS and as an extracted interfacial charge via numerical integration of the carrier profile. Note that the extracted interface charge density will vary as a consequence of this, depending on the possible distortions that will occur to the heterojunction accumulation and depletion features in the presence of variable occupancy traps. In contrast, Morii *et al.* [4.4] found the interface charge density increased with increasing Al content for the $\text{Al}_x\text{Ga}_{1-x}\text{P}/\text{GaP}$ heterointerface and attributed it to the greater degree of lattice mismatch between the alloy layers. Similar conclusions were made by Ogura *et al.* [4.9] with both deep level and interface charge density increasing for increasing mismatch between InGaAs and InP .

Finally, only a few brief reports have been made regarding the use of the C-V technique to determine band offsets and interface charge densities in the $\text{Si}/\text{Si}_{1-x}\text{Ge}_x/\text{Si}$ system. Denhoff *et al.* [4.18] found only approximate agreement between theoretically predicted and experimentally determined conduction band-offsets, with considerable error coming from the non-uniform bulk doping levels either side of the heterojunction. Tatsumi *et al.* [4.19] reported a valence band offset of 0.18eV for $x=0.3$ and interface charge densities up to $3 \times 10^{11} \text{ cm}^{-2}$ for $x=0.4$ Ge composition layers, directly relating

the latter electrical activity to interfacial misfit dislocations; no apparent free carrier profiles were presented, so the accuracy of these results is unknown.

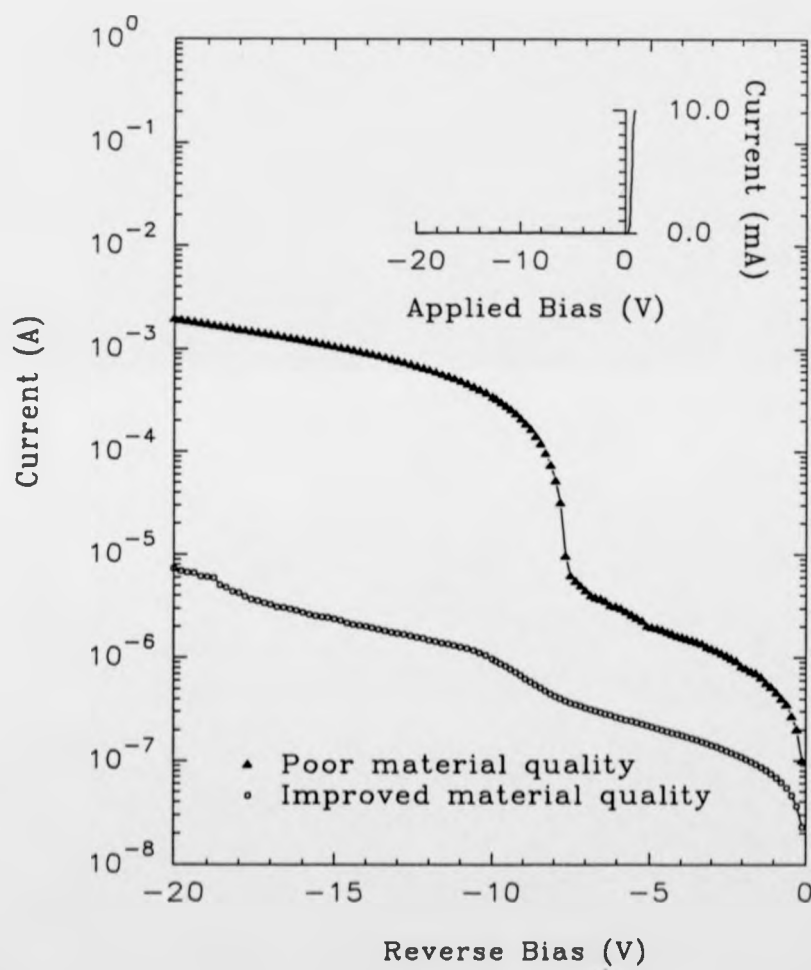
The ease and simplicity of heterojunction band offset and interface charge density extraction from the apparent free carrier distributions make C-V profiling a very powerful characterisation technique. However, care is needed in the interpretation of the results if traps are present; simulation programs can provide an assessment of the technique and validity of the experimentally determined parameters in such circumstances.

4.3 AN ASIDE: THE SCHOTTKY BARRIER

All depletion capacitance measurements relied on the formation of high quality Schottky barriers. It was necessary for such devices to be capable of supporting large reverse bias (in order to access the buried $\text{Si}_{1-x}\text{Ge}_x$ layer), with a minimal reverse leakage current and small series resistance. I-V measurements were initially used to assess these parameters; departures from these requirements usually reflected poor rectifying junctions, which were inadequate for capacitance measurements.

A considerable amount of work was initially spent investigating metal-Si Schottky barriers; sputtered Ti contacts (as detailed in section 3.2.5) were found to provide the best rectifying barriers, both in terms of their reproducibility and stability. However, greater problems associated with the fundamental quality of the MBE material were encountered. Fig 4.2 compares typical reverse bias characteristics for early $\text{Si}/\text{Si}_{1-x}\text{Ge}_x/\text{Si}$ samples as compared to later, improved samples. For the early samples, leakage is observed to be $\leq 10\mu\text{A}$ up to approximately -8V beyond which a sudden increase by an order of magnitude is seen; this transition bias corresponds to the point at which the depletion edge moves into the $\text{Si}_{1-x}\text{Ge}_x$ layer. Increasing reverse leakage currents have been attributed to increasing misfit dislocation densities [4.19, 4.20]; however, the observations made here indicated the leakage currents to be independent of misfit densities. Similar observations have been attributed to metal precipitation [4.21]

Fig 4.2 Non-ideal and improved Schottky characteristics for $\text{Si}/\text{Si}_{1-x}\text{Ge}_x/\text{Si}$ heterostructures.

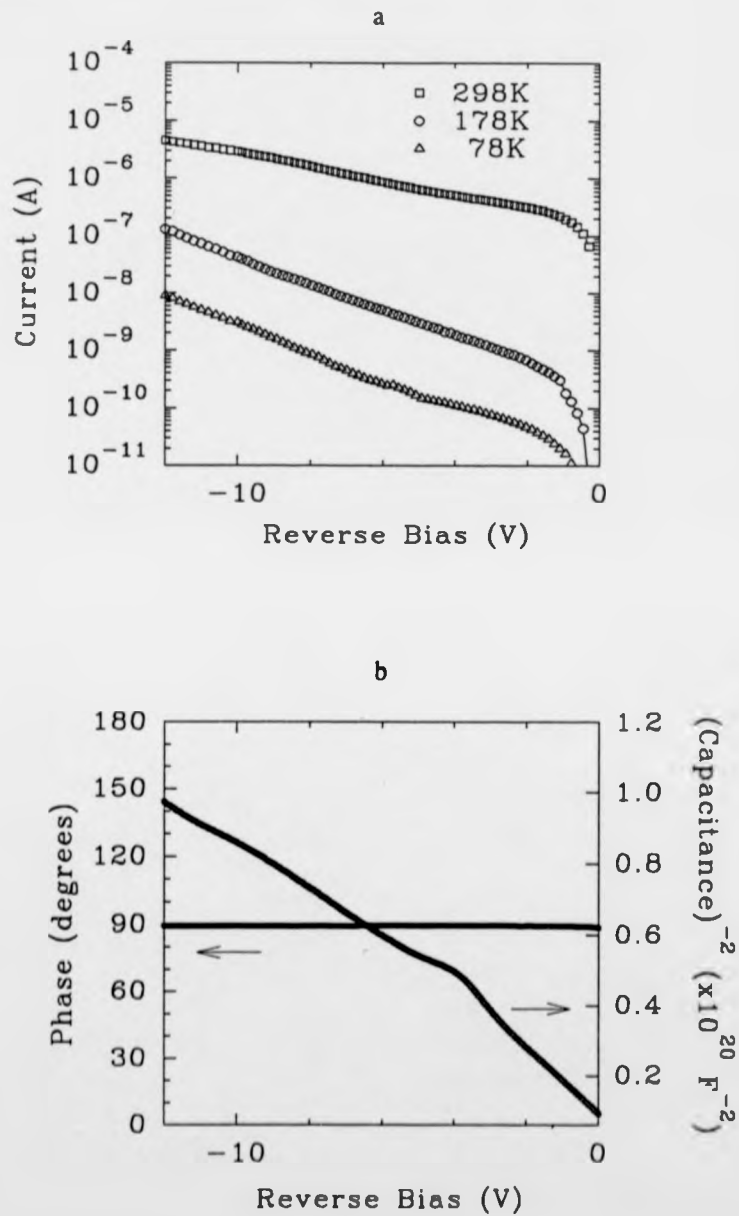


and can lead to dominant tunneling currents under both forward and reverse bias. Such current components are identified by their temperature independent behaviour, as was seen particularly for the leakage currents at biases $\leq -8\text{V}$. The argument for metallic contamination was verified by Secondary Ion Mass spectrometry (SIMS) on 2D hole gas (2DHG) structures from the same growth series [4.22]: Cu levels exceeding the solid solubility level were found to be located preferentially within the alloy $\text{Si}_{0.8}\text{Ge}_{0.2}$ layer. The onset of this increased leakage associated with the $\text{Si}/\text{Si}_{1-x}\text{Ge}_x$ interface made capacitance measurements into the alloy layer impossible.

The most likely source for the contamination was from the Cu hearth of the electron-beam evaporator; during deposition, the entire surface of the Ge charge melts. Significant in-diffusion of Cu would be expected since this molten surface is in direct contact with the Cu hearth in which the charge sits. This prompted the use of liners around the Ge charge: initially, a Si liner was employed (24 growth series samples), which was later superseded by a graphite liner (28 growth series). The interposition of such liners prevents contact between the molten Ge and the Cu hearth since both the Si and graphite remain solid at the Ge evaporation temperature. Whilst the use of such liners will have a limited life due to eventual in-diffusion of metals, the improvements to the material quality were substantial - seen in the improved 2DHG mobilities and in the I-V characteristics, particularly the reverse leakage current Fig 4.2. The inset of Fig 4.2 shows a typical Schottky diode characteristic, illustrating the ideal rectifying behaviour with a low reverse leakage current and small series resistance; no discernible differences were observed in the I-V characteristics, comparing the 24 and 28 growth series samples. Temperature variation in the ideality factor, n , from ≈ 1 at 300K to ≥ 2 at reduced temperatures, indicated recombination current components to be the most likely cause of departure from ideal thermionic behaviour (the influence of image force lowering or interfacial layers are considered temperature independent [4.23]). Typical reverse bias characteristics for a $\text{Si}/\text{Si}_{1-x}\text{Ge}_x/\text{Si}$ sample are shown in Fig 4.3a whilst the C^{-2} and phase angle versus V for the same sample are shown in Fig 4.3b. The reverse leakage may be described approximately by a $V^{1/2}$ dependence for low reverse bias

Fig 4.3

Schottky diode characteristics for a typical $\text{Si}/\text{Si}_{1-x}\text{Ge}_x/\text{Si}$ heterostructure illustrating: a) leakage current and b) variation of the depletion capacitance with reverse bias.



(eliminating effects due to image force lowering, where $I \propto V^{1/4}$ [4.24] and interfacial layers, where $I \propto V$ [4.25]); however, the increase in reverse leakage for $V \leq -5V$ cannot be matched by this simple dependence. From (3.11), the generation current component defined in (3.9) will depend upon both $V^{1/2}$ and the trap concentration; since, from Chapter 5, it is generally observed that trap concentrations increase on profiling from the Si into the $Si_{1-x}Ge_x$ layer, this may well account for the increase in reverse leakage. From the C^{-2} - V characteristic, the kink at $-5V$ corresponds to the depletion edge at the heterointerface and is well matched to the transition in reverse leakage current.

Assuming ϕ_b is bias-independent, (3.19) may be written as:

$$C^{-2} = \left(\frac{2}{qA^2 N_A \epsilon_0 \epsilon_r} \right) \left(V_R + \phi_b - \xi - \frac{kT}{q} \right) \quad (4.1)$$

where $\xi = E_F - E_V / kT$. For a C^{-2} - V plot, the intercept V_I on the x-axis is given by:

$$V_I = \phi_b - \xi - \frac{kT}{q} \quad (4.2)$$

Thus the Schottky barrier height, ϕ_b may be readily determined. Extracted barrier heights for Ti on Si (note that the contacts were always made to Si on either uniform Si or $Si/Si_{1-x}Ge_x/Si$ samples) were $0.8 \pm 0.2 eV$; this compares well to previously reported values [4.26, 4.27]. The reproducibility and stability of such contacts may reflect the formation of silicide-Si barriers [4.28], which are considered to be atomically abrupt and free of interfacial layers.

The Schottky contacts used to achieve capacitance measurements have thus been shown to be near ideal; it is assumed that interfacial layers play a minimal role. Furthermore, the low series resistance means that both $R_s/R_p < 1$ and $\omega R_s C < 1$ (from section 3.2.3.2) and hence, this too will have a minimal effect. The validity of the apparent free carrier profiles was determined from the phase angle; at high reverse bias $\leq -18V$ (not shown in Fig 4.3), the increasing leakage resulted in a drop in the phase

angle. One should be aware that this will correspond to an anomalous increase in the free carrier concentration [4.29] and the profile is subject to error in these regions.

4.4 EXPERIMENTAL RESULTS

In order to investigate the various trap response regimes, C-V measurements were made at a fixed oscillator frequency of 1Mhz, scanning typically between 0 and -20V reverse bias for a variety of temperatures.

Because of the unknown position of the Si/Si_{1-x}Ge_x heterointerface, it was necessary to assume a uniform dielectric constant throughout the Si/Si_{1-x}Ge_x/Si layers. This was taken as the arithmetic mean of the dielectric constant for Si (11.7) and Si_{1-x}Ge_x, the latter value being calculated as a linear interpolation between the values for Si and Ge (16.3). However, Babic *et al.* [4.30] showed that variation of the dielectric constant across an isotype heterointerface had no effect on the determination of the band offset or interface charge density from the carrier profile, justifying the uniform dielectric constant assumed throughout the layer. Note the average value is used throughout the heterostructure for the purpose of matching simulation to experimental data.

For the extraction of valence band offset and interface charge density a program was written to carry out a numerical integration of the experimental data based on (3.38) and (3.40) (see Appendix A). Using a histogram approach ($p^*(x^*) - N_A^*(x^*)$) and $(p^*(x^*) - N_A^*(x^*))(x^* - x_I)$ are evaluated for each x^* ; $N_A^*(x^*)$ is an input parameter and is determined from the bulk uniform carrier levels either side of the heterojunction. x_I is evaluated by matching simulation to experimental data; a guess is made as to the value of x_I and this is used as input to the integration program to determine the valence band offset. These values are then used as input to the simulation program to produce a carrier profile which is compared to the experimentally determined carrier profile. This iterative process is further complicated by the introduction of interfacial charge, which is discussed in section 4.5. For the purposes of determining x_I , interfacial charge is ignored.

(3.38) gives a value for $\Delta\phi$ and requires (3.45) to determine the valence band offset. Using non-degenerate statistics:

$$\delta_2 - \delta_1 = \frac{kT}{q} \ln \left[\frac{N_{A1}^*(x^*) N_{V2}}{N_{A2}^*(x^*) N_{V1}} \right] \quad (4.3)$$

where the valence band densities of states N_{V1} and N_{V2} are for the Si and $\text{Si}_{1-x}\text{Ge}_x$ regions respectively - note that a linear variation is assumed between Si ($1.049 \times 10^{19} \text{ cm}^{-3}$) and Ge ($4.327 \times 10^{18} \text{ cm}^{-3}$) in order to determine the density of states according to the Ge composition of the alloy.

I. Si

Apparent free carrier distributions for samples #24/21 ($T_s = 530^\circ\text{C}$, $N_A \approx 10^{16} \text{ cm}^{-3}$) and #28/20 ($T_s = 530^\circ\text{C}$, $N_A \approx 10^{16} \text{ cm}^{-3}$) versus temperature are shown in Fig 4.4 and Fig 4.5 respectively. Sample #24/21 shows relatively uniform doping levels at high temperature; however, as temperature is reduced enhanced features are observed and the carrier profile takes on an undulating appearance. Contrast this with sample #28/20, which maintains its uniformity down to the lowest measurement temperatures, with only one feature becoming apparent close to the epilayer/substrate interface. The validity of the profiles is verified from the apparent free carrier concentration and higher doping feature of the p^+ substrate, matching well with the growth specifications regarding epilayer thickness and intended doping level.

II. $\text{Si}/\text{Si}_{1-x}\text{Ge}_x/\text{Si}$

Typical temperature trends for the $\text{Si}/\text{Si}_{1-x}\text{Ge}_x/\text{Si}$ apparent free carrier distributions are shown in Fig 4.6a for sample #28/17 ($T_s = 530^\circ\text{C}$, $N_A \approx 10^{16} \text{ cm}^{-3}$, $x = 0.12$). The well defined depletion and accumulation feature at approximately $0.8 \mu\text{m}$ is associated with the first heterojunction; note the sharper definition of this feature as temperature is reduced. This is illustrated more clearly in Fig 4.6b; note the fixed position of the first heterojunction whilst the second heterojunction shows a reduced accumulation and depletion feature and is observed to shift to greater depth as

Fig 4.4

Apparent free carrier distributions for sample #24/21 as a function of temperature.

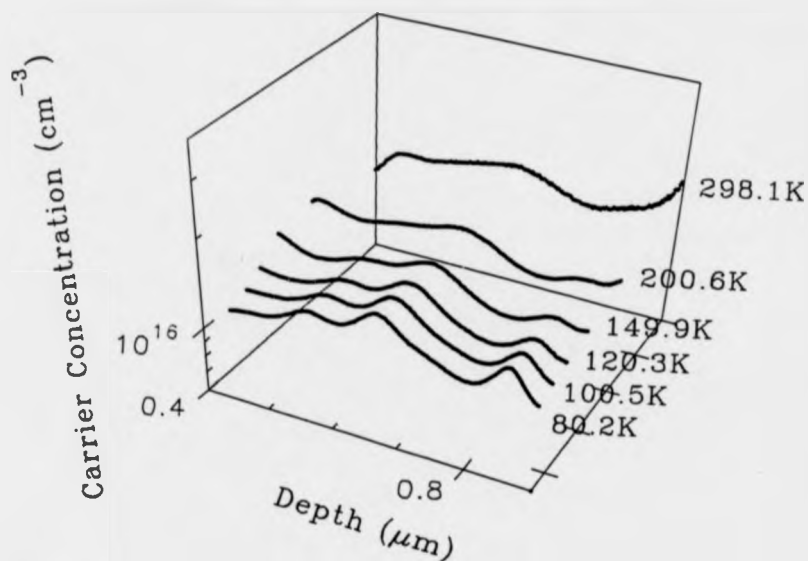


Fig 4.5

Apparent free carrier distributions for sample #28/20 as a function of temperature.

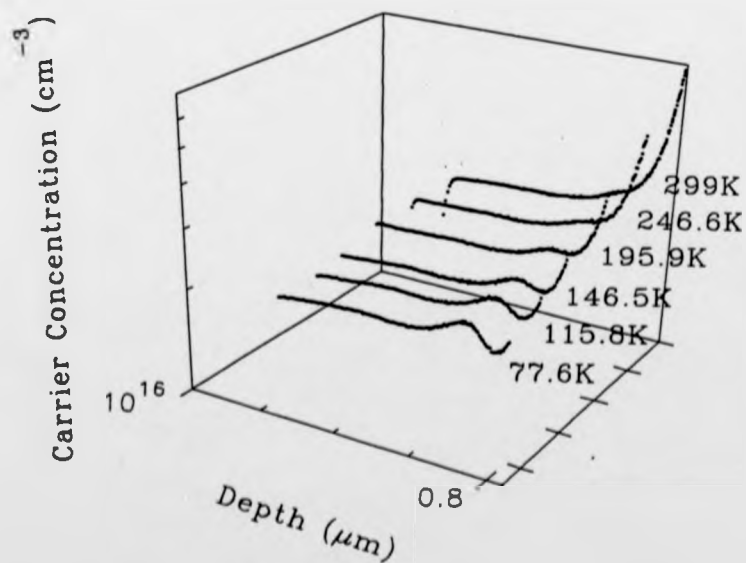


Fig 4.6a

Apparent free carrier distributions for sample #28/17 as a function of temperature.

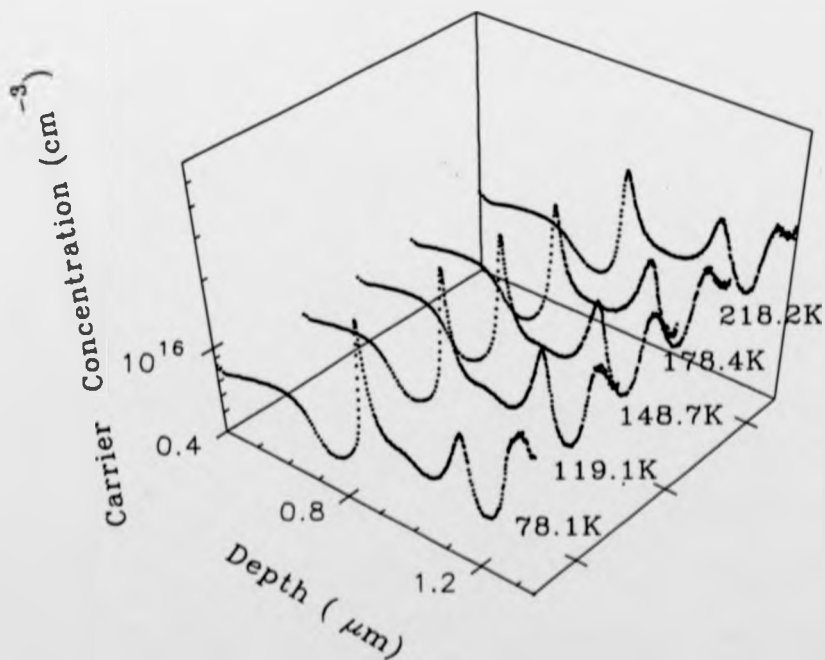
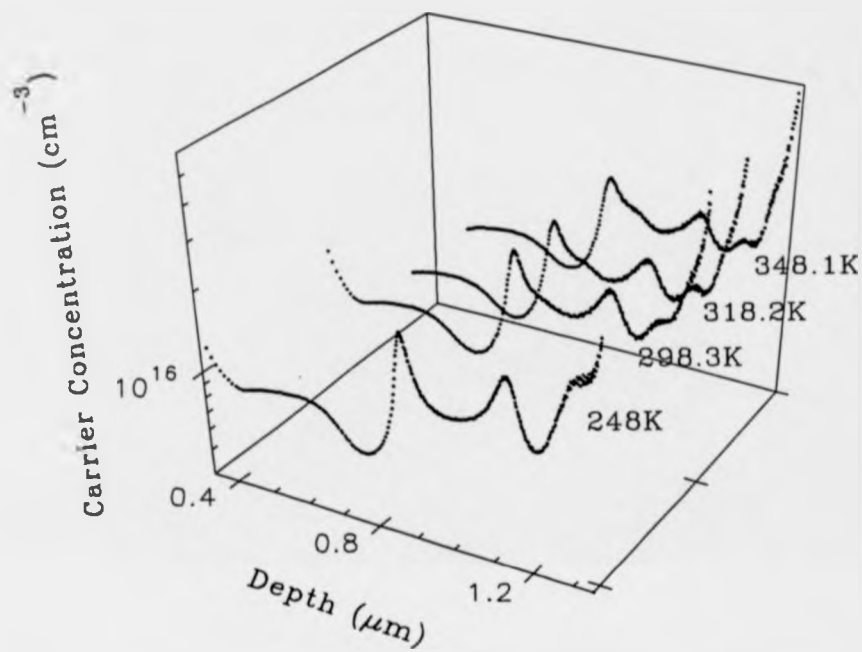
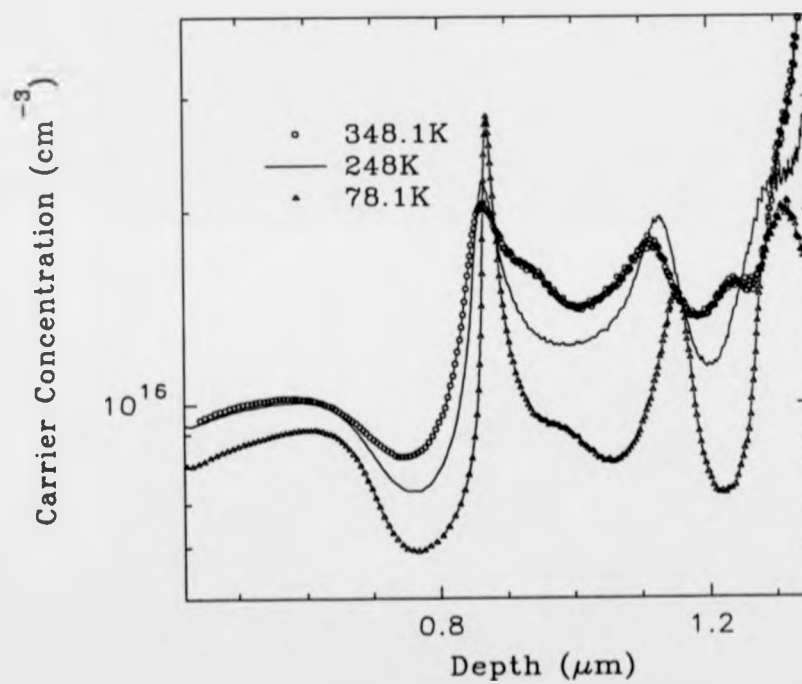


Fig 4.6b Apparent free carrier distributions for sample #28/17 as a function of temperature.



temperature is reduced. The reduction in apparent free carrier concentration at low temperature is most pronounced in the $\text{Si}_{0.88}\text{Ge}_{0.12}$ region and occurs to a lesser degree in the Si capping layer. These observations were made in all metastable samples investigated in this study. Note the progression of the apparent free carrier distribution for sample #24/27 ($T_s=530^\circ\text{C}$, $N_A \approx 10^{16} \text{ cm}^{-3}$, $x=0.08$) at reduced temperatures Fig 4.7 - the observed undulating appearance in the bulk regions is similar to the trends observed in results section I. between the 24 and 28 series uniform Si samples.

Extracted valence band offsets and interface charge densities are shown in Fig 4.8a&b respectively as a function of temperature for a variety of Ge percentages. The greater distortion observed in the carrier profiles for the 3% and 8% Ge composition layers made choice of uniform bulk doping levels difficult and is reflected in the larger variation of extracted band offset. Despite this, all samples showed good agreement to the predicted valence band offset [4.31] within the experimental error. Inferred interface charge densities showed less variation with temperature below 250K and, with the exception of the 3% Ge alloy, all indicated acceptor-like charge; if the 12% alloy is disregarded, the overall trend is for an increasing interfacial charge density with increasing Ge content.

Sample #28/16 ($T_s=530^\circ\text{C}$, $N_A \approx 10^{16} \text{ cm}^{-3}$, $x=0.2$) Fig 4.9 shows a very well defined depletion feature at the first heterojunction; since this alloy layer is only $0.1\mu\text{m}$ in thickness, the accumulation features of the first and second heterojunction merge due to the limited resolution of the profiling technique and, as a result, it was not possible to extract the heterojunction parameters. Note the dramatic shift in position and shape of the features for $T < 130\text{K}$.

The previous layers discussed here are considered to be in a metastable strained state (see section 5.4 for details). Sample #24/19 ($T_s=600^\circ\text{C}$, $N_A \approx 10^{16} \text{ cm}^{-3}$, $x=0.1$) was in a fully relaxed state - apparent free carrier distributions as a function of temperature are shown in Fig 4.10. Significant differences are seen to exist between these carrier profiles as compared to those for the metastable strained structures: whilst depletion and accumulation is seen at the first and, to a lesser extent, the second

Fig 4.7

Apparent free carrier distributions for sample #24/27 as a function of temperature.

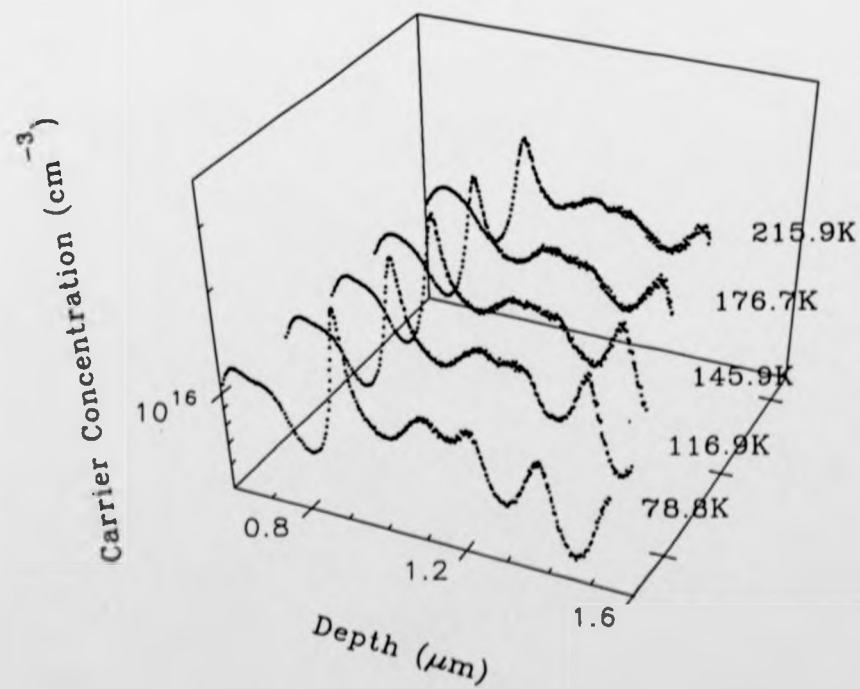
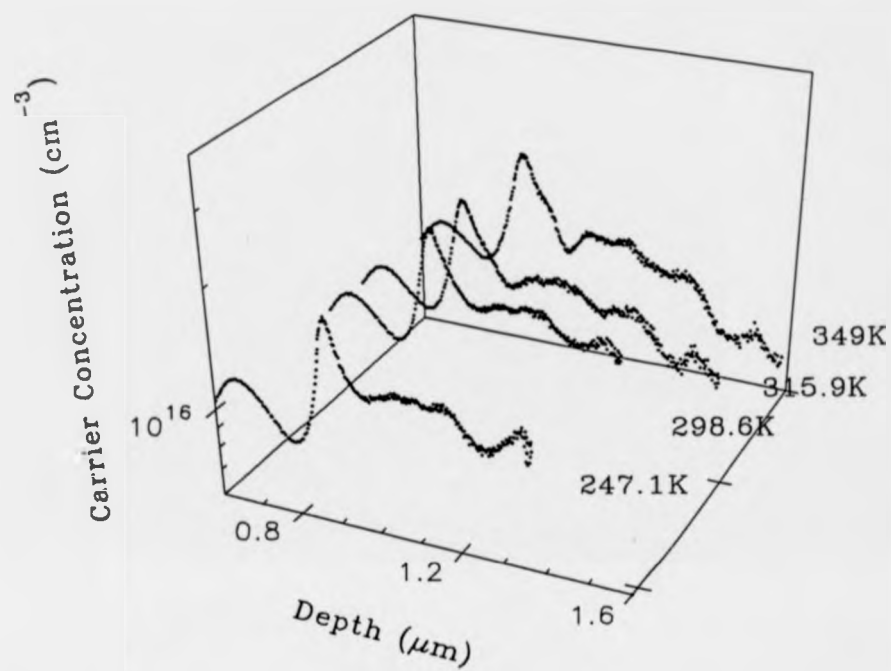


Fig 4.8a Temperature dependence of the extracted valence band offsets for various Ge compositions.

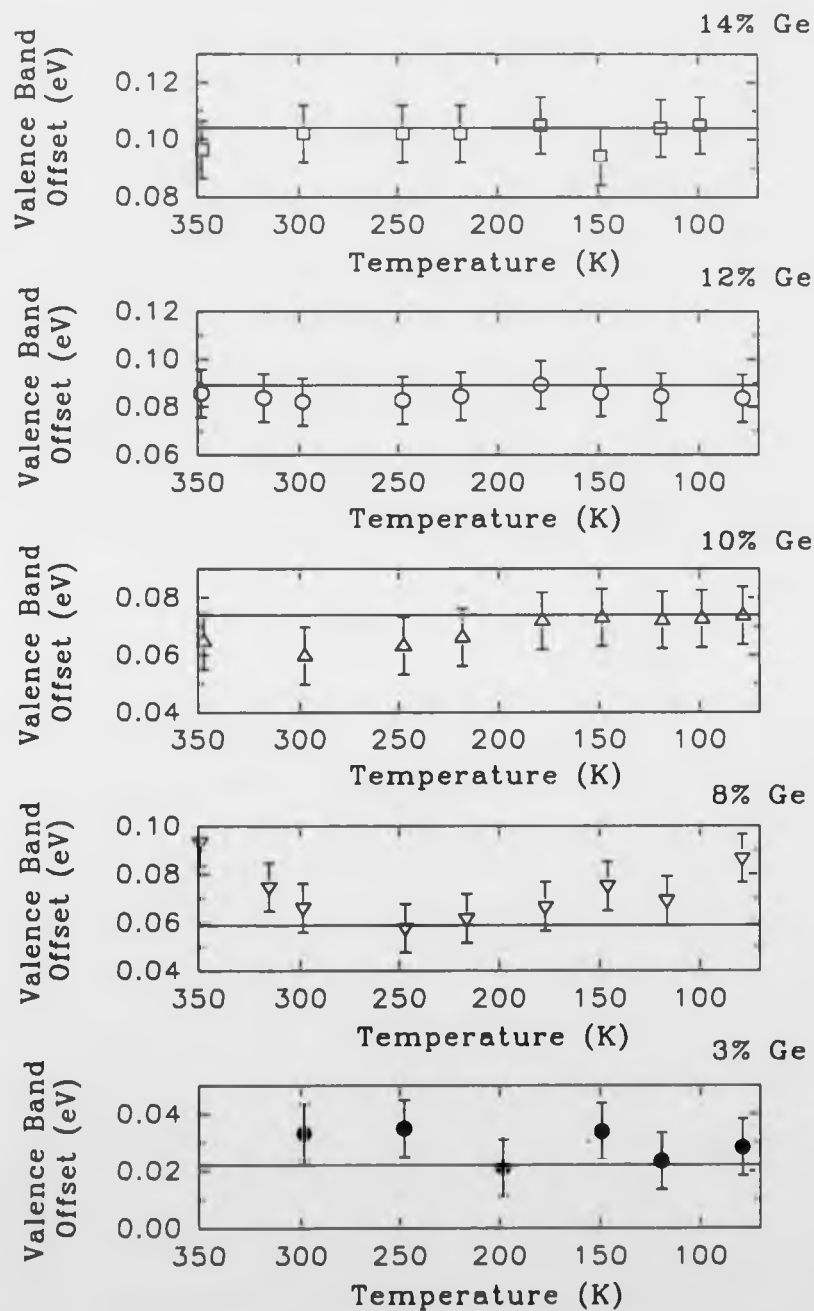


Fig 4.8b Temperature dependence of the extracted interface charge density for various Ge compositions.

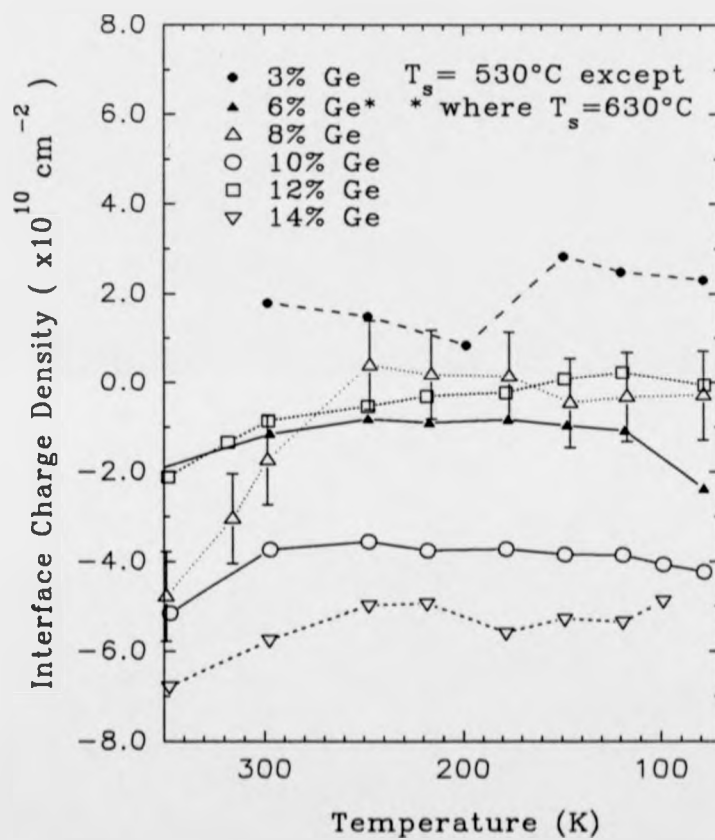


Fig 4.9

Apparent free carrier distributions for sample #28/16 as a function of temperature.

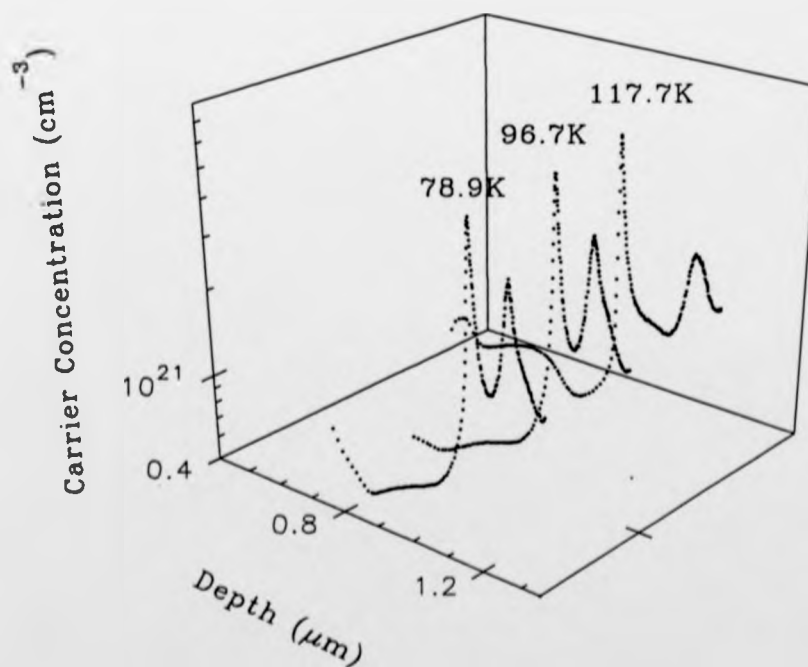
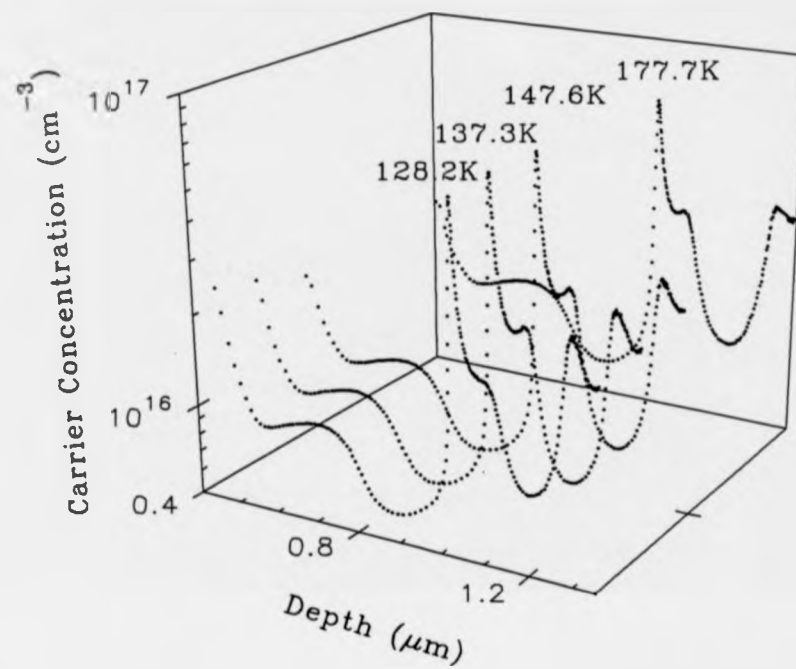
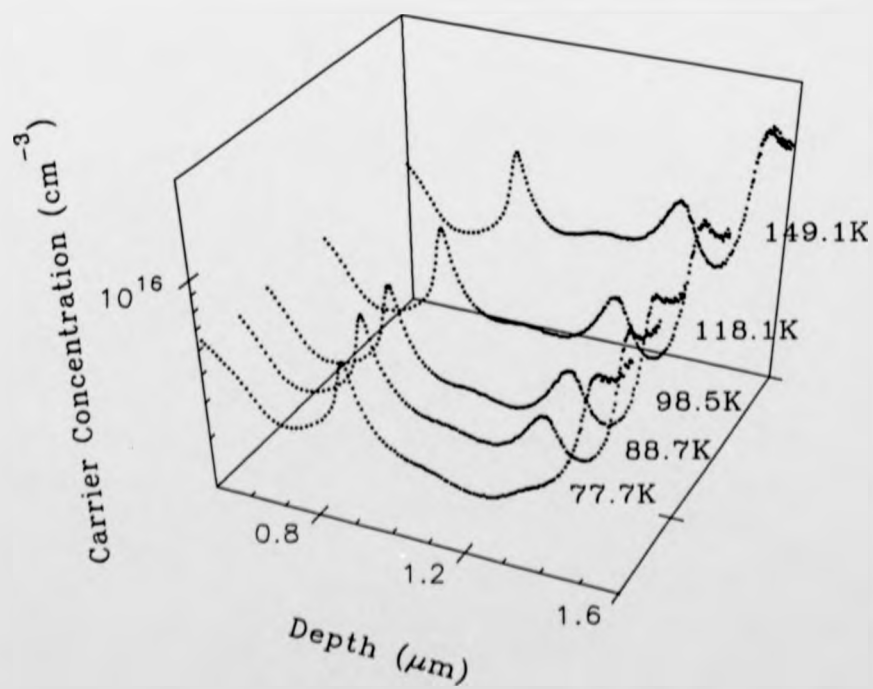
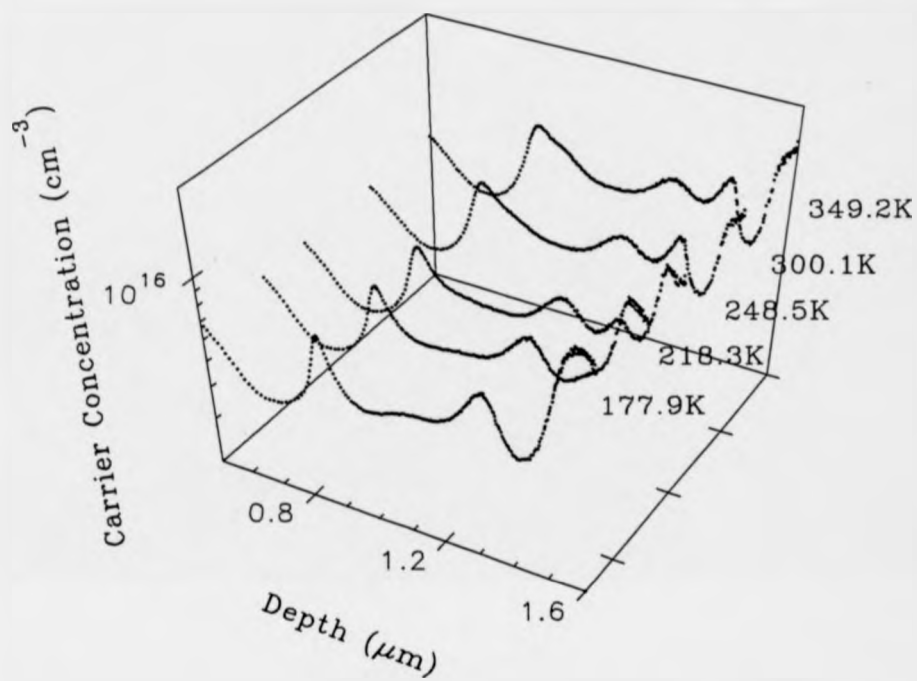


Fig 4.10

Apparent free carrier distributions for sample #24/19 as a function of temperature.



heterojunction, the apparent free carrier concentration is reduced well below the intended doping levels and further reductions are observed at lower temperatures. The degree to which this occurs is much greater than either the uniform Si or the metastable strained Si/Si_{1-x}Ge_x/Si layers.

4.5 DISCUSSION

The uniform Si layers will be considered first as the benchmark to which the Si/Si_{1-x}Ge_x/Si layers will be compared.

The undulating profile observed for sample #24/21 at reduced temperatures was in direct contrast to the uniformity exhibited by sample #28/20 under similar measurement conditions. This was initially considered to reflect different trap distributions/type, probably as a consequence of the modifications made to the growth system to reduce metallic contamination. Comparison of the DLTS results (section 5.3) indicated similar trapping levels; however, trap distributions showed significant differences.

Sample #24/21 showed a high ($\approx 10^{15} \text{ cm}^{-3}$) trap concentration toward the epilayer surface, with a lower ($\approx 2 \times 10^{14} \text{ cm}^{-3}$) uniform trap concentration deeper into the epilayer. A high concentration of donor traps towards the surface could produce the large observed zero bias depletion through compensation of the shallow acceptors and would be observed at some deeper spatial position as the traps empty, possibly corresponding to the raised part of the profile. From a consideration of the emission rates, it is believed that these surface traps undergo the transition from LF to HF regime as temperature is reduced from 300K to 200K; whilst a shift in the profile is observed, no significant change is seen in the carrier profile which would be expected for trap response changing from the LF to the HF response regime. Between 0.5-1 μm , uniform trap distributions with level A(0.184eV) dominant were present; however, such low concentrations ($\approx 2 \times 10^{14} \text{ cm}^{-3}$) may have an insignificant effect on the carrier profile. Note the LF to HF transition for this level occurs between 200K and 150K. In order to investigate these effects, simulations were carried out assuming uniform doping at

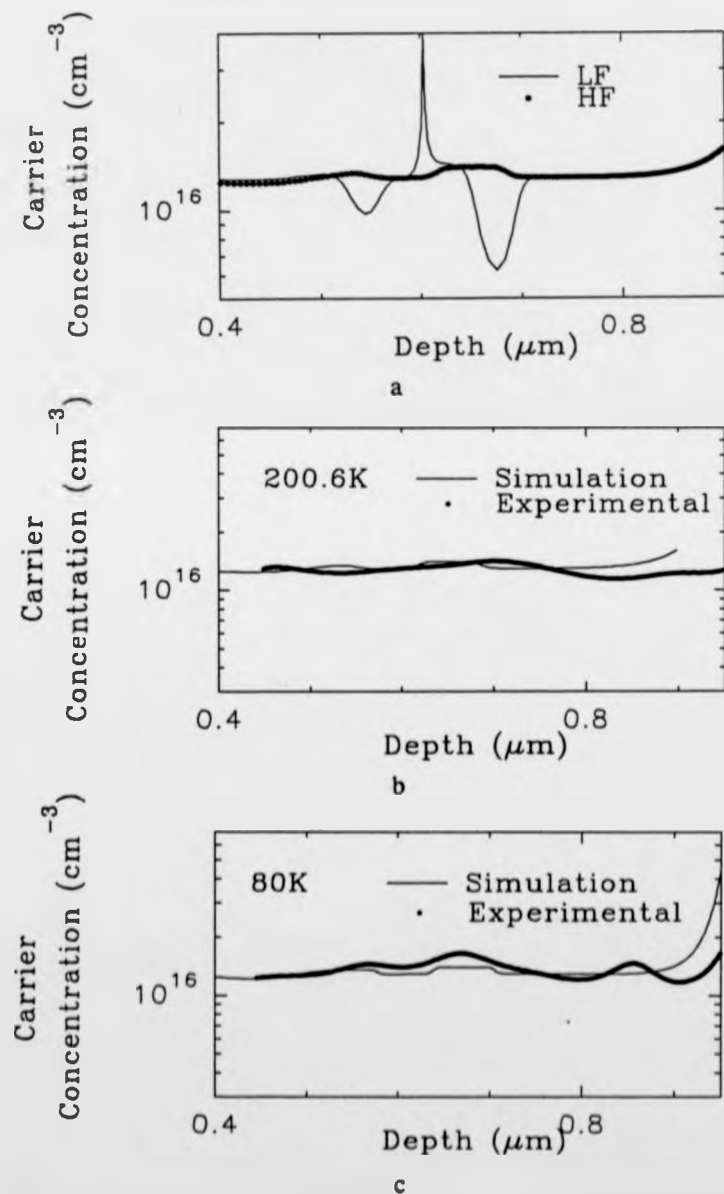
$1.3 \times 10^{16} \text{ cm}^{-3}$ and corrected trap concentrations from Fig 5.3, according to section 5.5. Note the trap distribution is defined in a block histogram form and only one trap level and concentration may be entered into the model for a particular spatial position. Donor traps are assumed here, based on the discussions of the DLTS results in section 5.6. Trap type is not clear (from the apparent free carrier distribution) since the background level, according to the shallow acceptor doping alone, is not well defined. Fig 4.11a indicates both the LF and HF simulated apparent free carrier distributions in the presence of deep traps - of note are the two features which modulate the profile in the HF measurement regime. The LF profile is also shown to indicate the distortion to the profile should the traps be able to respond at the measurement signal frequency; the features observed are due to the higher concentration surface traps and no effect is observed for the uniform trap distribution. Fig 4.11b&c compare simulation to experimental data at 200.6K and 80K respectively. Only HF response is considered since the surface traps will be unable to follow the measurement signal frequency at these reduced temperatures. An approximate match is seen at 200.6K whilst better agreement is seen at 80K; however, the feature observed close to the substrate is not accounted for, according to the measured uniform deep level distribution. Furthermore, these surface traps will have moved into the VHF regime down at 80K and would not be able to respond; the model does not take this into account but would result in dips in the carrier profile at the trap location and the features attributed to trap emptying would not be observed.

Contrast this with sample #28/20, which indicated a high, localised trap distribution with a decrease in concentration moving deeper into the epilayer ($\approx 2 \times 10^{15} \text{ cm}^{-3} \rightarrow 10^{13} \text{ cm}^{-3}$). A high surface concentration of donor traps could, once again, cause the significant observed zero bias depletion depth but the subsequent trap emptying is not seen; indeed, the uniform reduction of the carrier profile by approximately 10^{15} cm^{-3} at low temperatures suggested some discrepancy in the deep level distributions as determined by DLTS Fig 5.4 - note this reduction occurs at the HF to VHF transition for the dominant level D(0.461eV). Careful analysis of the

Fig 4.11

Simulated and experimental apparent free carrier distributions assuming $1.3 \times 10^{16} \text{ cm}^{-3}$ uniform doping and corrected trap distributions according to Fig 5.3 for sample #24/21:

- a) comparison between LF and HF simulated distributions,
b) matched data at 200.6K and c) 80K.

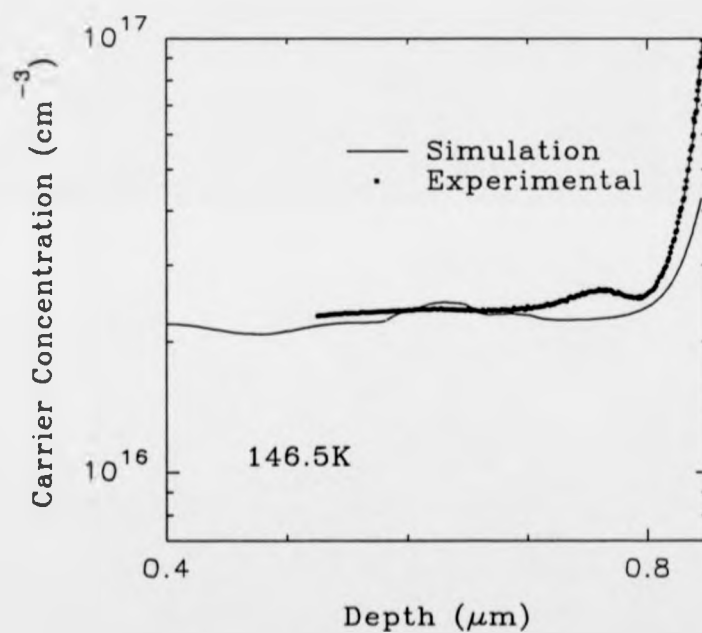


broadening effects (section 5.5) gave some correction to yield a less spatially localised trap distribution and these were used as input to the simulation model, assuming uniform doping at $2.2 \times 10^{16} \text{ cm}^{-3}$ and traps to be donor-like in nature. Results are shown in Fig 4.12 for the simulated HF apparent free carrier distribution compared to experimental data at 146.5K. Only reasonable correlation is observed; the peak attributed to trap emptying is not seen in the experimental data and as for sample #24/21, the feature close to the substrate cannot be accounted for according to the deep level distributions. The correction made to the deep level distribution did not particularly improve the match; however, it should be noted that the dominant level D was only measured up to $0.55 \mu\text{m}$ in depth and its existence at greater depths could explain the discrepancy.

These results illustrate the ambiguity associated with profile reconstruction in the presence of traps: the enhancement of features at reduced temperatures may be a consequence of the reduction in Debye length increasing the resolution of the technique; discrete energies as a result of the broadening effects observed in DLTS (see section 5.5) are undefined, leading to errors in trap emission rates, exact spatial position and concentration; doping modulation (particularly for sample #24/21) may also contribute to the features observed. Additionally, the model only allows LF (all traps respond) or HF (no traps respond) defined situations to be simulated - in reality, individual traps will respond according to the temperature of measurement and hence a situation can arise with different traps operating in the LF, HF and VHF regimes simultaneously. Thus, despite detailed considerations of trap distributions from Chapter 5, the origin of the differences observed between the uniform Si samples from the 24 and 28 growth series remains unclear and requires further work to elucidate the source.

Additional problems were anticipated on the introduction of the heterojunction as to the validity of the extracted valence band offset and interface charge density, in view of the distortions to the free carrier distribution in the presence of traps. In order to assess the possible errors that could occur, the simulation program was used to

Fig 4.12 HF match between simulated and experimental apparent free carrier distributions assuming $2.2 \times 10^{16} \text{ cm}^{-3}$ uniform doping with corrected trap distributions according to Fig 5.4 for sample #28/20 at 146.5K.



investigate the variation of the extracted parameters for shallow and deep traps at or in the vicinity of the heterointerface.

In each case, profiling occurred from wide band-gap Si to narrow band-gap SiGe with a band offset of 0.08eV. All trap distributions were positioned at $x_I = 0.8\mu\text{m}$ and the numerical integration procedure, as detailed in the previous section, was used to extract band offsets and interface charge densities (note (3.38) was used to determine the built-in potential since no correction term according to (3.41) was required in this initial case).

Fixed Charge Traps

If the donor trap is well above the Fermi level, even at large reverse bias or high temperature, or the acceptor trap is well below the Fermi level, even at zero applied reverse bias or low temperature, then the charge state of these traps is bias independent and they may be referred to as "Fixed charge traps". Simulated carrier profiles are shown in Fig 4.13a; note that since the charge state of such traps is bias independent, the apparent free carrier profile is not influenced by trap response at the measurement signal frequency. The features may be considered qualitatively thus: whilst distortion to the depletion and accumulation features is minimal at 10^{10} cm^{-2} , large distortion occurs for trap densities at 10^{11} cm^{-2} . For acceptor traps in p-type material, the significant local band bending produces a well in which accumulation of carriers will occur, observed as the large peak in the apparent free carrier distribution. Likewise, donor traps in p-type material will produce band bending in the opposite sense, giving a depletion effect observed as the dip in the apparent free carrier distribution. Extracted band offsets and interface charge densities are given in Table 4.1. Despite the distortion, band offset values of 0.079eV and 0.074eV for $-2 \times 10^{11}\text{ cm}^{-2}$ (acceptor) and $1.98 \times 10^{11}\text{ cm}^{-2}$ (donor) apparent interfacial charge densities respectively are obtained, in good agreement with the input parameters. For trap densities 10^{10} cm^{-2} band offset values of 0.078eV were obtained for both $-2.12 \times 10^{10}\text{ cm}^{-2}$ (acceptor) and

Fig 4.13

Simulated apparent free carrier distributions for: a) fixed charge, b) deep donor and c) deep acceptor traps positioned at the heterointerface, $x_I = 0.8 \mu\text{m}$ with band offset of 0.08 eV .

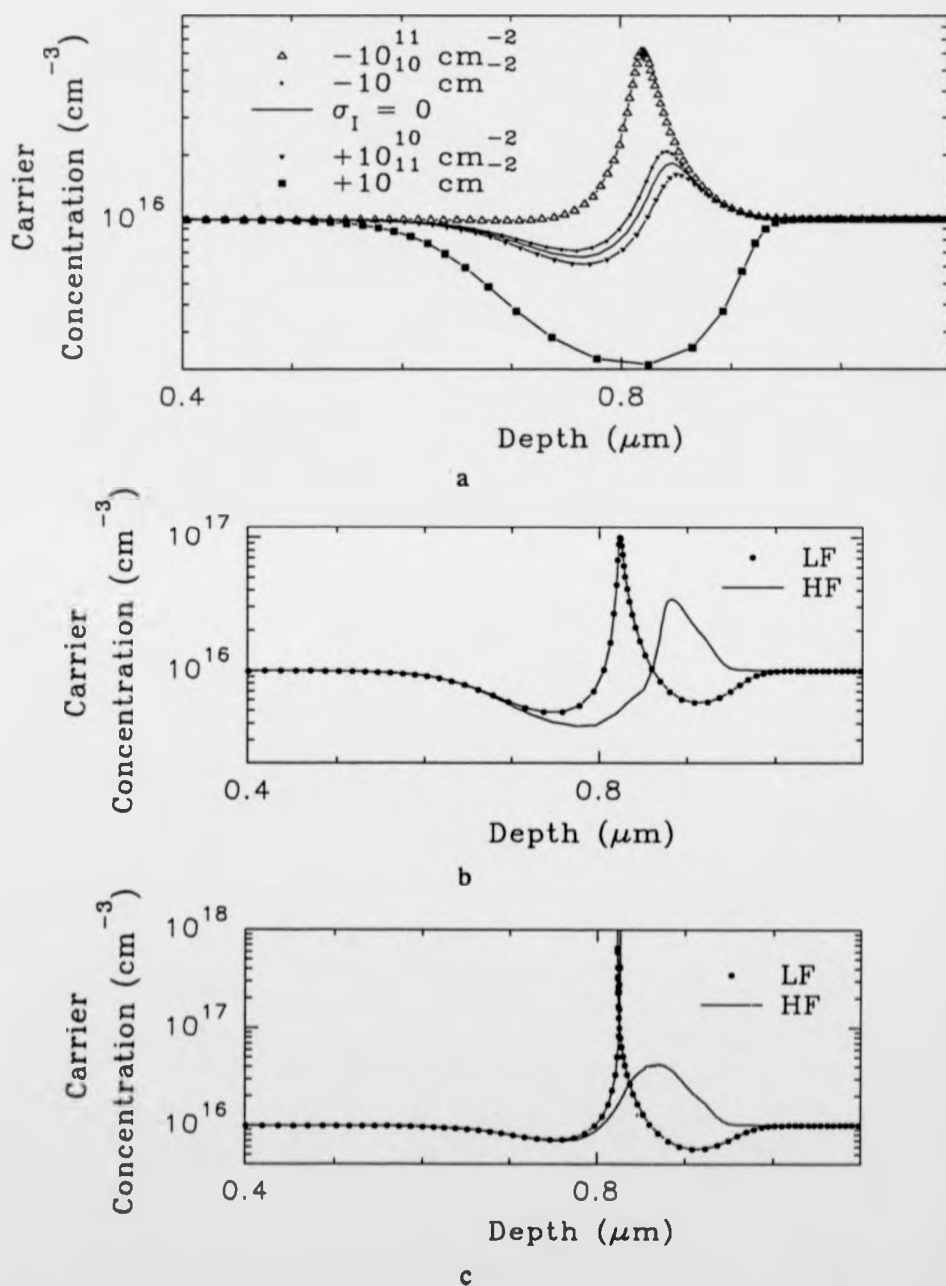


Table 4.1 Extracted band offsets and interface charge densities for various interfacial trap densities and type (band offset=0.08eV at 0.8 μ m according to Fig 4.13a-c).

Trap Type	Input σ_I (cm ⁻²) - Acceptor, + Donor	Extracted ΔE_V (eV)	Extracted σ_I (cm ⁻²)
Fixed	-10 ¹¹	0.079	-2x10 ¹¹
Fixed	-10 ¹⁰	0.078	-2.12x10 ¹⁰
Fixed	+10 ¹⁰	0.078	+1.87x10 ¹⁰
Fixed	+10 ¹¹	0.074	+1.98x10 ¹¹
$E_T=0.25\text{eV}$ LF	-10 ¹¹	0.006	-5.76x10 ⁹
$E_T=0.25\text{eV}$ HF	-10 ¹¹	0.278	-1.85x10 ¹¹
$E_T=0.25\text{eV}$ LF	-10 ¹⁰	0.077	-2.1x10 ¹⁰
$E_T=0.25\text{eV}$ HF	-10 ¹⁰	0.097	-1.93x10 ¹⁰
$E_T=0.25\text{eV}$ LF	+10 ¹⁰	0.077	-2.05x10 ⁹
$E_T=0.25\text{eV}$ HF	+10 ¹⁰	0.096	+3.31x10 ⁸
$E_T=0.25\text{eV}$ LF	+10 ¹¹	0.075	-2.68x10 ⁹
$E_T=0.25\text{eV}$ HF	+10 ¹¹	0.233	+1.15x10 ¹⁰

$1.87 \times 10^{10} \text{ cm}^{-2}$ (donor) apparent interfacial charge densities respectively, indicating the improved accuracy in band offset extraction for reduced interfacial charge.

Deep Interface Traps

The problem becomes greater in the presence of deep traps whose occupancy can change during measurement. In the limit of large reverse bias:

$$\sigma_{\text{Imeas}} \rightarrow \sigma_{\text{I}} \text{ (acceptor)}$$

$$\sigma_{\text{Imeas}} \rightarrow 0 \text{ (donor)}$$

This assumes that both trap types have emitted the trapped charge and in the case of the donor traps, the integration limits encompass both the compensation effect, observed as a dip in the carrier profile at the trap location, and the trap emission, observed as a peak in the carrier profile at some deeper position relative to the trap location.

Of greater importance is the problem of trap response at the measurement signal frequency. Such effects are illustrated in Fig 4.13b&c for 10^{11} cm^{-2} donor and acceptor traps respectively at 0.25eV above the valence band edge; subsequent extraction of band offsets and interface charge densities are given in Table 4.1. LF simulated profiles yielded the most accurate values for band offset (donor and acceptor traps) and interface charge density (acceptor traps alone) although this was for an interfacial charge density of 10^{10} cm^{-2} . For an interfacial charge density of 10^{11} cm^{-2} , only the LF donor trap case yielded sensible values for band offset whereas only the HF acceptor trap case yielded sensible values for interface charge density. Clearly, the presence of such interfacial traps would have a significant effect on the extracted heterointerface parameters.

For completeness the situation of trap distributions close to the heterojunction as proposed by Leu *et al.* [4.12] were also considered. Simulations were carried out exactly as for the previous interfacial charge case except the sheet charge densities were converted to block trap concentrations between 0.8 and 0.81 μm i.e. on the narrow band-gap side of the heterojunction. From section 3.2.3.4, (3.38) is no longer valid; for this

situation, it is necessary to evaluate (3.44) and provide a correction in the numerical integration procedure. Rewriting (3.44) gives:

$$\Delta\phi(0) = \Delta\phi(\sigma) \pm \frac{q}{\epsilon_0 \epsilon_r} \left[\int_{x_I}^{x_I^*} N_T^*(x^*)(x^* - x_I^*) dx^* - \int_{x_I}^{x_I^*} N_T^*(x^*) \Delta x_I dx^* \right] \quad (4.4)$$

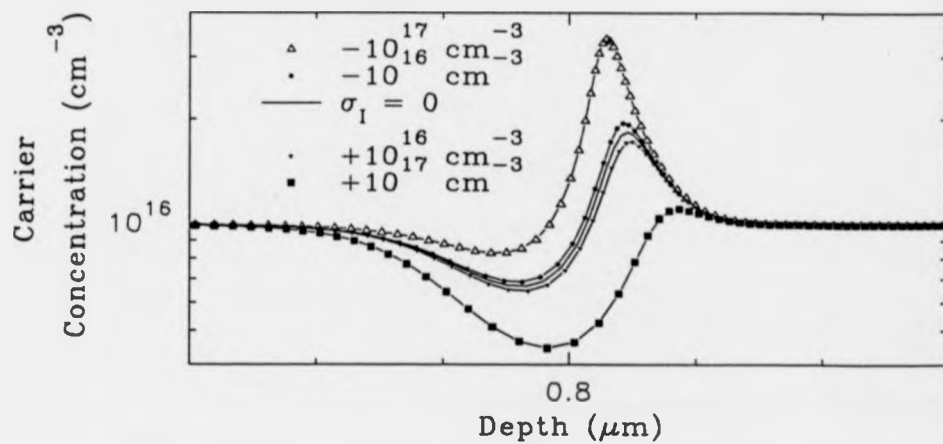
where $\Delta x_I = x_I - x_I^*$ is the difference between the real and assumed heterointerface position, x_I^* being the apparent interface position. Assuming a uniform trap distribution, $N_T^*(x^*)$ between x_I and $x_I + d$ and the traps to be of the fixed charge type such that the trap distribution directly relates to the measured interface charge density via (3.40), then (4.4) may be evaluated as:

$$\Delta\phi(0) = \Delta\phi(\sigma) \pm \frac{q\sigma_I}{\epsilon_0 \epsilon_r} \left[\frac{d}{2} - \Delta x_I \right] \quad (4.5)$$

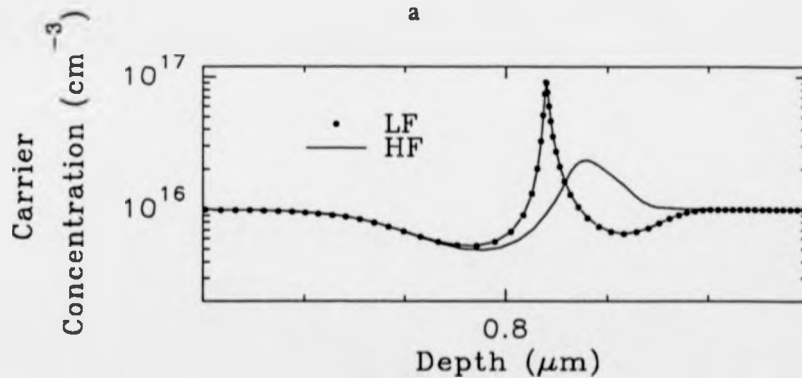
Asymmetric fixed charge trap distributions are shown in Fig 4.14a whilst extracted band offsets and interface charge densities are given in Table 4.2. Interface charge density and band offset, without the correction term of (4.5), were in good agreement with the input parameters except for the donor trap case, $N_T = +10^{17} \text{ cm}^{-3}$. Use of the correction term in (4.5) (assuming $\Delta x_I = 0$ and $d = 0.01 \mu\text{m}$) was found to decrease the extracted band offset for acceptor traps whilst improving the accuracy of extracted band offset for donor traps. Clearly care is required in applying this correction to experimentally determined values as trap distributions within the integration limits but removed from the heterojunction will all contribute to the extracted interface charge density which, along with the choice of d , could result in large error. Asymmetric deep trap distributions are shown in Fig 4.14b&c for 10^{17} cm^{-3} donor and acceptor traps respectively; extracted band offset and interface charge densities are given in Table 4.2. As before, distortion of the profiles was observed; LF carrier profiles yielded the most accurate values of band offset (donor and acceptor traps) and interface charge density (acceptor traps alone) for trap concentrations 10^{16} - 10^{17} cm^{-3} . For a trap concentration of 10^{17} cm^{-3} , only the case of acceptor traps in the HF regime yielded sensible values for interface charge density; because it is difficult in practice to accurately

Fig 4.14

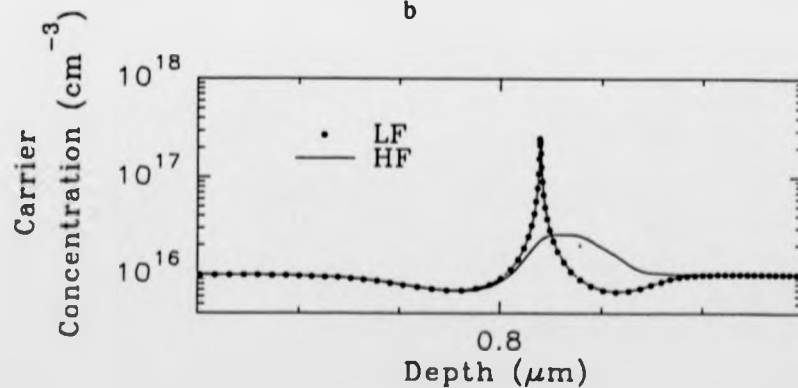
Simulated apparent free carrier distributions for: a) fixed charge, b) deep donor and c) deep acceptor traps positioned between x_I and $x_I + 0.01 \mu\text{m}$ (with x_I and band offset as for Fig 4.13).



a



b



c

Table 4.2 Extracted band offsets and interface charge densities for various trap densities and type distributed between 0.8-0.81 μm (band offset=0.08eV at 0.8 μm according to Fig 4.14a-c; NC/C denote no correction/ correction according to (4.5) for extraction of the band offsets).

Trap Type	Input N_T (cm^{-3}) - Acceptor, + Donor	Extracted ΔE_V (eV)	Extracted σ_I (cm^{-2})
Fixed	-10^{17}	NC 0.084 C 0.077	-8.83×10^{10}
Fixed	-10^{16}	NC 0.078 C 0.077	-9.72×10^9
Fixed	$+10^{16}$	NC 0.077 C 0.077	$+7.68 \times 10^9$
Fixed	$+10^{17}$	NC 0.071 C 0.077	$+8.62 \times 10^{10}$
$E_T=0.25\text{eV}$ LF	-10^{17}	NC 0.083 C 0.076	-8.89×10^{10}
$E_T=0.25\text{eV}$ HF	-10^{17}	NC 0.168 C 0.162	-8.15×10^{10}
$E_T=0.25\text{eV}$ LF	-10^{16}	NC 0.078 C 0.077	-9.97×10^9
$E_T=0.25\text{eV}$ HF	-10^{16}	NC 0.087 C 0.086	-9.1×10^9
$E_T=0.25\text{eV}$ LF	$+10^{16}$	NC 0.077 C 0.077	$+1.27 \times 10^9$
$E_T=0.25\text{eV}$ HF	$+10^{16}$	NC 0.086 C 0.086	-3.31×10^8
$E_T=0.25\text{eV}$ LF	$+10^{17}$	NC 0.076 C 0.076	-1.71×10^9
$E_T=0.25\text{eV}$ HF	$+10^{17}$	NC 0.157 C 0.158	$+5.44 \times 10^9$

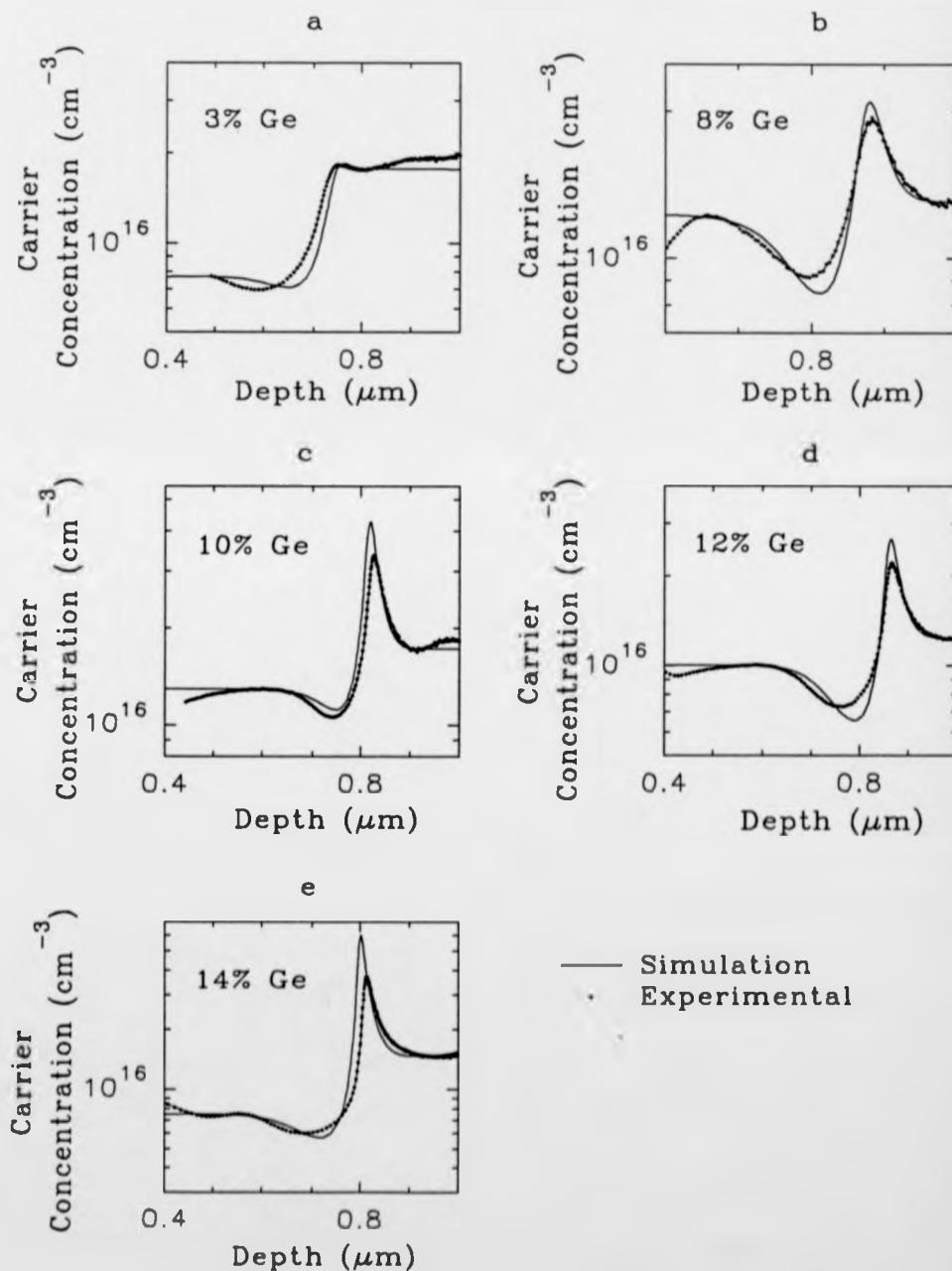
determine trap distributions and make a complete correction according to (3.44), (4.5) would seem a logical choice. However, use of (4.5) with $d=0.01\mu\text{m}$ and $\Delta x_I=0$ produces little change in the extracted band offset, for the cases of underestimated values of interface charge, and certainly could not be used to correct for the HF case of 10^{17} cm^{-3} donor or acceptor traps.

Hence the approach adopted by Leu *et al.* in correcting the band offset over the HF/low temperature regime should be viewed with caution. Furthermore, one has to question the real, physical reasons for these dramatic changes in the heterojunction parameters at some transition temperature. The work of Lee *et al.* [4.15] uses the approach of Leu *et al.* to correct for the apparent reduction in conduction band offset for $T\leq 160\text{K}$. The bulk apparent carrier concentrations were observed to change as temperature was reduced (in a similar manner to observations made in this work). If fixed values of uniform doping level (estimated from the bulk carrier distributions) are assumed for all temperatures and the apparent free carrier concentration is seen to decrease at reduced temperatures, error will be introduced into the extracted heterojunction parameters as a result of bulk effects away from the heterojunction. Whilst it is unclear what bulk levels are assumed in the previous publications, this problem is avoided here by assuming that the apparent free carrier concentration = bulk doping level (for the integration limits) at each measurement temperature; it should, for this reason, reflect more realistically the effect of the band offset and interfacial charge on the free carriers in the heterojunction region.

In view of these results, valence band offset and interface charge densities extracted from the experimental data were used as input parameters to the simulation program; the resulting match at $T=248\text{K}$ is shown in Fig 4.15a-e for the various Ge compositions investigated. Interface charge was chosen to be of the fixed charge trap type and although bulk traps have not been considered (this will be discussed next), there would appear to be reasonable agreement between the simulated and experimental carrier profiles. The introduction of interface charge has caused a shift of the peak

Fig 4.15

Simulated and experimental match between apparent free carrier distributions for various Ge compositions at $T=248\text{K}$. The experimentally extracted interface charge densities are placed at the assumed heterointerface position in each case.



position from the initial simulations used with $\sigma_I=0$ (used to determine x_I) and indicates that the initial choice of x_I may have been incorrect. Compare this to the matched carrier profiles in Fig 4.16a-e at $T=248K$, where the extracted interface charge density has been converted to a bulk trap concentration between x_I and $x_I+0.01\mu m$ and used as input to the simulation program. The shift in peak position observed in Figs 4.15 has essentially been removed and in the case of the 10% Ge composition sample, the match is very good.

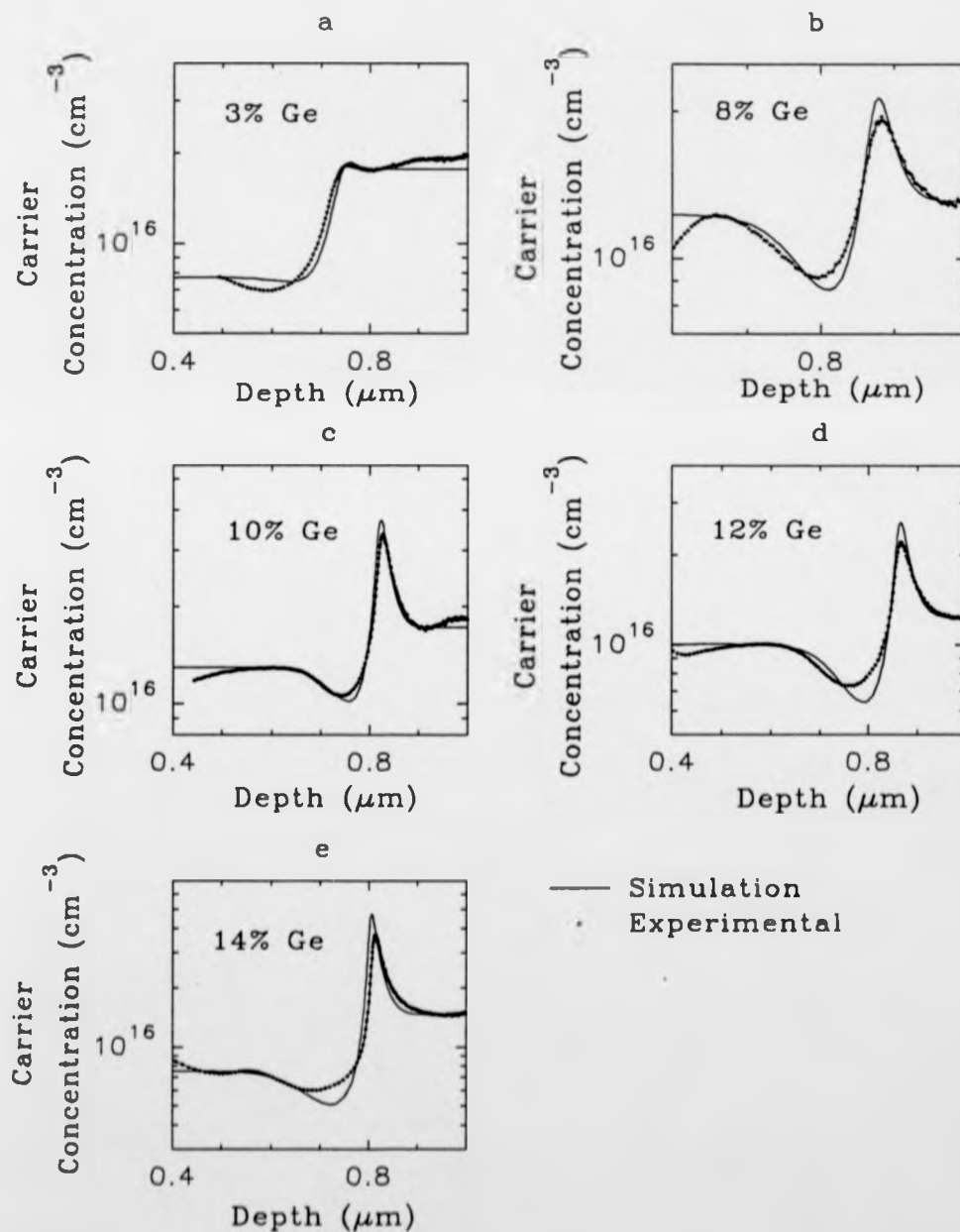
These comparisons indicate the iterative nature of matching simulation to experimental data; clearly care is required in the initial extraction of the heterojunction parameters and one should be aware of the possible distortion that can occur due to the presence of traps at, or near to, the heterojunction. However, it is clear that there is good reproducibility in the extraction of the valence band offset and interface charge density and, importantly, the use of (3.38) without correction would appear valid for the experimental data presented here. The extracted interfacial charge densities are consistent with the minimal distortion observed in the experimental free carrier profiles and, as a consequence, reflects the accuracy with which values for the extracted valence band offset are obtained. Furthermore, the temperature independent behaviour of the extracted interfacial charge suggests the traps in this region are of the fixed charge type; at present, it is unclear whether the traps are interfacial or distributed close to the heterojunction.

We are now in a position to discuss the qualitative features of the apparent free carrier distributions for the 12% Ge composition sample, in view of the detailed analysis previously discussed and bulk trap distributions as determined by DLTS (section 5.3).

The marked decrease in the apparent free carrier concentration within the Si cap as temperature was reduced may be attributed first to trapping level D(0.482eV), and then level B(0.306eV), making the transition from the HF to VHF regime for $T < 200K$. Consider the apparent trap profile in Fig 5.8d, showing a higher trap concentration towards the surface, falling off for greater depth into the epilayer towards the

Fig 4.16

Simulated and experimental match between apparent free carrier distributions for various Ge compositions at $T=248\text{K}$. The experimentally extracted interface charge densities are converted into bulk trap distributions between the assumed heterointerface position, x_I and $x_I+0.01\mu\text{m}$ in each case.



heterojunction: if acceptor-like, the carrier profile would show a raised section reflecting the trap distribution at some deeper spatial position - this is not observed; if donor-like, the carrier profile would show a compensated region at the actual trap location as a mirror-image of the trap distribution, similar to that observed. Note the enhanced depletion in the vicinity of the heterojunction, at these reduced temperatures, makes the apparent compensation effect greater towards the heterojunction and does not necessarily reflect the trap concentrations in this region.

The enhanced depletion and accumulation feature seen at the first heterojunction, at reduced temperatures, is a consequence of the increasing confinement of carriers in the well, on the $\text{Si}_{0.88}\text{Ge}_{0.12}$ side of the heterojunction; the enhanced depletion on the the Si side of the heterojunction follows as a result of this. The fact that these features do not change shape or shift in position is indicative of the features being related to the valence band-offset alone; this is verified by the accuracy of the extracted heterojunction parameters - note the extracted interface charge densities would cause minimal distortion to the heterojunction depletion and accumulation feature according to the simulations. The sharpness of the features may also be attributed, in part, to the reduction of the Debye length at low temperatures, so increasing the resolution of the C-V measurement technique.

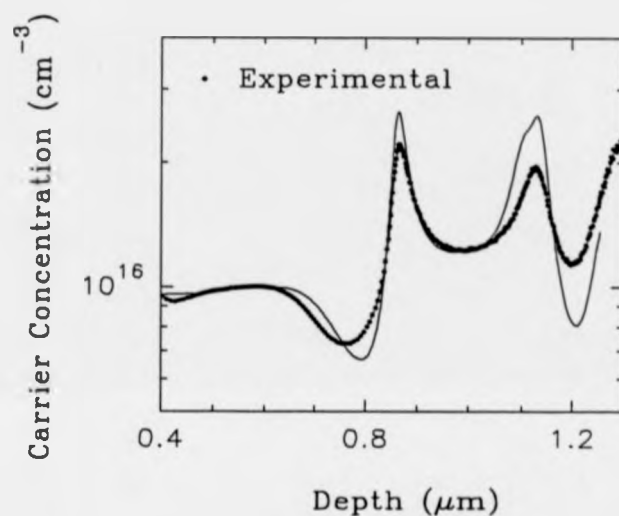
Moving into the $\text{Si}_{0.88}\text{Ge}_{0.12}$ layer, deep level concentrations are observed to increase by an order of magnitude; because of the distortion observed in the DLTS in the heterojunction region, exact trap distributions are questionable. However, away from the first heterojunction, trap distributions were determined with more confidence and indicated a gradual decrease in concentrations as the second heterojunction was approached. Marked changes were observed in the apparent free carrier distributions as temperature was reduced. At 348K a shoulder is seen following the peak associated with the first heterojunction; this shoulder disappears as temperature is reduced. If such a feature was associated with trap emission on crossing the Fermi level it would be expected to see this feature down to 200K, below which certain traps enter the VHF regime and retain the trapped carriers; this is not observed. The shoulder is seen to

disappear between 298K and 248K and is accompanied by a decrease in the apparent free carrier concentration and shift of the second heterojunction peak to greater depth; these observations suggest a transition from the LF to HF regime for trap response, although the observed distortion in the LF regime is minimal and it is not clear which level is responsible for this. If a triangular trap distribution is considered in the alloy layer with a peak at approximately $1\mu\text{m}$, the observed decrease in the carrier concentration at reduced temperatures would represent a mirror-image of the trap distribution, assuming the traps to be donor-like; indeed, the dip that occurs at approximately $1.04\mu\text{m}$ for $T < 150\text{K}$ corresponds well with the level B(0.314eV) moving from the HF into the VHF response regime. The subsequent emission of trapped carriers, for trap response in the HF regime, may explain the broadening of the second peak; the fact that the second heterojunction peak shows a shift to greater depth with reduced temperature suggests some contribution due to trap emission (as the Fermi level approaches the valence band edge at low temperatures, trap features will be observed at locations ever further from their true position as a consequence of the change in trap crossing point with the Fermi level); the magnitude of this contribution is reduced at the lowest temperatures as the traps enter the VHF regime.

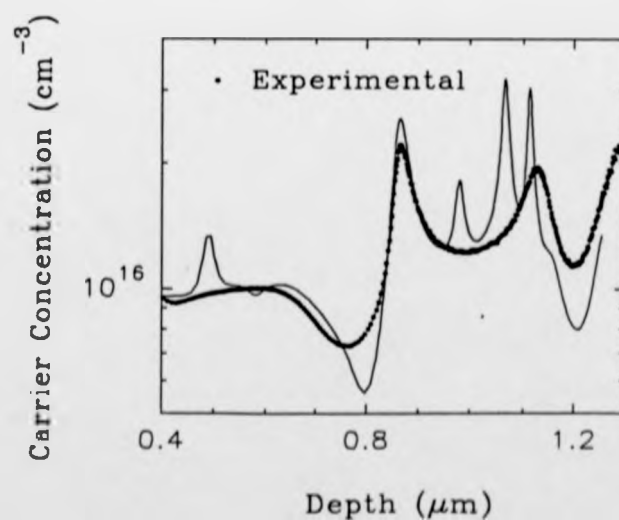
Simulations were carried out assuming doping levels of $1 \times 10^{16} \text{ cm}^{-3}$ and $1.4 \times 10^{16} \text{ cm}^{-3}$ for the Si and $\text{Si}_{0.88}\text{Ge}_{0.12}$ regions respectively and corrected donor trap distributions assumed as in Fig 5.8d, according to section 5.5. Results are shown in Fig 4.17a&b, for the HF and LF cases respectively, matched to experimental data at 248K. Extracted interface charge density has been converted to a bulk trap distribution between $0.83\text{-}0.84\mu\text{m}$ on the $\text{Si}_{0.88}\text{Ge}_{0.12}$ side of the first heterojunction and a band offset of 0.083eV was assumed at both heterointerfaces. A reasonable match is achieved in the HF case and note the effects of compensation in the bulk regions, either side of the first heterojunction, are well evident, justifying the assumption of the traps being donor-like in nature. Error in the exact trap distribution in the vicinity of the first heterojunction may well explain the differences observed between the simulated and experimental depletion and accumulation features. The second heterojunction peak

Fig 4.17

Simulated and experimental match between apparent free carrier distributions for sample #28/17 at $T=248\text{K}$, incorporating the corrected trap distributions according to Fig 5.8d: a) HF and b) LF simulations.



a



b

feature shows the effects of broadening due to trap emission; note the discrepancy between the simulated and experimental features suggests a smaller band offset as compared to the first heterojunction. This could represent some degree of mismatch at the lower heterointerface, with a resultant change in valence band offset; strain relaxation is more likely to occur at this interface, according to the relaxation processes and observations reviewed in Chapter 2. However, if such relaxation was to occur and the first (upper) heterojunction maintained its coherency, the change in lattice constant would result in both the Si cap and underlying alloy layer being in a strained state. This would subsequently affect the valence band offset at the first heterojunction; within the experimental error, the extracted valence band offsets do not indicate a deviation away from the theoretically predicted values for strained lattice-matched $\text{Si}_{1-x}\text{Ge}_x$ on cubic Si. The LF case is shown to indicate the gross distortion that would be expected should the trap distribution be able to respond at the measurement signal frequency; the dominant trapping levels undergo the transition LF to HF response for temperatures just below 300K. This further validates the HF match to experimental data at 248K, but the shoulder observed for $T \geq 300\text{K}$ and attributed to LF trap response is much more subtle. A good degree of reproducibility has thus been shown, despite the discrepancies that were observed in the matching of the simulated to experimental carrier profiles for uniform Si alone; the various limitations discussed for the uniform Si layers are equally applicable in this case. One may conclude that the deep level distributions in the bulk and in the vicinity of the first heterojunction have contributed minimal distortion to the free carrier profiles, so reflecting the accurate determination of the valence band offsets. It is important to stress that the trends and detailed analysis presented here for the 12% Ge composition alloy are equally applicable to the other metastable layers and sample #28/17 has only been chosen as representative of these. Differences between the 24 and 28 growth series Si/ $\text{Si}_{1-x}\text{Ge}_x$ /Si samples may be considered in a similar way to those for the uniform Si samples and will not be discussed here.

The origin of the interface charge is not clear; results discussed in section 5.6 consider the bulk deep levels to be point defect/dislocation related and donor-like in nature whilst the extracted interface charge was consistently acceptor-like. DLTS will not detect fixed charge traps whose charge state remains bias and temperature independent. The accuracy of the extracted valence band offsets suggest that the strained integrity of the first heterointerface has been maintained. This is verified by the low misfit dislocation densities observed (see section 5.4), which are not seen to scale with the changing interface charge densities determined for the various Ge compositions; this suggests the origins of the interfacial charge does not lie with such interfacial defects, in contrast to the work of Tatsumi *et al.* [4.19]. From Chapter 5, the reduction in bulk trap distributions, for high growth temperature or anneal treatments, is considered the result of the removal of point defect species from the dislocation environment; the fact that no observed reduction in interface charge density is seen in Fig 4.8b for the higher growth temperature sample further suggests it to be unrelated to misfit dislocations. A more probable origin of the interface charge is from the incorporation of the Ge into the growing Si matrix and the definition of the first heterojunction. The increasing electrical activity observed via DLTS for increasing Ge composition at the $\text{Si/Si}_{1-x}\text{Ge}_x$ heterointerface may reflect the degree of disorder on an atomic scale at, or near to, the heterointerface which, in turn, may give rise to acceptor-like levels. Indeed, the influence of interface impurity scattering on hole mobilities in 2DHG structures grown at Warwick was consistent with interface charge densities of the order 10^{11} cm^{-2} for 20% Ge composition alloys [4.32] - this is in reasonable agreement with the work presented here, assuming an increasing interface charge density for increasing Ge composition. However, such states were considered to be the result of gettering of metallic species to the interface; whilst TEM results presented in section 5.4 indicate evidence of gettering, it is not preferential to the interface. Furthermore, improvements in the hole mobilities for increased growth temperature were considered to be the result of metallic removal and lower interface charge densities

[4.22]; higher growth temperature did not reduce the interface charge density observed in this work. The exact nature of such states is not clear at present.

The marked changes in the apparent free carrier distributions at low temperatures and for higher Ge composition alloys was particularly interesting in view of the similar observations widely reported in the literature (see section 4.2 and references therein). This marked change corresponded to a decrease in the measured device capacitance and was observed in the 14% Ge composition alloy for $T < 100\text{K}$ and for the 20% Ge composition alloy for $T < 130\text{K}$; these effects will be discussed for the latter case, where the trends were more obvious.

The temperature dependence of the device capacitance is shown in Fig 4.18a as a function of various reverse biases; a marked decrease in capacitance is shown to occur between 110-130K whilst the effect is shown to be removed on extending the reverse bias $\leq -8\text{V}$. For reverse biases less than -8V , the Schottky depletion edge has extended through the $0.1\mu\text{m}$ thick alloy layer; this suggests that the observed effects are directly related to the alloy layer itself. The measured capacitance for reverse biases $\geq -8\text{V}$ and $T \geq 130\text{K}$ yields an apparent free carrier profile that is in good agreement with the intended growth specifications, in terms of doping level and the position of the first heterojunction feature matching to the topmost heterointerfacial position Fig 4.9. This suggests, contrary to previous considerations [4.8, 4.9] that, in this case, the capacitance is in error for $T \leq 130\text{K}$ and not vice-versa, where it was considered that traps contributed to the measured capacitance above a transition temperature which marked the LF to HF trap response regimes. Consideration of emission rates for the observed deep levels did not show any correlation to such a LF to HF transition at $T \approx 130\text{K}$ and, as such, does not explain the changes observed here. However, it is possible that the admittance associated with the heterojunction will undergo a change at low temperatures, making the apparent capacitance of the heterojunction comparable to that of the Schottky, resulting in the observed reduction in the measured device capacitance. Consider Fig 4.18b&c which illustrate the measured conductance and

Fig 4.18a Variation of the measured device capacitance as a function of temperature for various reverse bias conditions.

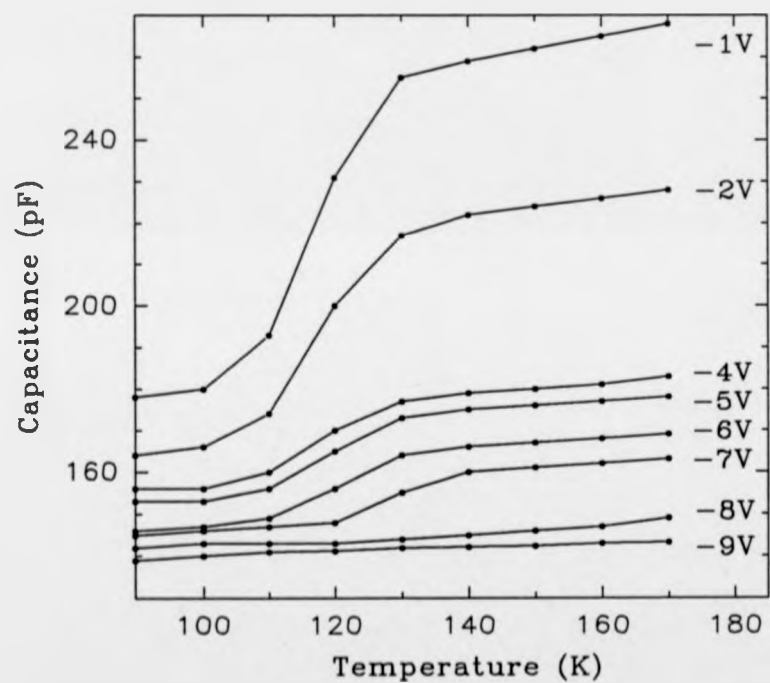


Fig 4.18b Variation of the measured device conductance as a function of reverse bias around the transition temperature.

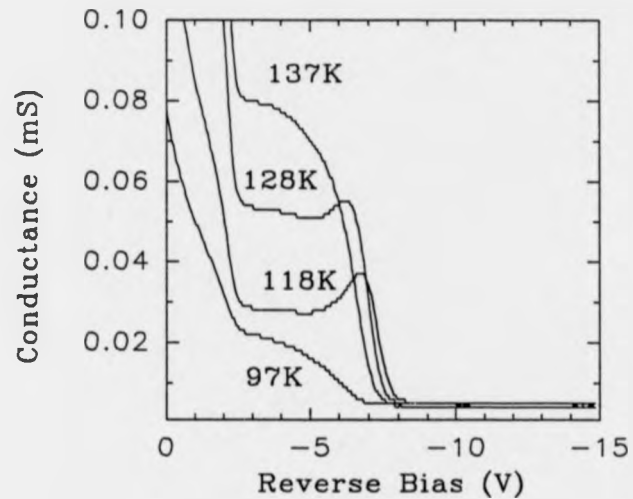
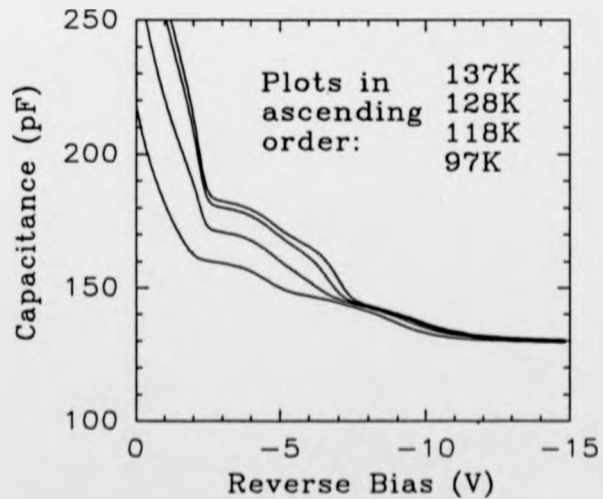


Fig 4.18c Variation of the measured device capacitance as a function of reverse bias around the transition temperature.



capacitance versus reverse bias respectively of the device around the transition temperature. The alloy region is well defined between -3 and -7V reverse bias and it is in this region that dramatic changes occur in the conductance, which is observed to decrease as temperature is lowered below $\sim 137\text{K}$. Whilst the complete equivalent circuit analysis would be complex, these changes may be considered qualitatively: at high temperatures, the carrier mobility is such that the carrier movement over the hetero-barrier is unheeded - in this situation, the conductance term across the hetero-barrier is in parallel with the capacitance associated with the heterojunction and at high temperature, the dominant term of the heterojunction admittance is the conductance. Assuming this to be large at high temperatures, the overall device admittance will measure the depletion capacitance associated with the Schottky diode alone. As temperature is reduced, the conductance component across the heterojunction decreases; the contribution to the overall device admittance from the capacitance associated with the heterojunction will increase, with the result that the overall device admittance indicates a decreasing capacitance, so producing the effects observed. Note this implicitly assumes that the Schottky and heterojunction depletion capacitance are comparable in magnitude. The effect on the 14% composition sample occurs at a lower transition temperature still since the valence band-offset is smaller.

Finally a comment is appropriate regarding the relaxed sample #24/19. This has been included purely to illustrate the increased changes observed in the apparent free carrier concentration as temperature is lowered; if the high dislocation density in this layer was considered to introduce donor-like deep states into the bulk layers, these would adequately account for the large, observed compensation effects. The reduced peak features at both heterojunctions will be a consequence of this, along with a probable reduction in valence band offset, due to the increased degree of mismatch at the heterointerfaces.

CONCLUSION

Apparent free carrier distributions have been determined via C-V techniques for a variety of Si and Si/Si_{1-x}Ge_x/Si layers. Features observed have been discussed in relation to trapping levels determined in Chapter 5; furthermore, numerical integration of the carrier profiles for the alloy layers has allowed extraction of interface charge densities and valence band offsets, the latter being in good agreement to theoretically determined values. The effect of traps positioned at or near to the heterojunction on these extracted parameters was investigated using simulation; it is concluded that minimal distortion has occurred to the experimentally determined carrier profiles and that the interface charge is of a fixed charge type. Simulations were used to reconstruct the carrier profiles; some agreement is found although such processes are iterative, being subject to various sources of error. From such comparison of simulated and experimental data, the effect of traps in the bulk and close to the heterojunction are considered to have a small effect on the carrier profile and reflects the high degree of accuracy in the extracted valence band offsets. Temperature dependence of the carrier profiles suggests possible compensation effects ie. donor-like traps, which is in good agreement with the results presented in Chapter 5.

REFERENCES

- 4.1 C. T. Sah and V. G. K. Reddi IEEE Trans. Elec. Dev. ED 11 (1964) 345
- 4.2 G. I. Roberts and C. R. Crowell J. Appl. Phys. 41 (1970) 1767
- 4.3 L. C. Kimerling J. Appl. Phys. 45 (1974) 1839
- 4.4 A. Morii, H. Okagawa, K. Hara, J. Yoshino and H. Kukimoto
Jap. J. Appl. Phys. 31 (1992) L1161
- 4.5 M. O. Watanabe, J. Yoshida, M. Mashita, T. Nakanisi and A. Hojo
J. Appl. Phys. 57 (1985) 5340
- 4.6 P. Z. Lee, C. L. Lin, J. C. Ho, L. G. Meiners and H. H. Wieder
J. Appl. Phys. 67 (1990) 4377
- 4.7 I. D. Hawkins PhD. Thesis UMIST (1989)
- 4.8 K. Kazmierski, P. Philippe, P. Poulain and B. de Cremoux
J. Appl. Phys. 61 (1987) 1941
- 4.9 M. Ogura, M. Mizuta, K. Onaka and H. Kukimoto
Jap. J. Appl. Phys. 22 (1983) 1502
- 4.10 S. R. Forrest and O. K. Kim J. Appl. Phys. 53 (1982) 5738
- 4.11 G. W. t'Hooft and S. Colak Appl. Phys. Lett. 48 (1986) 1525
- 4.12 L. Y. Leu and S. R. Forrest J. Appl. Phys. 64 (1988) 5030
- 4.13 H. Kroemer, W.-Yi. Chien, J. S. Harris Jr. and D. D. Edwall
Appl. Phys. Lett. 36 (1980) 295
- 4.14 L. Y. Leu and S. R. Forrest J. Appl. Phys. 65 (1989) 4818
- 4.15 C. D. Lee and S. R. Forrest J. Appl. Phys. 69 (1991) 342
- 4.16 P. S. Whitney and C. G. Fonstad J. Cryst. Growth 83 (1987) 219
- 4.17 H. Okumura, S. Misawa and S. Yoshida Surf. Sci. 174 (1986) 324
- 4.18 M. W. Denhoff, J. -M. Baribeau, D. C. Houghton and K. Rajan
J. Cryst. Growth 81 (1987) 445
- 4.19 T. Tatsumi, H. Hirayama and N. Aizaki Appl. Phys. Lett. 52 (1988) 895

- 4.20 C. A. King, J. L. Hoyt, D. B. Noble, C. M. Gronet, J. F. Gibbons,
M. P. Scott, T. I. Kamins and S. S. Laderman
IEEE Elec. Dev. Lett. ED 10 (1989) 159
- 4.21 G. I. Andersson and O. Engström J. Appl. Phys. 69 (1991) 4418
- 4.22 D. W. Smith, C. J. Emeleus, R. A. A. Kubiak,
E. H. C. Parker and T. E. Whall Appl. Phys. Lett. 61 (1992) 1453
- 4.23 E. H. Rhoderick and R. H. Williams "Metal-Semiconductor contacts"
2nd Ed. (Clarendon Press, Oxford 1988) 139
- 4.24 (as for 4.23) 38
- 4.25 (as for 4.23) 125
- 4.26 M. O. Aboelfotoh and K. N. Tu Phys. Rev. B. 34 (1986) 2311
- 4.27 A. M. Cowley Sol. St. Elec. 12 (1970) 403
- 4.28 S. P. Muraka J. Vac. Sci. Technol. 17 (1980) 775
- 4.29 P. Kramer, C. de Vries and L. J. van Ruyven
J. Electrochem. Soc. 122 (1975) 314
- 4.30 D. I. Babic and H. Kroemer Sol. St. Electron. 28 (1985) 1015
- 4.31 R. People and J. C. Bean Appl. Phys. Lett. 48 (1986) 538
- 4.32 C. J. Emeleus, T. E. Whall, D. W. Smith, R. A. A. Kubiak,
E. H. C. Parker and M. J. Kearney J. Appl. Phys. 73 (1993) 3852

CHAPTER 5

DEEP LEVEL DISTRIBUTIONS IN Si AND SiGe

5.1 INTRODUCTION

This chapter will report an investigation into deep level distributions in Si and Si/Si_{1-x}Ge_x/Si layers grown by MBE. Using DLTS as the primary characterisation technique, trap activation energies and deep level concentrations were extracted as a function of depth into the epilayers; these parameters have already been considered in Chapter Four for the reconstruction of the C-V determined apparent free carrier concentration profiles and to discuss the effect of trapping states on the measured profiles. Comparison to published data is made; combining these results with those obtained via X-ray, TEM and defect etch techniques has allowed the nature and possible identification of the observed electrically active states to be made. Simulations are used to match to the experimental deep level spectra in order to determine the validity of the technique and investigate the "band of energies", as opposed to single energy level, proposed for dislocation and alloy related band-gap states.

5.2 DEEP LEVELS IN Si, SiGe AND III-V ALLOY SYSTEMS

DLTS analysis in MBE Si layers has found considerable variation in deep level concentrations and activation energies, with the bulk of the work having been carried out in n-type material [5.1-4]. Results from different sources show dramatic variation in deep level species and concentration, ranging between 10^{12} to 10^{16} cm⁻³ [5.1]; Xie *et al.* [5.2] report very broad spectra, with a single deep level $E_c-0.58$ eV at approximately 10^{15} cm⁻³ which is reduced below the detection limit ($\leq 10^{12}$ cm⁻³) for subsequent substrate precleans (attributed to C removal from the substrate surface); Sidebotham *et al.* [5.4] reported deep state concentrations decreasing with increasing

growth temperature to approximately 10^{12} cm^{-3} at $T_s=795^\circ\text{C}$. In this latter case, the gradual change was attributed to intrinsic defects (vacancies at $E_c-0.53\text{eV}$ and $E_c-0.3\text{eV}$) whilst the sharp transition was attributed to deep states associated with Ta ($E_c-0.53\text{eV}$) and decorated dislocations ($E_c-0.32\text{eV}$). This sharp transition was suggested to be the result of the change in nature of metallic species incorporation in the growing epilayer. In all cases, the deep level concentration was observed to increase towards the epilayer/substrate interface. In contrast, both Gravesteijn *et al.* [5.5] and Ota [5.6] report DLTS studies in MBE Si yielding deep level concentrations below the detection limit of the technique. Further to previous work, Sidebotham [5.7] concludes the high deep level concentration observed at low T_s is due to disordered growth and hence the fundamental limit of low deep state concentration is set not by the degree of impurity contamination but by the growth temperature.

Nagesh *et al.* [5.8] provided the first published data concerning deep levels in CVD grown $\text{Si}_{1-x}\text{Ge}_x$ for Ge fractions 3.4%, 7% and 14.9%. The layers were approximately $15\mu\text{m}$ in thickness and, for a $T_s=1000-1200^\circ\text{C}$, should have been in a fully relaxed state, although this is not discussed. Two or more deep levels were found in the upper half of the alloy band-gap depending upon the Ge fraction; details are given for only one of these levels, common to all samples, and it is suggested this level has been observed in Czochralski SiGe bulk alloys but no reference is given. The asymmetry of the peak is similar to those attributed to dislocations - however capture measurements do not exhibit the logarithmic filling behaviour considered indicative of such extended defects. In a following publication, Nagesh *et al.* [5.9] report a mid-gap level induced by heat treatment which was found in all SiGe alloys studied and which varied between 10^{11} to $4 \times 10^{12} \text{ cm}^{-3}$. Whilst the origins of this defect are discussed, the possibility of it being a dislocation-related feature seems to have been ignored. Deep state concentrations less than $5 \times 10^{13} \text{ cm}^{-3}$ were reported for as-grown CVD $\text{Si}_{1-x}\text{Ge}_x$ [5.10] layers with Ge fractions 12% and 16%; significant deep levels were introduced following electron irradiation treatment. Bremond *et al.* [5.11] report DLTS

for $\text{Si}_{0.86}\text{Ge}_{0.14}/\text{Si}$ structures for a variety of thicknesses intended to study the onset of relaxation. Spatially resolved spectra is only achieved for the thickest samples: a trap at $E_v+0.38\text{eV}$ is found in the overlying $\text{Si}_{0.86}\text{Ge}_{0.14}$ layer at $1.2 \times 10^{14} \text{ cm}^{-3}$ and is attributed to 60° threading dislocations whilst a trap at $E_v+0.51\text{eV}$, with an interfacial density of $4 \times 10^{11} \text{ cm}^{-2}$, is considered related to misfit dislocations. It is not clear how this latter interfacial density is obtained nor why it is considered localised at the heterojunction. As the alloy layer thickness is reduced, both trap densities (volume and sheet) decrease; however the interpretation of the results presented seems extremely ambiguous, both in resolving particular trap peaks and the spatial position of these states.

Despite the maturity of the III-V material system, deep level studies are not in abundance. Lattice matched $\text{In}_{0.53}(\text{Ga}_x\text{Al}_{1-x})_{0.47}\text{As}$ layers on InP have produced very broad DLTS spectra for a variety of Al percentages [5.12]; some states exhibit activation energies which seem dependent on Al content. Such states approximately follow the locus of the alloy mid-gap and it is concluded that traps observed in different alloy composition layers are the same deep level, originating from a dominant native defect or impurity. Trap densities increasing with increasing lattice mismatch have been reported for $\text{Ga}_x\text{In}_{1-x}\text{P}$ layers grown on InP [5.13] and $\text{In}_x\text{Ga}_{1-x}\text{As}_y\text{P}_{1-y}$ on GaAs [5.14], with the latter showing an additional increase in trap concentration as the heterojunction was approached. Trap profiling through the GaAs/ $\text{Al}_{0.25}\text{Ga}_{0.75}\text{As}$ heterojunction has been reported [5.15] using a fixed reverse bias and varying the fill bias amplitude; this revealed both bulk states and states spatially localised at the heterojunction. However, because of the use of ever-increasing voltage measurement windows, deep level spectra become distorted and require careful deconvolution to resolve individual features. Whitney *et al.* [5.16] investigated the $\text{In}_{0.53}\text{Ga}_{0.47}\text{As}/\text{InP}$ interface using Double Correlation DLTS (DDLTS) [5.17]. Whilst this technique yields information on trap distributions over a narrow region and was used to profile deep states through the heterojunction region, it still does not address the problem of multiple

trap crossing points with the Fermi level: traps at fixed distances below the conduction band will, in the vicinity of the heterojunction, cross the Fermi level at more than one point during a transient measurement. Furthermore, although the work of Whitney shows a peak in the trap concentration occurring close to the heterojunction position, the magnitude is questionable since it is approximately equivalent to the shallow doping level. No significant variation of interface trap density (as determined from integration of the DLTS data) was observed with increasing lattice mismatch. It is clear that the use of DLTS for trap profiling through a heterojunction is non-trivial, with ambiguities existing in the interpretation of such results.

Extensive work has been carried out in characterising deep defect levels in bulk Si associated with dislocations introduced by plastic deformation. DLTS studies have been carried out in both n- and p-type material and whilst results for n-type material have been more consistent, there is still a differing view on the exact nature of the dislocation-related states. On introducing a high dislocation density (typically 10^9 cm^{-2}), a complex deep level spectra is observed. Omling *et al.* [5.18] concluded that the same deep levels were observed in plastically deformed n-type Si for various different studies. Each exhibited a logarithmic capture behaviour which has been ascribed to acceptor-type states as a result of interaction between dangling bonds at the dislocation core and point defect clouds [5.19, 5.20]. This so-called logarithmic filling law is now commonly accepted to be the fingerprint of an extended defect. Kimerling *et al.* [5.21] and Kveder *et al.* [5.19] report a complex deep level spectra for n- and p-type Si, both of which simplify to a single broad peak at $E_C - 0.38\text{eV}$ and $E_V + 0.35\text{eV}$ respectively following a high temperature anneal. The change in defect spectra is considered to be due to reconstruction of dangling bonds at the dislocation core. Ono *et al.* [5.22] reports three main hole traps, all of which virtually disappear on high temperature annealing. The ideal capture behaviour suggested the states were acceptor-like and discretely distributed i.e. not interacting dislocation core states. It is proposed that the dominant state observed in the as-deformed material at $E_V + 0.33\text{eV}$ is related to

irregularities on dislocation lines, whilst the subsidiary states at $E_V+0.24\text{eV}$ and $E_V+0.56\text{eV}$ related to agglomerations of point defects; TEM results indicated the removal of such defects with high temperature anneal whilst the dislocation density remained unchanged. Thus Ono questioned the validity of the dangling bond reconstruction theory, proposing that such a mechanism would be likely to occur at temperatures lower than that observed by Kveder. As previously considered by Jaros *et al.* [2.56], such dangling bond models would produce energy bands too broad to be observed by conventional spectroscopic techniques such as DLTS. Thus, it seems most likely that the observed dislocation related levels are the result of dislocation interaction with point defect species, core reconstruction being less likely. Sidebotham [5.7] first reported deep levels associated with grown-in dislocations in n-type MBE Si. The dislocation density was much lower (10^3 to 10^5 cm^{-2}), as compared to typical densities investigated by DLTS for plastically deformed samples. A single level $E_C-0.51\text{eV}$ matched to work by Omling [5.18] and Kveder [5.19]; however, logarithmic filling behaviour was not observed for the MBE material.

It has been considered [5.18, 5.21, 2.55] that the broadening of the deep level spectra is the result of a band of energies contributing to the measured capacitance transient; in such circumstances, the transient may become non-exponential and the validity of the DLTS measurements is brought into question. This problem was first assessed by Omling *et al.* [5.23], who considered the extraction of physical properties from conventional DLTS with non-exponential transients. Assuming a gaussian distribution of energies around a fixed mean energy, deep level spectra were simulated for a variety of broadening energies; it was observed that the broadening was symmetrical about the deep level peak position (which showed no variation) and peak heights were reduced for increasing level broadening. The latter effect could lead to errors in trap concentrations as determined from the deep level peak height. The model was further extended to non-exponential transients for dislocated n-type Si [5.18] and n-type GaAs [5.24]. Das *et al.* [5.25] similarly considered a band of energies for the case of semiconductor alloys and detailed the situations of weak and strong crystal disorder.

It was concluded that standard DLTS analysis introduced negligible error except in the case of severe broadening, where E_{act} was overestimated. Broadening has also been observed in plastically deformed n- and p-type Si by Kisielowski *et al.* [5.26]. The broadening apparent in the deep level spectra was attributed to the inhomogeneous introduction of dislocations and point defects and could be described by broadening parameters which straddled the weak-to-strong disorder transition (20-30meV) as defined by Das *et al.*. This was taken to indicate substantial local distortion of the energy gap, caused by local shifts of the band edge: both fluctuations in potential energy occurring between sites of randomly distributed charged defects and the formation of split-off states or band tails associated with dislocations were considered as possible causes. Some interesting conclusions were drawn from additional information provided by Electron Spin Resonance (ESR), which was used to investigate the nature of the electrical activity with regard to defect-point defect/dislocation interactions. Point defects, with no structural relation to dislocations, dominated the electrical properties of the deformed crystals by introducing deep levels mostly in the lower half of the bandgap, whilst defects in the core of dislocations were more likely to produce mid-gap levels and levels in the upper part of the bandgap; this was determined by ESR alone. More importantly, the observed logarithmic filling behaviour was not considered to imply the location of a defect on a dislocation although it was suggested it could indicate the presence of dislocations or compensation in the crystals. This is a very interesting viewpoint and, as pointed out in the preceding paper [5.27], means that highly localised point defect distributions and dislocation-related deep states can only be distinguished by such techniques as ESR since a logarithmic capture process will be observed for both defect types. Most defects observed were amphoteric, exhibiting donor-like and acceptor-like behaviour in p- and n-type material respectively.

Thus, whilst it is considered that dislocation electrical activity is the result of decoration of the defect by impurities, the exact nature of the deep states is a complex area, reflected by the rich and varied deep level spectra often observed. Furthermore,

the validity of the so-called logarithmic filling behaviour, taken as an indicator of dislocation-related deep states, is brought into question and highlights the necessity for complimentary techniques to probe the defect structure and possibly identify the origins of such deep states.

5.3 EXPERIMENTAL RESULTS

In order to spatially profile deep level distributions, a pulse height of 1V was used for increasing reverse bias; this allowed narrow regions of the sample to be analysed independently and was found to be preferable to use of a fixed fill bias and variable reverse bias (where deconvolution of individual peaks was problematic). Deep level distributions were evaluated using the "effective voltage change" approach [5.28]: a given spatial distribution of traps will drop a calculable voltage as the traps discharge and it is this that gives rise to the capacitance transient [see section 3.2.4.3]. This effective trap distribution voltage drop is found by finding the slope to the C-V curve at the reverse bias used and dividing the capacitance transient size by this slope; this value is then used in (3.55) to calculate N_T , whilst x_1 and x_2 are found from (3.27). A fill pulse of 3ms was found sufficient to completely saturate all deep states studied. Capture measurements were carried out using a larger voltage window, employing a -2V fill pulse and -5V reverse measurement bias, in order to minimise the potential problem of trap refilling due to carrier spilling from the depletion edge into the space-charge region [5.29]. All deep level spectra presented here are for the 1000s^{-1} rate window; trap concentrations were determined from the peak height.

The Si epilayers will be considered first as they provide the benchmark to which the $\text{Si/Si}_{1-x}\text{Ge}_x/\text{Si}$ layers will be compared.

I. Si

Typical deep level spectra for sample #24/21 ($T_s = 530^\circ\text{C}$, $N_a \approx 10^{16} \text{ cm}^{-3}$) for a variety of reverse measurement biases are shown in Fig 5.1. Note the peak height does not directly reflect the trap concentration as the quiescent capacitance changes. Three

Fig 5.1 Typical deep level spectra for sample #24/21.

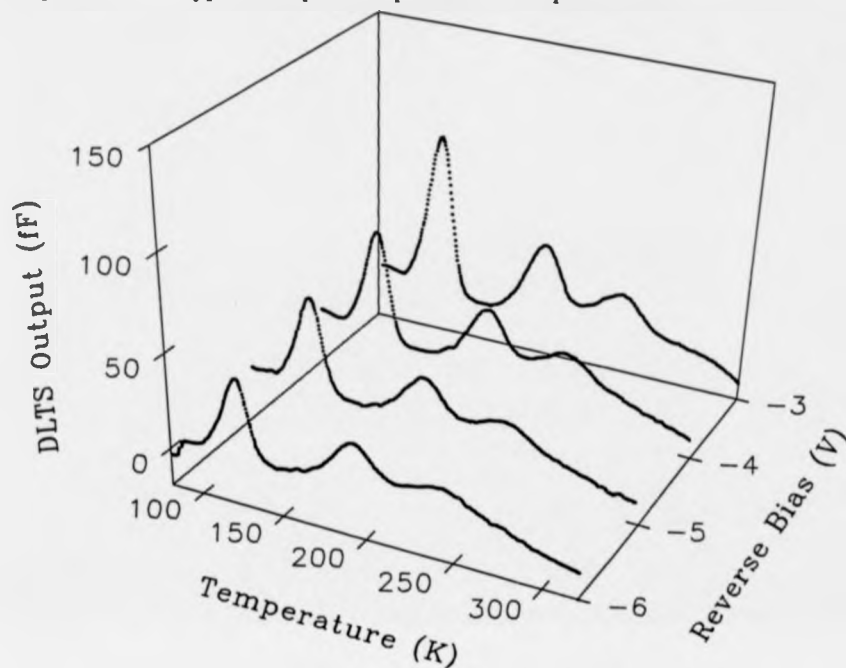
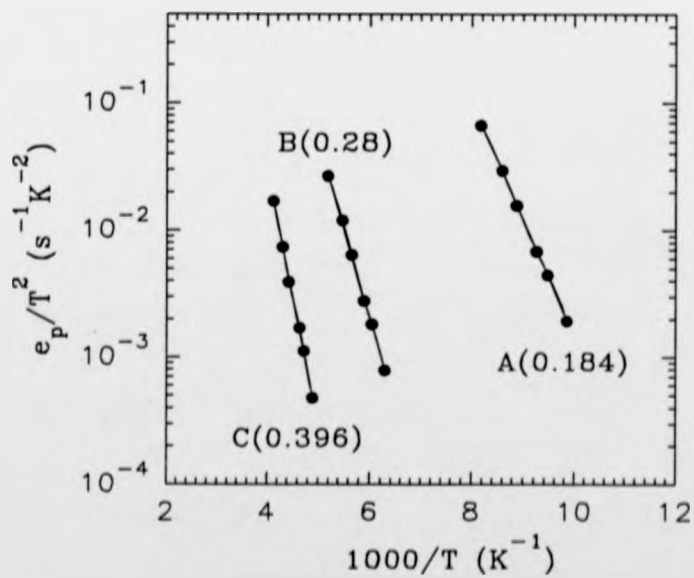


Fig 5.2 Arrhenius plot of the well defined deep level features as shown in Fig 5.1.



well defined peaks are observed and will be referred herein as A ($0.184 \pm 0.02 \text{ eV}$), B ($0.28 \pm 0.02 \text{ eV}$) and C ($0.396 \pm 0.02 \text{ eV}$). Fig 5.2 gives the Arrhenius plots of the T^2 - corrected hole emission rates, taken as the fingerprints for the three well defined hole traps. The notation A(0.184) etc. refers to the slope of these Arrhenius plots (0.184 eV in this case); the actual trap depth from the band edge can only be calculated by appropriate thermodynamic considerations (section 3.2.4.4) and taking into account the temperature dependence of the capture cross-section, which is not actually possible due to the non-ideal capture behaviour. Apparent deep level distributions as determined from the peak height are shown in Fig 5.3 which, away from the contact region, are relatively uniform, with a slight increase towards the epilayer/substrate interface. A few comments are now appropriate. Trap position determined from (3.27) gives a histogram distribution; for clarity, an average position between x_{\min} and x_{\max} for the histogram distribution has been chosen for the plots. Also, the identification of deep levels to a single trapping state, X is determined from both its activation characteristics and the position of the peak; this is of greater relevance when the Si/Si_{1-x}Ge_x/Si layers are considered in results section II.

Contrast this with the results for sample #24/17 ($T_s = 630^\circ \text{C}$, $N_a \approx 10^{16} \text{ cm}^{-3}$) which shows similar peaks A, B and C but with an apparent deep level distribution an order of magnitude lower in concentration.

The apparent deep level distribution for sample #28/20 ($T_s = 530^\circ \text{C}$, $N_a \approx 10^{16} \text{ cm}^{-3}$) are shown in Fig 5.4; whilst peaks A, B and a state herein denoted D (see results section II.) are observed, D is seen to dominate and is present in much higher apparent concentrations as compared to sample #24/21.

Capture measurements for deep states A, B and C in sample #24/21 all indicated logarithmic filling behaviour as described by (3.64) Fig 5.5 and hence no meaningful values for capture cross-section could be obtained. Note that even for small filling pulses, ideal capture behaviour according to (3.62) was not observed. A restriction placed on this latter point was the problem associated with "ringing" for reduced filling pulses and hence measurements were not possible for pulses $\leq 500 \text{ ns}$.

Fig 5.3

Apparent deep level distributions for sample #24/21.

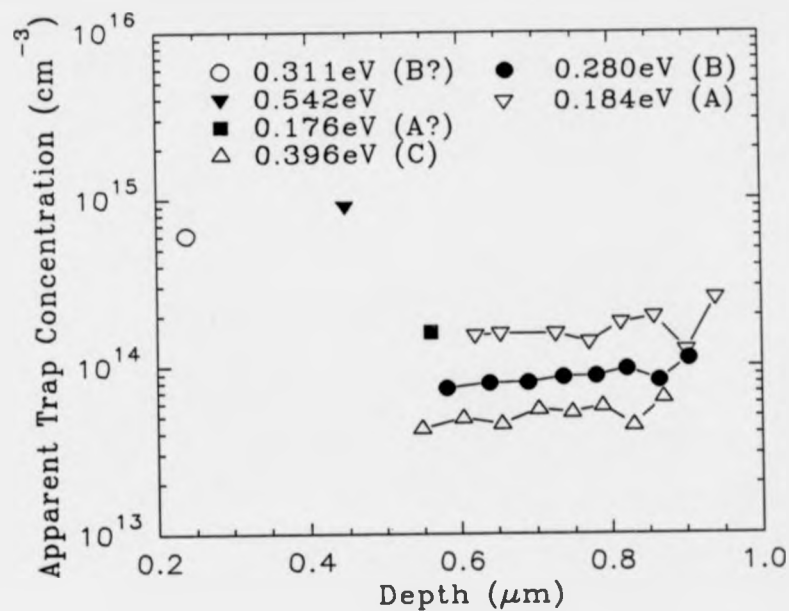


Fig 5.4

Apparent deep level distributions for sample #28/20.

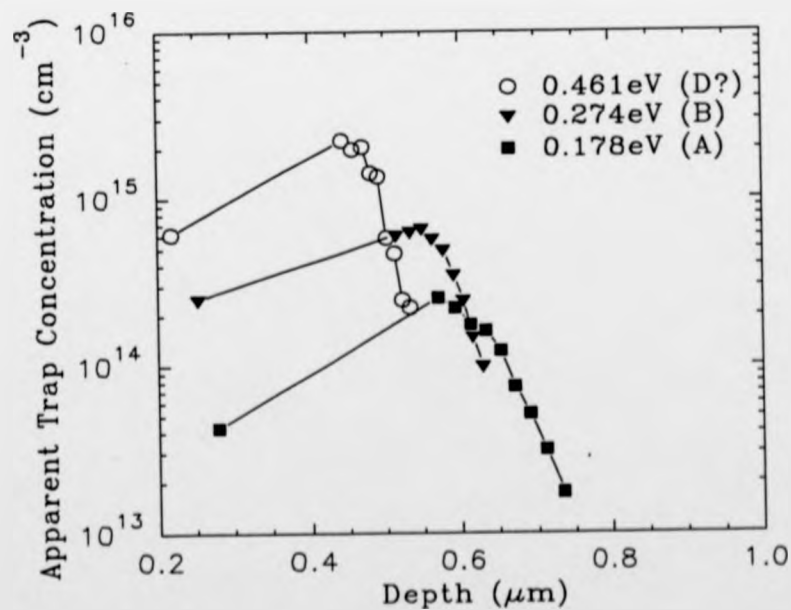


Fig 5.5 Logarithmic filling behaviour observed
for deep levels A, B and C.

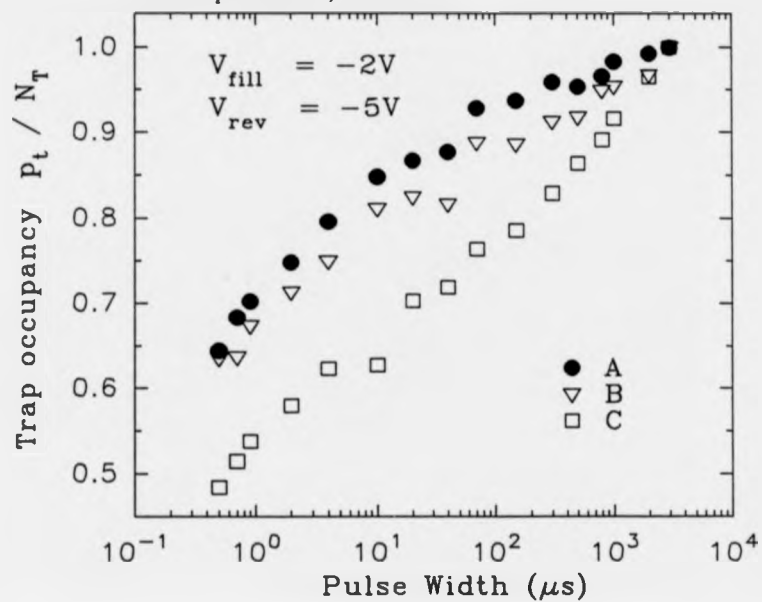
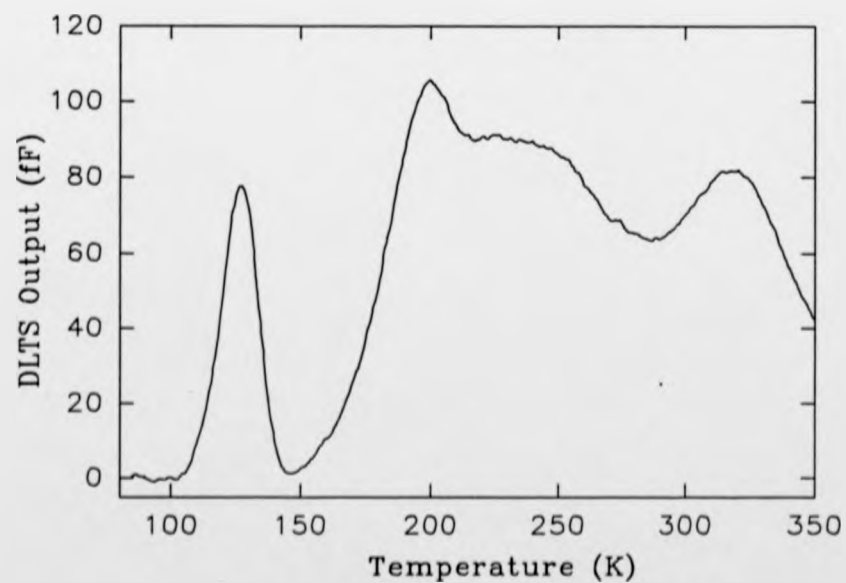


Fig 5.6 Deep level spectra for sample #24/21 following
annealing treatment (30 minutes at 630°C).



Annealing studies were also carried out to determine the stability and nature of the deep levels. As-grown material was subjected to a rigorous pre-clean before annealing took place, which involved as follows:

- (i) A degreasing procedure (successive washes in boiling Trichloroethylene, then Acetone, then Methanol) to remove surface organics;
- (ii) HF (50%) dip to remove the residual surface oxide;
- (iii) RCA1 [5.30]: a wash in a boiling Ammonia-based solution to remove organics;
- (iv) HF (50%):DI, 1:10 to remove the oxide formed during step (iii);
- (v) RCA2 [5.30]: a wash in a boiling Peroxide-based solution to remove surface metallics.

Bulk contamination would be unaffected by this pre-clean. A quartz furnace tube was purged in O_2 at $900^\circ C+$ for one week to remove any contamination; annealing then took place at reduced temperatures in an N_2 gas atmosphere. Samples were introduced in a smaller quartz tube (which had itself undergone the preclean outlined above plus O_2 purge), annealed and then withdrawn to the mouth of the furnace and allowed to cool in an N_2 /air ambient. Ti Schottky barriers were then formed, as detailed previously, to allow capacitance measurements to be made. Results for heat treating sample #24/21 for 30 minutes at $630^\circ C$ are shown in Fig 5.6. Although detailed profiling was not carried out, the important observations made were the broadening of the deep level spectra and a reduction in the apparent deep level concentration by an order of magnitude. Attempts to use Ti Schottky barriers on Si layers subjected to heat treatment for 1 hour at $830^\circ C$ failed; the devices suffered catastrophic degradation on measurement, which was irreversible. The reasons for this are unknown at present.

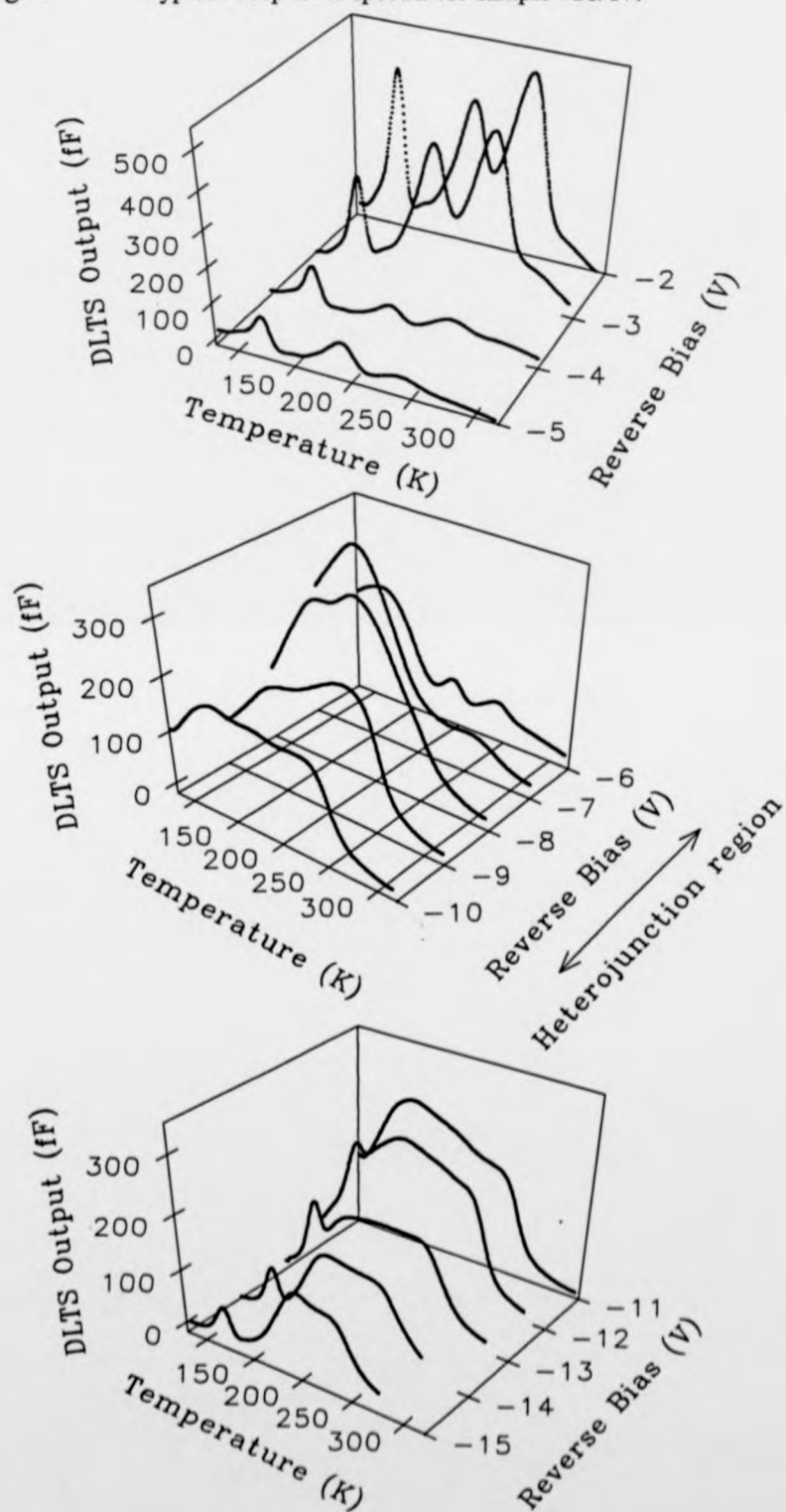
II. $Si/Si_{1-x}Ge_x/Si$

The introduction of the heterojunction, along with the $Si_{1-x}Ge_x$ alloy, is a further potential problem; despite this, some interesting trends have been observed.

Typical deep level spectra for sample #28/17 ($T_s = 530^\circ C$, $N_A \approx 10^{16} \text{ cm}^{-3}$, $x = 0.12$) are shown in Fig 5.7. Whilst well defined peaks are observed in the Si cap,

Fig 5.7

Typical deep level spectra for sample #28/17.



overlying the $\text{Si}_{0.88}\text{Ge}_{0.12}$ layer (at 0.195 ± 0.02 eV comparable to A, 0.306 ± 0.02 eV comparable to B, 0.389 ± 0.02 eV comparable to C and 0.482 ± 0.02 eV herein denoted as D), considerable distortion is observed in the deep level spectra as the depletion edge moves into the vicinity of the first heterojunction. As the depletion edge is extended into the bulk $\text{Si}_{0.88}\text{Ge}_{0.12}$ layer away from the first heterojunction, the distortion is reduced and peaks start to be resolved (the particularly well defined level at 0.185 ± 0.02 eV is comparable to A). These observations were made for all Ge compositions studied.

The broadness of the peaks in the first heterojunction region suggested either multiple trap contributions or "trap energy bands" (this is considered in the next section); this means that both apparent trap concentrations and activation energies taken from the broad peaks could be in error and should be viewed with caution. And despite the use of the narrow 1V measurement window to spatially resolve the deep states, the problem of multiple trap crossing points in the vicinity of the heterojunction still exists, causing error in the apparent trap spatial location. However, it would appear that despite the distortion that occurs in the deep level spectra in the vicinity of the first heterojunction, comparison with apparent trap distributions determined with greater accuracy in the bulk $\text{Si}_{1-x}\text{Ge}_x$, away from the first heterojunction, suggest that the apparent trap distributions in the first heterojunction region are not significantly in error. It is interesting to note that whilst the maximum reverse bias employed modulates trap distributions close to the second heterojunction, the distortion observed in the deep level spectra in the first heterojunction region is not seen.

Fig 5.8a-e illustrates the apparent trap distributions for a variety of samples. An attempt is made to identify particular traps from their activation energies and peak positions using the notation X as previously; this is relatively straightforward for the well defined peaks in the bulk regions, but the distorted spectra in the first heterojunction region means comparisons are difficult and so a large number of states in this region remain uncategorised.

Fig 5.8a Apparent deep level distributions for sample #24/19.

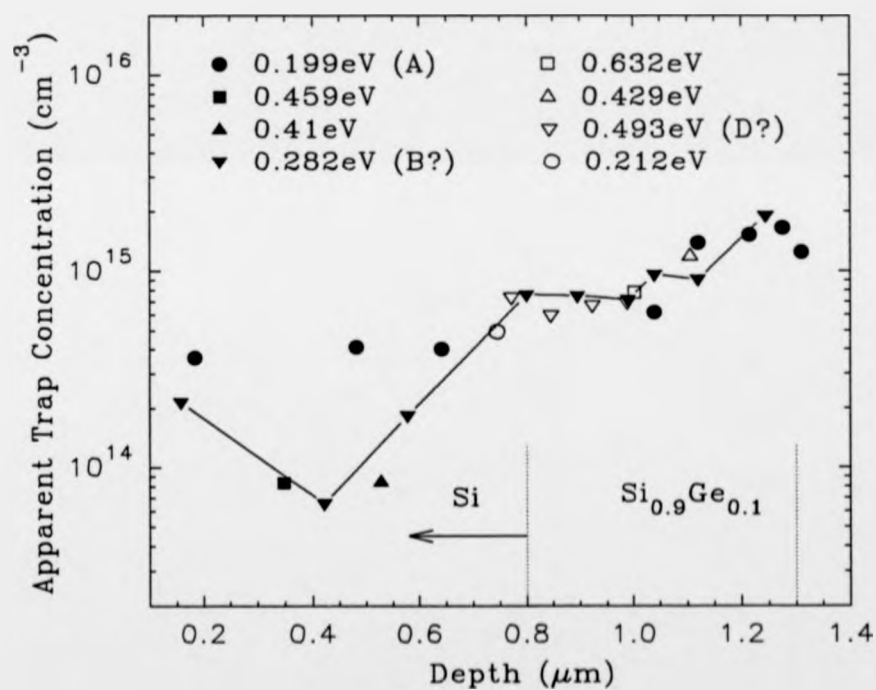


Fig 5.8b Apparent deep level distributions for sample #28/15.

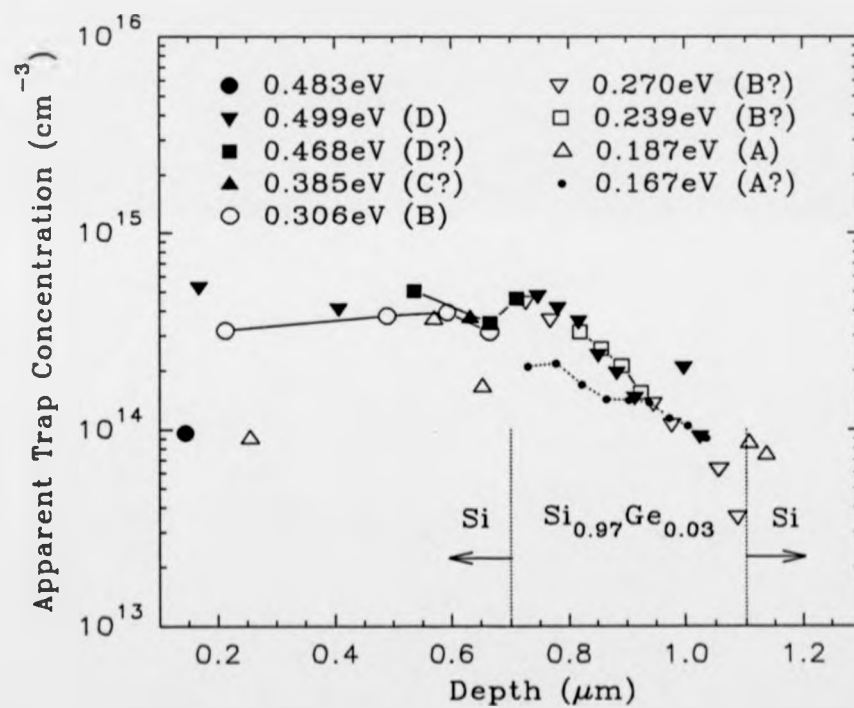


Fig 5.8c Apparent deep level distributions for sample #28/16.

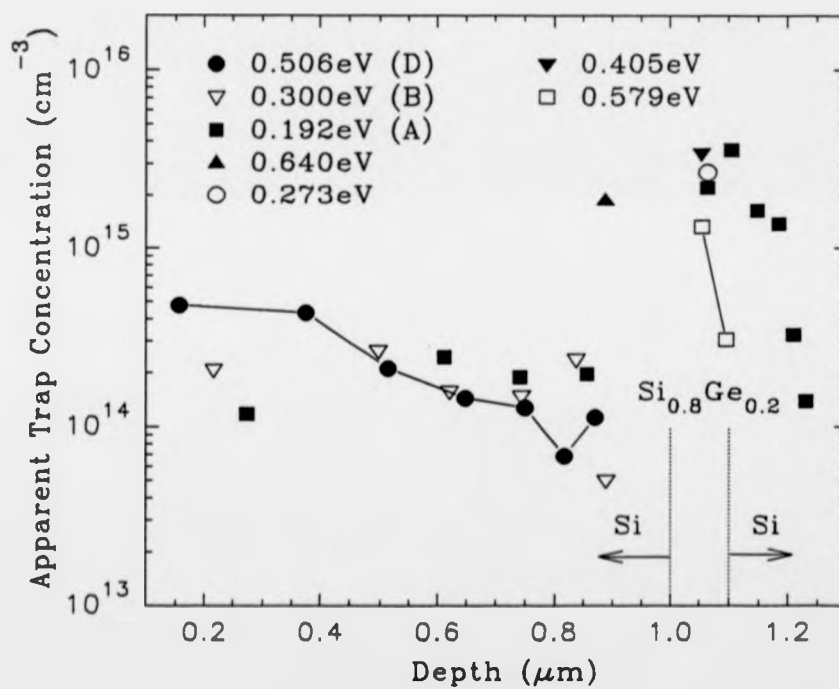


Fig 5.8d Apparent deep level distributions for sample #28/17.

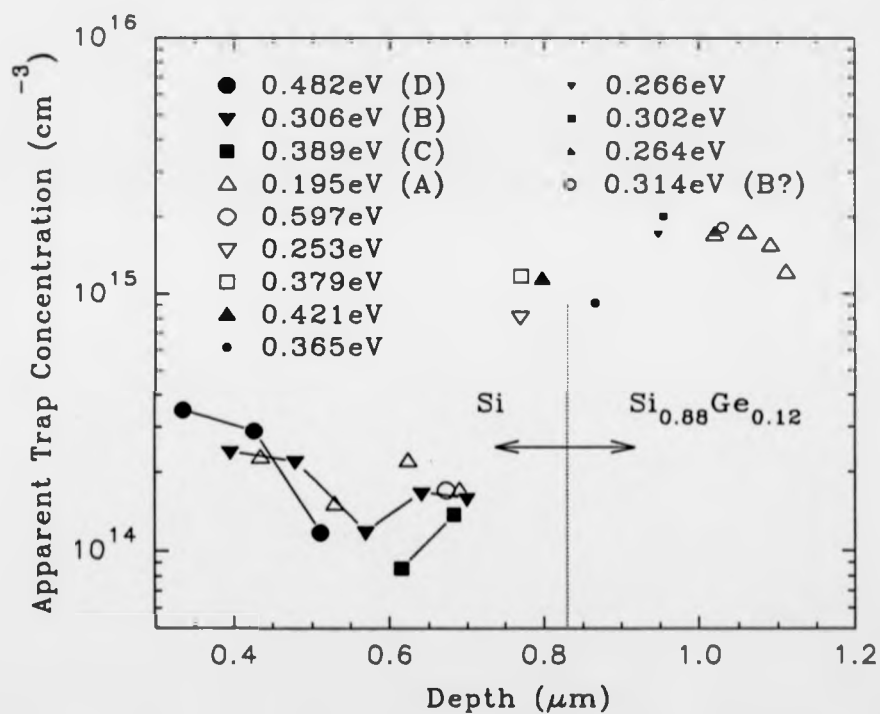
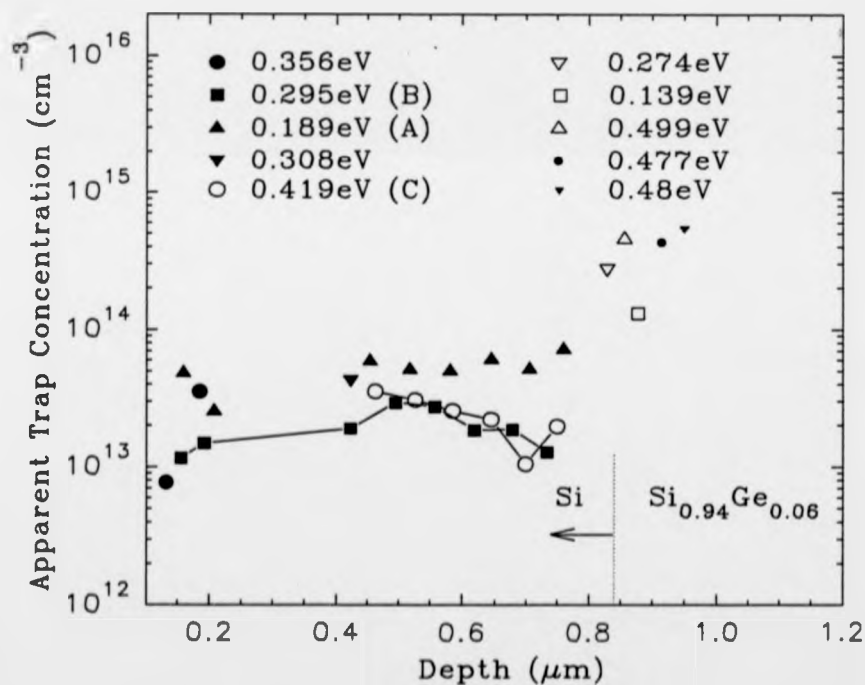


Fig 5.8e Apparent deep level distributions for sample #28/22.



- (i) Sample #24/19 Fig 5.8a ($T_s=600^\circ\text{C}$, $N_A\approx 10^{16}\text{ cm}^{-3}$, $x=0.1$) relaxed: the deep level spectra, although broadened, shows peaks which may still be resolved; the degree of distortion on profiling through the first heterojunction was less as compared to all the metastable layers. A gradual increase in deep level concentration is observed towards the second heterojunction;
- (ii) Sample #28/15 Fig 5.8b ($T_s=530^\circ\text{C}$, $N_A\approx 10^{16}\text{ cm}^{-3}$, $x=0.03$) strained: minimal distortion occurred in the deep level spectra in profiling through the first heterojunction, which showed broadened, but well defined, peaks throughout. As a consequence of this improved resolution, peaks attributed to A and B within the $\text{Si}_{0.97}\text{Ge}_{0.03}$ epilayer show reduced activation energies by 0.02-0.03eV as compared to A and B in the Si cap; it could be argued this reduction is similar to the band offset associated with the 3% Ge composition and suggests the states are pinned to the conduction band. Such an effect is also observed for D, but only in the vicinity of the first heterojunction. No evidence is seen for this in higher Ge composition alloys. Note also the fall-off in deep level concentration beyond the first heterojunction region into the bulk alloy layer;
- (iii) Sample #28/16 Fig 5.8c ($T_s=530^\circ\text{C}$, $N_A\approx 10^{16}\text{ cm}^{-3}$, $x=0.2$) strained: because the width of the $\text{Si}_{0.8}\text{Ge}_{0.2}$ layer was only $0.1\mu\text{m}$, spatial resolution of peaks in the alloy was not possible. However, the distribution shows a peak in the vicinity of the first heterojunction/alloy layer and drops off as the depletion edge is extended into the underlying Si buffer;
- (iv) Sample #28/17 Fig 5.8d ($T_s=530^\circ\text{C}$, $N_A\approx 10^{16}\text{ cm}^{-3}$, $x=0.12$) strained: the deep level distribution shows a maximum in the vicinity of the first heterojunction/alloy region; again, there is a fall-off in the deep level concentration beyond the first heterojunction towards the second heterojunction;
- (v) Sample #28/22 Fig 5.8e ($T_s=630^\circ\text{C}$, $N_A\approx 10^{16}\text{ cm}^{-3}$, $x=0.06$) strained: the apparent trap concentrations are an order of magnitude lower compared to layers grown with $T_s=530^\circ\text{C}$; this is in good agreement with the negligible change observed in the bulk free carrier concentrations from C-V measurements.

Note also that for increasing Ge percentage, the peak trap concentration in the first heterojunction/alloy region is seen to increase.

Capture measurements carried out in the Si cap for deep states A, B and D all indicated non-ideal logarithmic filling behaviour Fig 5.9 as for the uniformly doped Si

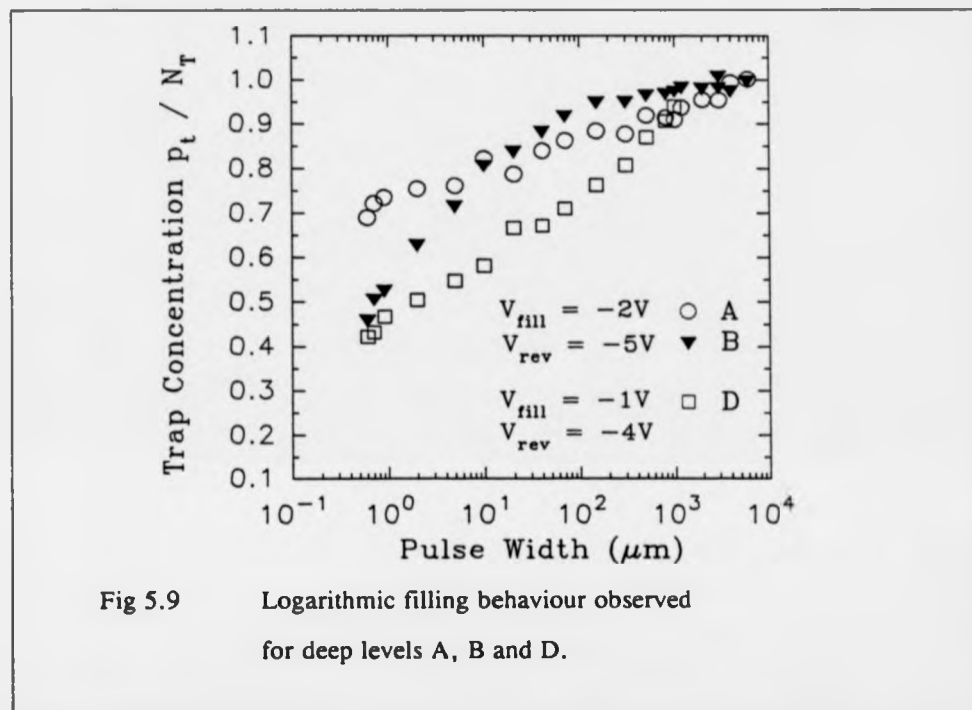


Fig 5.9 Logarithmic filling behaviour observed for deep levels A, B and D.

layers and thus no meaningful value for capture cross-section could be obtained. Furthermore, reducing the fill pulse for measurements made in the vicinity of the first heterojunction resulted in a reduction in amplitude of the broadened features; individual peaks could no longer be resolved and hence capture measurements could not be made.

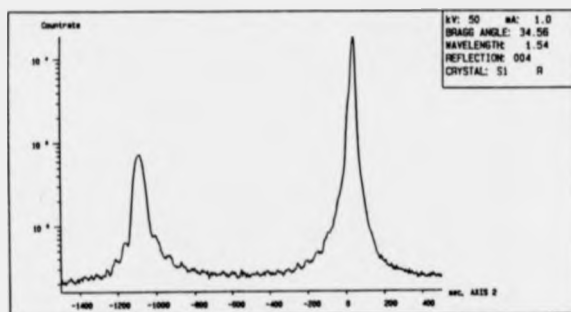
Heat treating the metastable layers caused problems with degradation of the Schottky devices and depletion capacitance measurements were not possible. The cause for this is unknown at present.

5.4 STRUCTURAL AND CHEMICAL ANALYSIS

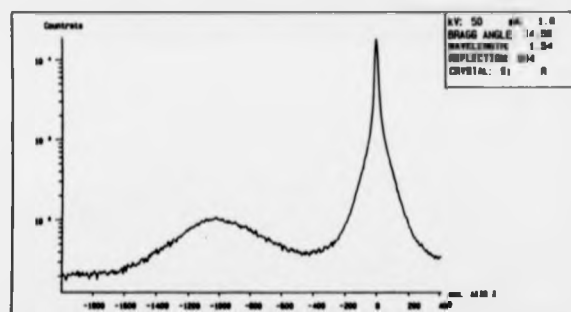
Typical double X-ray rocking curves are shown in Fig 5.10a-c for samples #28/17 (as-grown), #28/17 (heat treated 1 hour at 830°C) and #24/19 respectively.

Fig 5.10

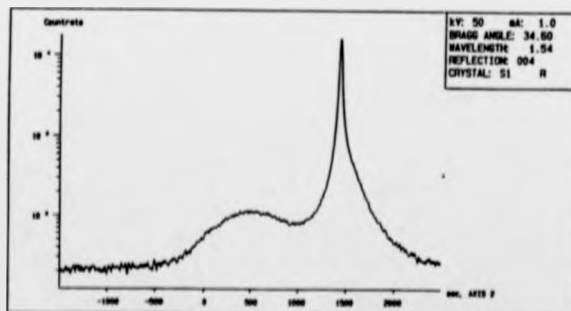
X-ray rocking curves for: a) sample #28/17 (as-grown), b) #28/17 (annealed 1 hour at 830°C) and c) sample #24/19.



a



b



c

Fig 5.10a illustrates the Bragg reflection for the, on-average, fully strained 12% alloy layer, which allowed determination of alloy thickness ($0.35\mu\text{m}$) and Ge fraction (0.114 ± 0.005), in good agreement with the layer specifications. The subsidiary peaks seen either side of the epilayer reflection arise from interference between the wave field incident on the alloy layer and the wave field reflected at the Si epilayer surface; such features are taken to indicate the high interfacial definition of the underlying heterointerface [5.31]. The displacement of the $\text{Si}_{0.88}\text{Ge}_{0.12}$ alloy reflection on heat treatment Fig 5.10b, indicates the change in lattice constant in the direction of growth due to the strain reduction within the alloy layer. The broadening of the epilayer signal in Fig 5.10b&c, with a removal of these secondary fringes, indicates a loss of interfacial integrity, due to non-uniform relaxation as misfit arrays appear.

Results of defect etching are shown in Fig 5.11. Considerable variation was observed in the defect counts; further problems were encountered regarding defect identity on etching into the $\text{Si}_{1-x}\text{Ge}_x$ alloy layers. For this reason, results presented here are for defect counts in Si (for the $\text{Si}/\text{Si}_{1-x}\text{Ge}_x/\text{Si}$ layers, etching was confined to the Si cap). Misfit densities were observed in the Si as a consequence of underlying lattice mismatch, although it is not possible to determine whether this is occurring at the upper or lower interface. Particular trends observed were:

- (i) As-grown s-pit and threading dislocation densities showed little variation with increasing Ge percentage, remaining in the low 10^4 cm^{-2} regime; for the situation of either $T_s=630^\circ\text{C}$ or subsequent annealing, s-pit densities were observed to approach 10^6 cm^{-2} whilst threading dislocation densities remained relatively unchanged.
- (ii) Misfit dislocation line densities showed little dependence on increasing Ge percentage; the densities observed still corresponded to minimal relaxation.

Typical TEM micrographs for as-grown relaxed and strained alloy layers are shown in Fig 5.12a&b respectively. Note TEM cannot detect the low threading dislocation densities as observed by the defect etch technique.

Fig 5.11 Defect counts for various samples investigated in this work.

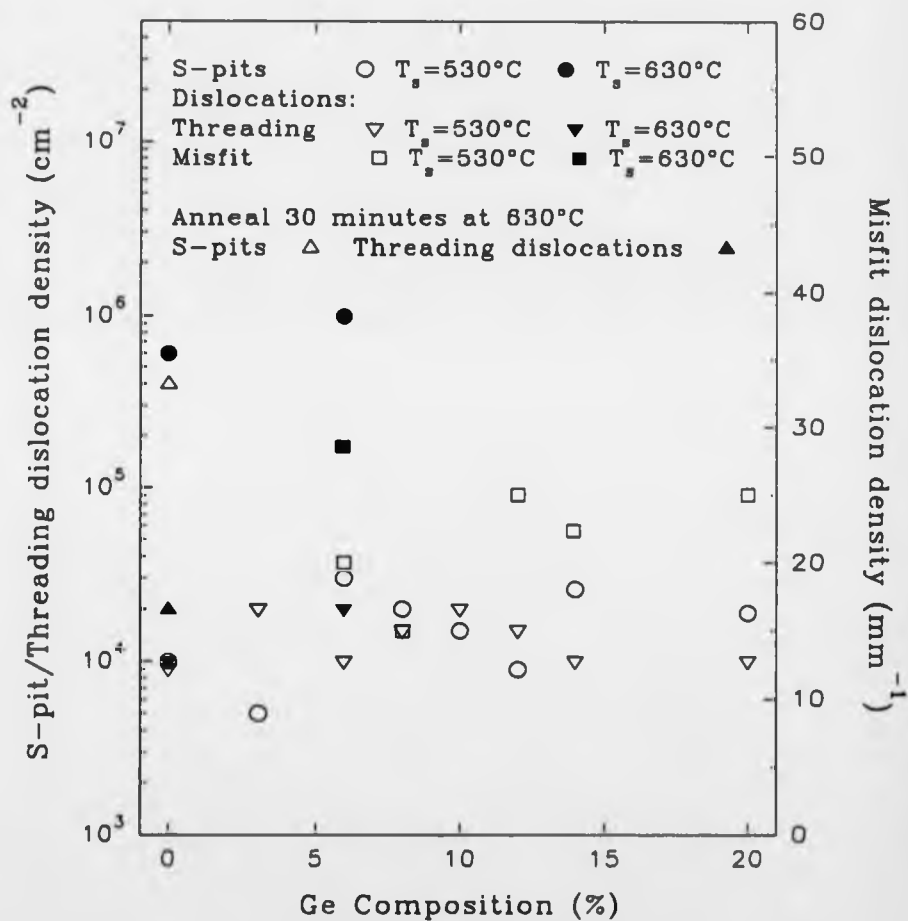
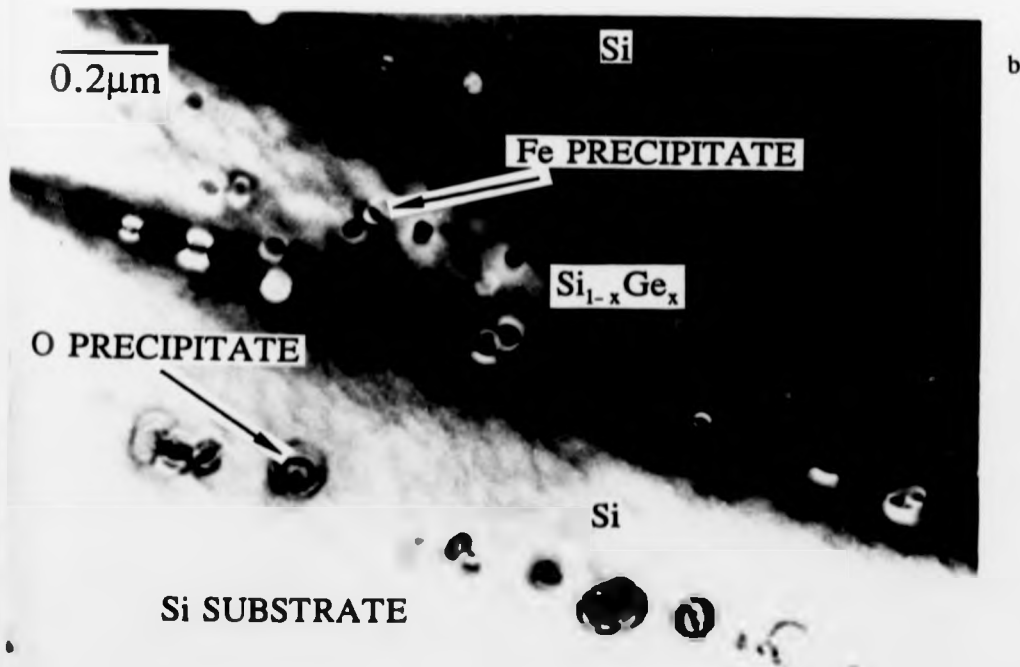
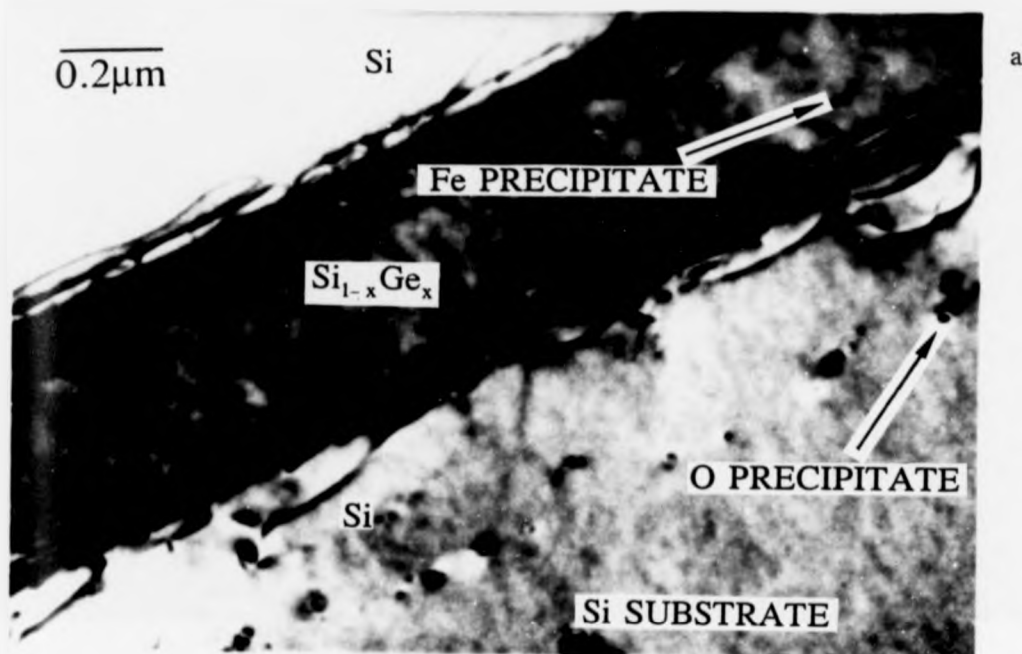


Fig 5.12 Typical TEM micrographs for: a) relaxed and
b) strained layers investigated in this work.



The relaxed sample exhibits a high misfit dislocation density along both heterointerfaces, indicative of strain relief. Of particular interest are the precipitate features observed: those at the epi/substrate interface are O-related whilst those located preferentially at the heterointerfaces and within the alloy layer alone are Fe-related precipitates - note there was also evidence of Fe precipitation on the dislocations. Not shown for this particular orientation are banding effects observed within the alloy layer, parallel to the plane of growth; similar effects observed by Fraser *et al.* [5.32] were attributed to compositional variations.

In contrast, the strained layer showed a high degree of coherency at the upper and lower heterointerfaces, no misfit dislocations being apparent. Similarly to the relaxed sample, precipitates located at the epi/substrate interface are O-related whilst those at the heterointerfaces and within the alloy layer alone are Fe-related. Evidence of alloy banding was again apparent.

5.5 DEEP LEVEL MODELLING

The DLTS rate window technique is based upon the assumption that the capacitance transient is an exponential; departures from this draw the conventional analysis of trap activations and concentrations into question. During the DLTS thermal scan, the capacitance transient was continually monitored; deviations from exponential behaviour was found for traps A, B, C and D, being most pronounced in the deeper states. This observation was even more apparent in the spectra recorded on profiling through the first heterojunction into the alloy. Furthermore, peak heights for successive rate windows 400, 200, 80, 50 and 20 s⁻¹ (required for trap activation) were observed to decrease in height; this has been attributed to trap refilling at the depletion edge [5.33]. Again, this was most pronounced in the deep level spectra obtained on profiling through the first heterojunction. Using a larger measurement window did not remove this effect of reduced peak height, suggesting that trap refilling could not alone explain this observation. For traps positioned at $x < x_0$ Fig 3.7, the capture rate during the fill pulse decreases with distance according to the carrier spilling at x_0 . The time required

to fill traps to the steady state is much longer as a consequence of this, as compared to traps situated at $x > x_0$. From the depletion approximation, $E_T = E_F$ and $c_p \approx e_p$ at x_2 (from (3.47)). The capture rate is given by (3.61):

$$\begin{aligned} p_T &= N_T [1 - \exp(-c_p t)] \\ &= N_T [1 - \exp(-e_p t)] \\ &\equiv N_T \quad \text{for } t \geq (e_p)^{-1} \end{aligned} \quad (5.1)$$

Clearly this is satisfied for $e_p = 1000\text{s}^{-1}$ and 400s^{-1} with a fill period of 3ms. However, for rate windows 200s^{-1} or less, this condition is not satisfied and incomplete trap filling is expected, resulting in diminishing peak height as observed.

Furthermore, the use of the narrow 1V measurement window may have resulted in a transient time constant made up of both emission and capture components; indeed, the increased charge in the depletion region as emission proceeds requires that the edge of the depletion region shrinks towards the Schottky barrier at the surface. Thus an empty trap may be refilled if it lies close to the shrinking depletion edge. So, in order to ascertain the effect of the small 1V measurement window on the DLTS lineshape and peak height, a "no-depletion approximation" model was considered to reproduce the true measurement conditions.

Model I.

This first model is based on the approach adopted by Sidebotham [5.7]. Consider Fig 5.13a for long filling times: for $x > x_0$, all traps may be considered filled whilst for $x < x_0$ the trap occupancy may be determined by (3.50) for $t_{\text{FILL}} \rightarrow \infty$ (in this case, $p_T(0) = 0$), the occupancy being governed by the carrier concentration due to carrier spilling at the depletion edge, x_0 . At the end of the filling phase, the diode is switched into reverse bias with the depletion edge now at x_d ; it is this time regime that this model is concerned with. It is assumed that all the shallow acceptors are ionised, with their associated free holes swept out of the depletion region; both N_A and N_T are assumed to be uniformly distributed over the 1V measurement window. The initial trap

Fig 5.13a Variation in trap occupancy for fill (V_{FILL}) and reverse (V_{REV}) applied measurement biases, where $V_{\text{FILL}} > V_{\text{REV}}$ (see section 3.2.4.2).

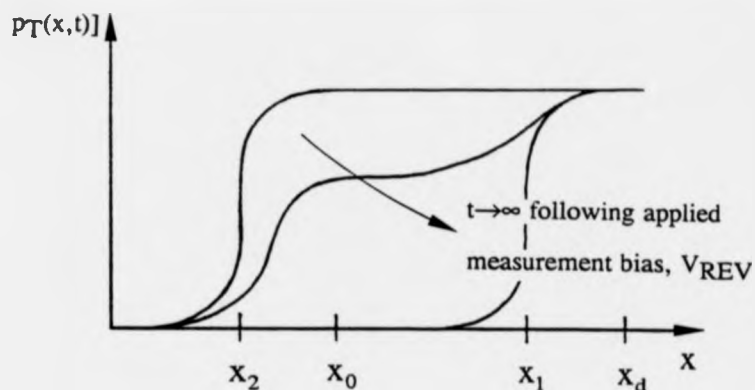
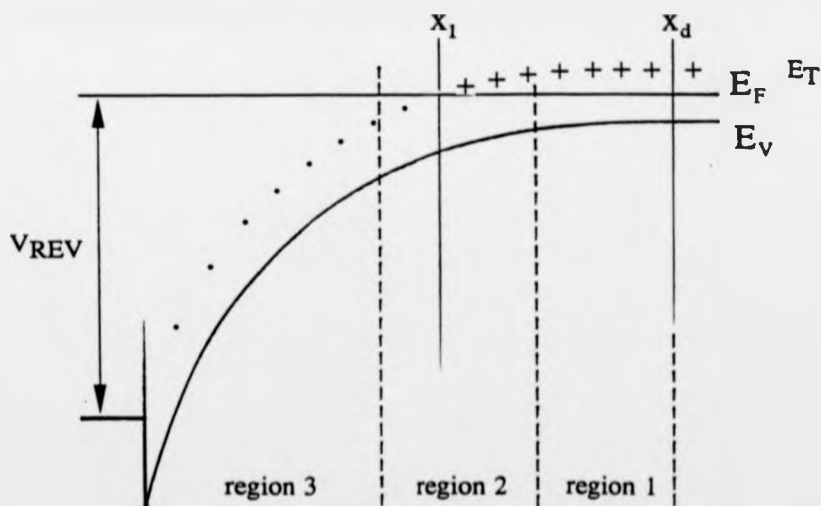


Fig 5.13b Energy band diagram according to Model I.



$$J = R$$

$$x = L$$

$$V_{x=x_d} = 0$$

$$J = 0$$

$$V(J=0) = \frac{E_T - 5kT}{q} - \frac{E_F - E_V}{q}$$

$$V(R) = V_{\text{REV}} + V_{\text{bi}} = V$$

occupancy is as previously determined. Referring now to Fig 5.13b, the depletion region may now be divided into three regions. In 1., deep states at $5kT$ or greater above the Fermi level are filled and do not emit trapped carriers during the measurement phase. In 2., states lying less than $5kT$ above the Fermi level or less than $5kT$ below the Fermi level will exhibit both emission and capture behaviour according to (3.50); the degree to which these occur depends upon both the spatial and energetic position of the deep states. In 3., states are $5kT$ or less below the Fermi level; (3.50) is still applicable but emission dominates over capture.

Consider the case for deep donor traps. At time $t=0$, the initial charge density is $N_A - N_T$ up to x_0 , with a decreasing occupancy for $x < x_0$, allowing one to define a unique value for space-charge density, $N(J)$ for each value of J . From Poissons equation:

$$-\frac{d^2V(J)}{dx^2} = \frac{N(J)}{\epsilon_0 \epsilon_r} \quad (5.2)$$

Hence the valence band potential, $V(J)$ may be found by numerical integration of the space-charge density starting at L ($J=0$) and working towards the surface until $V(J) = V_{REV} + V_{bi} = V(J=R)$ is reached (see Appendix B). This gives a value for R and since $W = x_d = L + R$, where dx is the incremental distance corresponding to an increase in J , the capacitance at $t=0$ may be calculated from:

$$C(t) = \frac{\epsilon_0 \epsilon_r}{W(t)} \quad (5.3)$$

Incrementing time by an amount dt , the new trap occupancy is given by (3.50), rewritten as:

$$N_T(J, t_2) = N_T \frac{c_p(J, t_1)}{e_p + c_p(J, t_1)} \left[1 - \exp\{-\{e_p + c_p(J, t_1)\}dt\} \right] + N_T(J, t_1) \exp[-\{e_p + c_p(J, t_1)\}dt] \quad (5.4)$$

where $t_2 = t_1 + dt$ and $N_T(J, t_2)$ and $N_T(J, t_1)$ are the concentrations of occupied traps at times t_2 and t_1 respectively. The term $c_p(J, t_1)$ reflects the reduced occupancy for the

region $x_2 < x < x_0$ through the variation in the free hole concentration, $p(J)$; this may be calculated from the corresponding potential, $V(J)$:

$$p(J) = N_v \exp\left[-\frac{qV(J)}{kT}\right] \quad (5.5)$$

This term is also used to determine the magnitude of the capture process, c_p relative to the emission process in region 2. Thus, by subtraction of the new trap occupancy from N_A , a new charge density, $N'(J)$ may be defined; Poissons law necessitates the depletion width adjusts accordingly. The new boundaries ie. $J=R'$ (where $R' < R$ for majority carrier traps considered here) are obtained by repeating the numerical integration with the new charge density and thus W , and the next $C(t)$, may be obtained. By repeating these calculations for successive time increments, a capacitance transient may be constructed. From this, the DLTS spectrum may be calculated at t_1 and t_2 as described in section 3.2.4.4. This is repeated over the required temperature range allowing the deep level spectra to be obtained. For the purposes of extracting the deep level concentration, (3.55) was used.

Typical results for DLTS simulations matched to experimental data for sample #28/17 (-1/-2V measurement window) are shown in Fig 5.14, assuming a uniform distribution of donor traps at concentrations corresponding to the apparent trap concentration, as determined from the peak heights for levels A, B and D. Several important points are of note:

- (i) Despite the use of the small measurement window, the extracted trap concentrations were not underestimated for this model of discrete trap levels;
- (ii) Although there was evidence of non-exponential behaviour with the simulated capacitance transients, it was only slight and suggested the source of this effect lay elsewhere;
- (iii) The lineshapes for the simulated discrete trapping levels were noticeably narrower as compared to the experimental data.

These latter two points indicated that the possible cause for the non-exponential capacitance transients was related to trap energy bands; this initiated work on the second model.

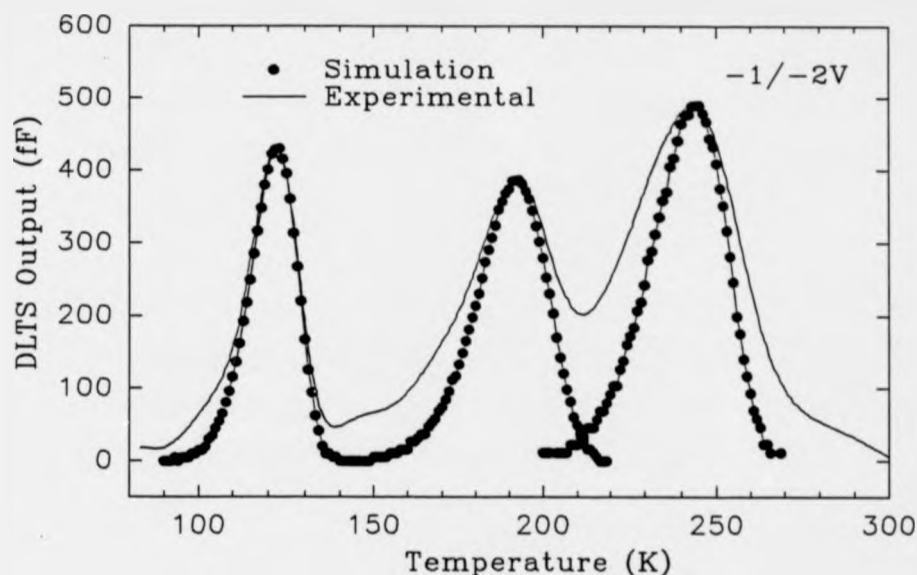


Fig 5.14 Simulations matched to experimental data for the well defined peaks in the Si capping layer for the Si/Si_{0.88}Ge_{0.12}/Si sample.

Model II.

Work by Morgan [5.34] considered that fluctuations in potential energy occurring between different sites of deep impurity centres produced identical fluctuations in the energies of the highly localised states associated with these centres. If the local potential at a point depended upon the configuration of ions around that point then it was considered that the probability, $P(E)dE$ of finding the local electronic potential energy within a range dE about E was given by the sum of the probabilities of all ionic configurations generating a potential energy in that range. The probability density function, $P(E)$ was considered to be a Gaussian distribution; this second model is based on the work of Omling *et al.* [5.23], who considered a modified form of (3.54)

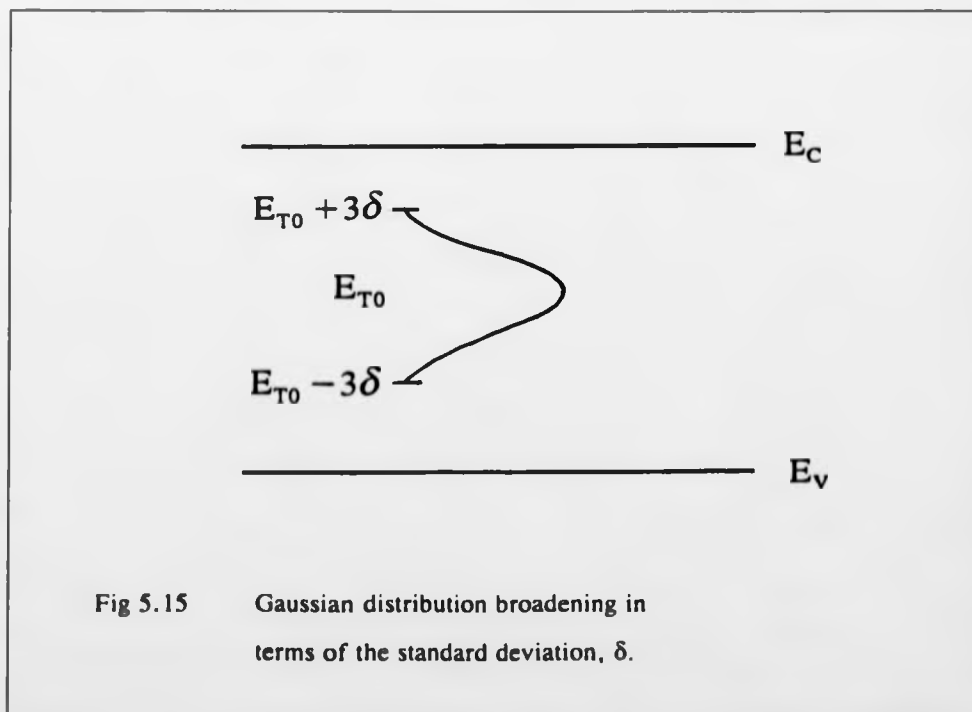
for broadened deep levels such that the time dependence of the capacitance was given by:

$$C(t) = \int_0^{\infty} P(E_T) C_0 \exp[-e_p(E_T)t] dE_T \quad (5.6)$$

Thus the ideal exponential dependence of the capacitance transient for a single energy deep state is weighted by the distribution function, $P(E_T)$, assumed to be a Gaussian distribution function centred around a mean energy, E_{T0} such that:

$$P(E_T) = \frac{1}{\sqrt{(2\pi)\delta}} \exp\left[-\frac{(E_T - E_{T0})^2}{2\delta^2}\right] \quad (5.7)$$

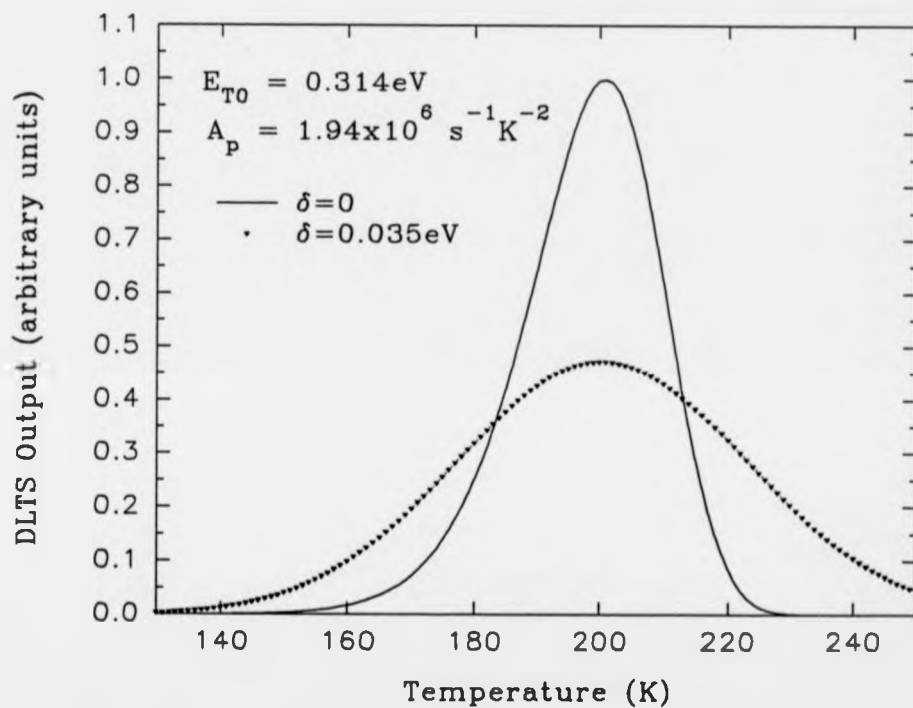
The parameter δ defines the standard deviation of the distribution and it is through this that the degree of level broadening may be considered. This is clearly illustrated in Fig 5.15: depending upon the choice of δ , the extent to which contributions for $E > E_{T0}$ and $E < E_{T0}$ are significant will be determined by the relative magnitude of δ compared to E_{T0} .



The weighting function is evaluated by calculating the magnitude of $P(E_T)$ for each E_T across the Gaussian distribution (see Appendix B). For each weighting function, the corresponding value of E_T gives a value for e_p (from (3.48)); this allows the exponential term of (5.6) to be determined, for each t and for all E_T , as defined by $P(E_T)$. As for model I., repeating these calculations for successive time increments allows the associated capacitance transient to be constructed and the DLTS spectrum follows from the boxcar technique, sampling at times t_1 and t_2 over the desired range of temperatures. Since the total area under the distribution is equal to unity, judicious choice of δ will produce $P(E_T)$ weighted deep level spectra as shown in Fig 5.16. The case of $\delta=0$ illustrates the characteristic narrow deep level lineshape for carrier emission from a single energy level, E_{T0} with the peak maximum determining the trap concentration. Evidence of energy bands around a mean energy, E_{T0} will be observed by an increase in the peak width and a reduction in the peak height. Although the latter case involves a value for $\delta>0$, the same trap concentration is assumed in both cases. Hence, by normalising the peak height for simulations with $\delta>0$ to that for $\delta=0$, the degree of error in determining trap concentrations may be found by matching simulations to the experimental data.

Fig 5.17 shows the simulated match to experimental data for sample #28/17 (-1/-2V measurement window) whilst Table 5.1 shows the broadening parameters used to match to the experimental data plus the trap concentration correction factors determined for the deep levels A, B and D. It should be realised that the process of matching simulation to experimental data is an iterative one and, similar to the C-V simulation profiles, can be very time consuming; for this reason, no attempt is made to provide corrected trap distributions or broadening parameters for all the samples investigated in this work. Sample #28/17 is chosen as a typical example to illustrate the applicability of the model.

Fig 5.16 Weighted deep level spectral broadening
according to the choice of the parameter, δ .



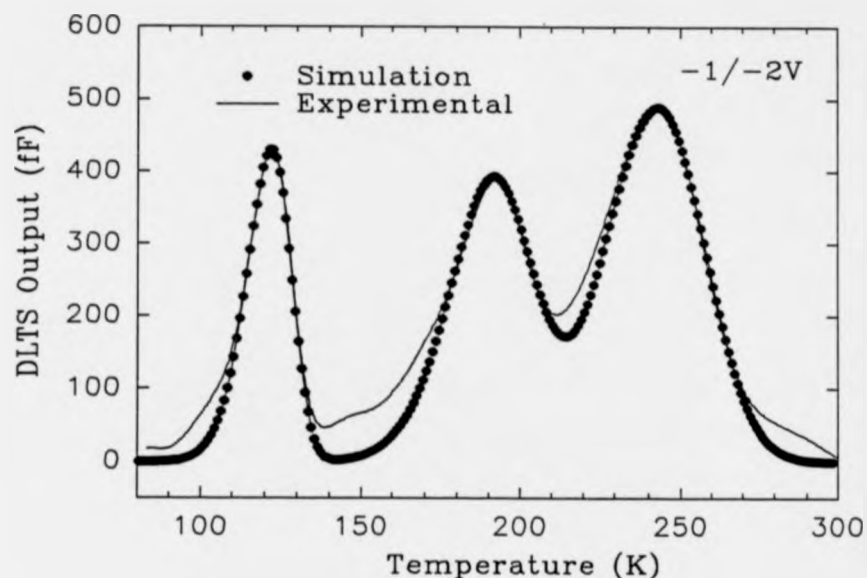


Fig 5.17 Simulated match to the well defined peaks in the Si capping layer of the Si/Si_{0.88}Ge_{0.12}/Si sample.

Table 5.1 Extracted broadening parameters for the matching of simulations from model II. to sample #28/17 (-1/-2V measurement window).

Trap Identity	E_T (eV)	δ (eV)	N_T Correction
A	0.193	0.0042	1.07
B	0.297	0.0134	1.27
D	0.482	0.0233	1.44

Broadening parameters are readily extracted for the well defined peaks A, B, C and D; however, the gross distortion that occurs to the deep level spectra in the vicinity of the heterojunction cannot realistically be discussed in terms of broadening of a single energy level associated with a deep state since isolated peaks are no longer well defined.

Initially, the distorted deep level spectra was compared to the simulations used to match to peaks A, B and D. Consider Fig 5.18a, showing the broad deep level spectra in the vicinity of the heterojunction (-11/-12V measurement window). Whilst A and the trailing edge of D can apparently be identified by the simulations, the mid-temperature range peak shows no correlation to the simulation for B. Consider now Fig 5.18b, which is identical to Fig 5.18a except that the broad activated peak at $E_T=0.302\text{eV}$ is compared to a simulation with $\delta=0.05\text{eV}$. It becomes clear that whilst the simulations can be used to reconstruct the deep level spectra for the well defined peaks, any number of trap activations and their associated spectra could be used to reconstruct the experimental data for broadened features. In doing so, large apparent values of δ , associated with very broad single peaks, could be extracted, which should be viewed with caution. Extracted values for the band broadening parameter and trap concentration correction factors are given in Table 5.2 for the well defined peaks in sample #28/17. Because the distortion occurs in the vicinity of the heterojunction, it is possible that the associated band bending accompanying the valence band offset, along with any significant build-up of coulombic potential at trapping states, may obscure the true deep level features as observed in the bulk Si and $\text{Si}_{1-x}\text{Ge}_x$ regions. These points will be discussed in the next section.

Whatever, the model provides an explanation for the experimentally observed departure from exponential dependence of the capacitance transients and, more importantly, allows both an estimation of the broadening of the deep states along with a correction for the true trap concentrations. Applying the correction factors in the well defined bulk regions, the true trap concentration is in better agreement with the degree of compensation observed in the bulk apparent free carrier distributions as determined by C-V measurements (see Fig 4.6), assuming the deep levels to be donor-like in nature

Fig 5.18a Matching to the distorted spectra close to the first Si/Si_{0.88}Ge_{0.12} heterointerface with simulations used to match to the well defined deep levels A, B and D (as in Fig 5.17).

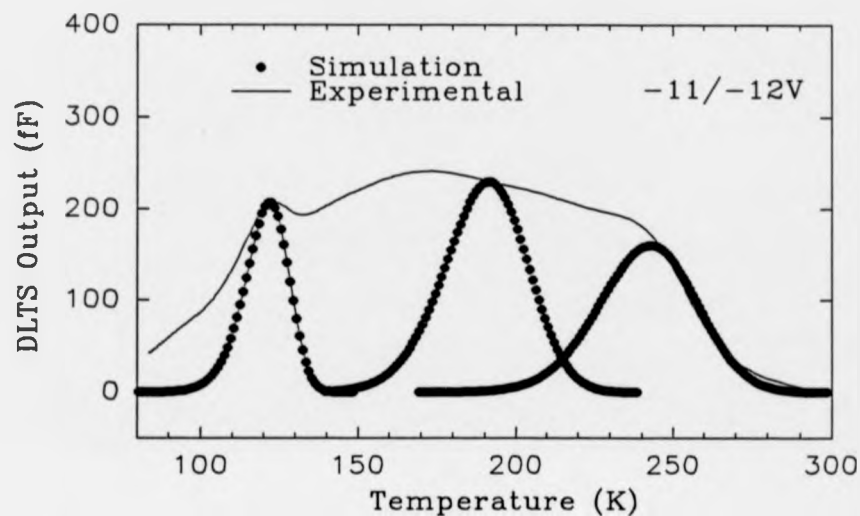


Fig 5.18b Simulated match to the broad deep level feature (from Fig 5.18a).

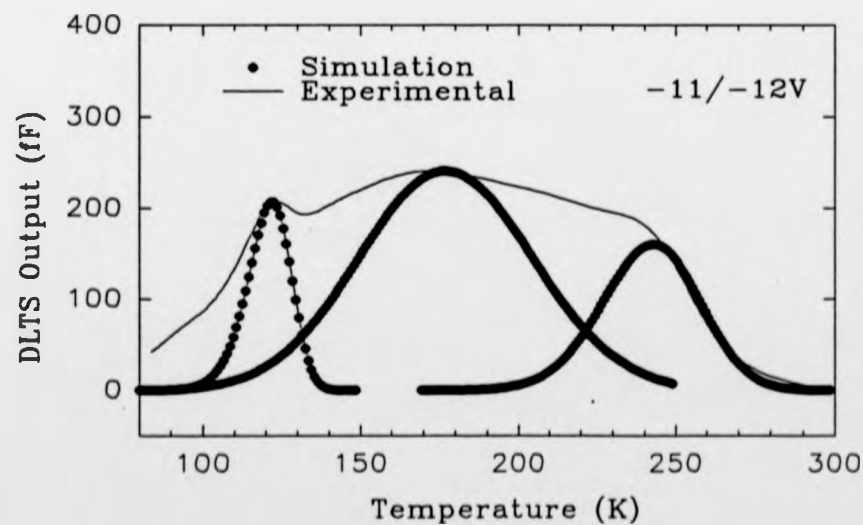


Table 5.2 Extracted broadening parameters for the matching of simulations
from model II to the well defined deep level peaks in sample #28/17.

Measurement Window (V)	Broadening Parameter, δ (eV)		Trap concentration correction factor, K_N
-2/-3	A: $\delta=0.004$ $K_N=1.07$	B: $\delta=0.013$ $K_N=1.27$	D: $\delta=0.023$ $K_N=1.44$
-3/-4	A: $\delta=0.004$ $K_N=1.07$	B: $\delta=0.007$ $K_N=1.08$	D: $\delta=0.02$ $K_N=1.35$
-4/-5	A: $\delta=0.004$ $K_N=1.07$	B: $\delta=0.01$ $K_N=1.16$	C: $\delta=0.021$ $K_N=1.39$
-5/-6		B: $\delta=0.01$ $K_N=1.16$	C: $\delta=0.021$ $K_N=1.39$
-11/-12	A: $\delta=0.004$ $K_N=1.07$		D(?): As for D (-2/-3V)
-12/-13	A: $\delta=0.004$ $K_N=1.07$		
-13/-14	A: $\delta=0.004$ $K_N=1.07$	B(?): $\delta=0.038$ $K_N=2.37$	
-14/-15	A: $\delta=0.004$ $K_N=1.07$	B(?): $\delta=0.035$ $K_N=2.12$	

5.6 DISCUSSION

The C-V simulations used to reconstruct the free carrier profiles in Chapter 4 assumed that the bulk trap distributions were compensating centres ie. donor-like traps. Considerable evidence now exists to verify this.

The Poole-Frenkel effect [5.35] results in a lowering of the coulombic potential barrier around a deep state, following the application of a large E-field; for this phenomena to occur, the trap must be neutral when filled and charged when empty ie. an acceptor trap. Measurements on the well defined peaks A, B, C and D for increasing field (fixed fill bias, increased reverse bias) indicated no significant temperature shift of the peaks and no reduction in activation energy as would be expected for such an effect. This showed the states to be donor-like in nature.

Capture measurements on peaks A, B, C and D indicated logarithmic capture behaviour; this has been considered due to the build-up of a Coulomb potential as the traps fill, so inhibiting further capture of carriers. Such behaviour has long been attributed to dislocation states and, more recently, to localised compensation regions due to inhomogeneous point defect distributions; in both cases, the model shows the states to be positively charged when full and neutral when empty ie. donor-like (for p-type material).

The following discussions of the donor-like deep states are based on analysis assuming the build-up of a coulomb potential, compensation of the free hole carriers and broadening of the deep level spectra (as observed by DLTS). Similar observations and assumptions have been used, almost exclusively, to assess deep level behaviour associated with point defect/dislocation interactions. From the electrical measurements made in this work, it is difficult to distinguish between states associated with point defects alone and states arising from point defect/dislocation interactions, assuming they both exhibit similar characteristics as proposed in [5.26].

It is suggested that the origins of the electrical activity will lie with both point defects (from the structural and electrical observations, discussed later, for the high T_s and annealed samples) and dislocations (from their gettering nature). It is probable there will be some form of interaction between the two, with dislocations drawing point defects into well defined arrays along the length of the dislocation; indirect evidence for this is based on the observations made by TEM, for the relaxed sample, where Fe precipitates decorating misfit dislocations have been identified. This indicates that the solubility limit for Fe has been exceeded on segments of the dislocation; it is most likely that Fe point defects surround these precipitates and, if considered to decorate the dislocations, could give rise to the observed electrical activity. Similar effects may be considered to occur for the 60° threading dislocation components, which lie in $\langle 011 \rangle$ and $\langle 101 \rangle$ directions through the Si and $\text{Si/Si}_{1-x}\text{Ge}_x/\text{Si}$ epilayers, since it is these which may give rise to the observed states A, B, C and D.

As mentioned previously (see section 2.5 and 5.2), the associated interaction between trapped charge on dislocation-related states should result in a broadening of deep state energy levels. Use of the deep level simulations developed in the previous section allowed the degree of broadening of the well defined peaks to be assessed. Whilst a reasonable match has been achieved, it is apparent that leading and trailing edges do not always match completely; this may be a consequence of the assumption of a Gaussian distribution to describe the band broadening and a better match obtained if an asymmetric energy distribution used. Alternatively, smaller, unresolved features may be present, so producing shoulders on the main peaks.

The work of Morgan [5.34] and Stern [5.36] allowed a relation between the broadening parameter, δ and the Debye screening length, L_D to be made:

$$\delta = \sqrt{\left(\frac{q^2}{\epsilon_s \epsilon_r} \left[\frac{(N_A^- + N_D^+) L_D}{8\pi} \right] \right)} \quad (5.8)$$

where N_A^- and N_D^+ are the number of ionised acceptors and donors respectively. In

compensated material, the Debye length may be defined as:

$$L_D = \sqrt{\left(\frac{\epsilon_0 \epsilon_r kT}{q^2 (N_A - N_D)} \right)} \quad (5.9)$$

Note this is simply re-writing (3.24) replacing N_A by $N_A - N_D$; L_D represents the distance over which free carriers will redistribute themselves in the vicinity of the localised compensated region. Thus the ionisation of the donor traps and subsequent compensation allow the associated degree of level broadening to be determined.

Consider sample #28/17: only states B, C and D can cause the observed compensation (from C-V profiling) in the Si cap since from consideration of their respective emission rates as a function of temperature, C and D will freeze out at approximately 190K whilst B will freeze out at approximately 140K (A is only affected for temperatures $\leq 100K$; no significant compensation may be attributed to this particular transition). This seems reasonable since it is only B, C and D which show significant level broadening and may be considered the dominant features. From the maximum observed decrease in apparent free carrier concentration between 200K and 100K, it was estimated that B, C and D were present in approximately equal concentrations at $5 \times 10^{14} \text{ cm}^{-3}$. Table 5.3 shows the calculated values of δ for B, C and D, along with typical values taken from the $\text{Si}_{0.88}\text{Ge}_{0.12}$ alloy region according to the degree of compensation associated with these trap concentrations; a comparison to relaxed sample #24/19 and previously reported values are also given (calculated and extracted from experimental deep level spectra according to a similar approach adopted for model II.).

It is clear that the calculated broadening attributed to B (0.005eV), C and D (0.006eV) and deep states observed in the bulk $\text{Si}_{1-x}\text{Ge}_x$ epilayers, according to the localised compensation, only contribute in part to the total broadening determined via simulations; this discrepancy was also found by Kisielowski *et al.* ([5.26] Table 5.3) for much higher degrees of compensation. It was proposed that local strain (due to the presence of the dislocations) introduced states split-off from the band edges and these could additionally contribute to the overall broadening observed. The work of Ossipyan

Table 5.3 Characterisation of deep level lineshape broadening
for differing degrees of disorder in Si and $\text{Si}_{1-x}\text{Ge}_x$.

Material	δ (calculated) (eV)	δ (from simulation) (eV)	Reference
Sample #28/17 Si epilayer	0.005-0.006	0.01-0.023	This work
Sample #28/17 $\text{Si}_{0.88}\text{Ge}_{0.12}$ epilayer	≤ 0.0025	0.035-0.038	This work
Sample #24/19 $\text{Si}_{0.9}\text{Ge}_{0.1}$ epilayer		0.02-0.03	This work
Deformed FZ Si		0.016-0.022	[5.18]
Deformed FZ Si	≤ 0.01	0.02-0.03	[5.26]
Grain boundary		0.023-0.027	[5.26] & [5.37]
a-Si:H		0.175	[5.25]

[5.38] indicated a variety of dislocation-related energy bands could exist, depending upon the location of trapped charge (coulombic interaction resulting in energy band broadening or split off states) and the local defect environment. However, such split-off states would already form a part of the energy band scheme as considered in model II, ie. providing a contribution to the capacitance transient as non-interacting emitting centres over a range of energies as defined by the Gaussian distribution. The overall concentration of deep states is defined by the area under the Gaussian distribution and would encompass the split-off states; this determines the degree of compensation (assuming all deep states to be donor-like in nature) and is in reasonable agreement with the C-V measurements. Hence, the origins of the discrepancy between the broadening determined from (5.8) and the Gaussian distribution of energy states used in model II, is probably to be found in the different assumptions made in the use and interpretation of the work by Morgan: explicit details on the derivation of (5.8) by Stern are vague whilst (5.6) ignores a variation of the capture cross-section. Thus, further investigations are required on this matter; certainly temperature dependency of the capture cross-section cannot be determined at present since capture cross-section is undefined due to the logarithmic filling behaviour observed.

From Table 5.3, the value of δ is seen to systematically increase with increasing disorder, from as-grown to plastically deformed to amorphous Si. States in the Si capping epilayer studied here straddle the weak-to-strong disorder category [5.25] and may be attributed to the relatively low dislocation/high crystalline quality of the material. Contrast this to the underlying $\text{Si}_{0.88}\text{Ge}_{0.12}$ epilayer which shows an increase in broadening parameter for the dominant deep states. Assuming the layers to be in a metastable state such that the threading dislocation density is comparable to that observed in the Si cap, the additional broadening may be attributed to growth disorder. TEM results indicated banding, which may represent alloy compositional fluctuations; this would produce a modulation of the band edges which could affect the transient capacitance measurements (as will be discussed next for the heterojunction region). The additional presence of the metallic precipitates, located preferentially within the alloy

layer, could produce potential wells [5.39] and act as deep donor states within the p-type material, similar to the proposed dislocation-related deep levels. Such states could contribute to the observed broadening of the deep level spectra since carrier emission would occur over a range of apparent energies.

The distortion observed in the deep level spectra, in the vicinity of the first heterojunction, probably arises as a consequence of the significant band bending which occurs in this region. The band bending may cause carrier emission, from a single energy level, to occur at more than one spatial location and combined with different apparent energetic displacements from the valence band edge, could broaden the deep level features. Note the deep level occupancy may also be affected (see section 2.5). Three possible sources for the band bending will now be considered.

Increasing fixed interface charge density, with increasing Ge percentage, could produce progressively larger degrees of band bending; note this contribution is both bias and, approximately, temperature independent and will not be observed by DLTS. Making a similar assumption to that made in Chapter 4, the sheet charge density extracted from the heterojunction region is converted to a volume trap density. Thus, a sheet density $5 \times 10^{10} \text{ cm}^{-2}$ distributed over an $0.01 \mu\text{m}$ region becomes $5 \times 10^{16} \text{ cm}^{-3}$; at 300K this can produce a band-bending of 0.044eV whilst at 80K the band-bending is reduced to 0.013 eV. These values are significant when compared to the heterojunction band-offset. It is interesting to note that negligible band bending will occur assuming depletion of the uniformly doped layers due to the presence of a sheet of charge; this may be found using the formula for a parallel plate capacitor:

$$q\Delta V = \frac{\sigma d}{2\epsilon_0\epsilon_r} \quad (5.10)$$

σ being the sheet charge density and d the total depletion which will occur (where $d = \sigma/N_A$). From the maximum determined interface charge density $\sigma_I \cong 5 \times 10^{10} \text{ cm}^{-2}$ and $d = 0.25 \text{ nm}$, this gives a total band bending of $qV \cong 0.00023 \text{ eV}$. If the charge were

to reside wholly as a sheet distribution at the heterointerface, such a dipole would have a negligible effect on the band edge.

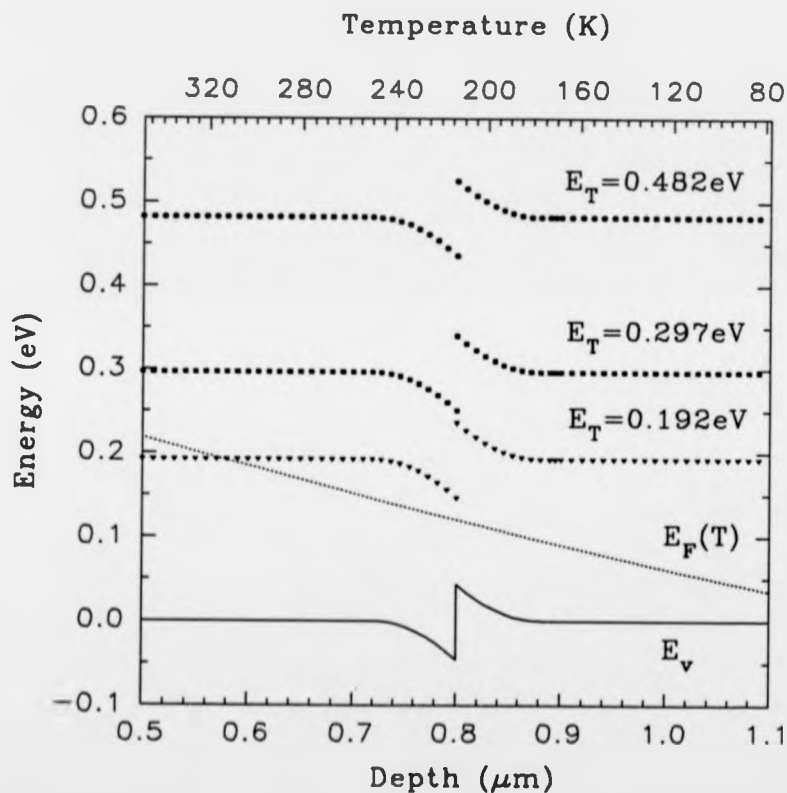
For a band offset of 0.089eV (12% Ge alloy), the associated band bending would extend approximately 0.1 μ m either side of the heterojunction. This is illustrated in Fig 5.19 in the absence of an applied bias and also shows the relative positions of deep states A, B and D, assumed at fixed energies relative to the valence band. The variation of the Fermi level as a function of temperature is given for clarity. Deep states, which have filled under the conditions shown in Fig 5.19, could cross the Fermi level at more than one point in the heterojunction region, on applying the reverse measurement bias, and depending upon their depth relative to the band edge, so provide extra contributions to the transient capacitance and hence broaden the deep level spectra. Indeed, the ambiguity of the apparent trap depth in the vicinity of the heterojunction is self evident: deep states close to the heterojunction on the Si side, emitting carriers to the valence band on the Si_{0.88}Ge_{0.12} side, are shallower in energy. Additionally, if narrow energy bands are present in the heterojunction region (not illustrated in Fig 5.19) and subject to the band bending, fractional occupancy of the bands could occur producing asymmetric deep level features.

The band bending attributed to the coulomb potential build-up at the dislocation-related states may also be significant. As considered in section 2.5, the capture of holes creates a localised positive charge and the associated band bending, $q\Phi$ increases to a saturation value as progressively more states are filled. Thus, the band bending is a function of fill time; this is observed as the logarithmic capture behaviour shown in Fig 5.5 and Fig 5.9 and described by (3.64). Rewriting (3.63) gives:

$$q\Phi(t_F) = kT \ln \left[\left(\frac{N_T - p_T}{p_T} \right) \sigma_p \langle v_{th} \rangle p t_F \right] + kT \ln \left[\frac{p_T}{t_F \left(\frac{dp_T}{dt_F} \right)} \right] \quad (5.11)$$

With the corrected trap concentrations and using the capture cross-section determined via the intercept method from the DLTS activation plots, the band bending as a function

Fig 5.19 Band bending associated with a valence band discontinuity of 0.089eV. The relative energetic displacements for levels A, B and D from the valence band edge are also shown.

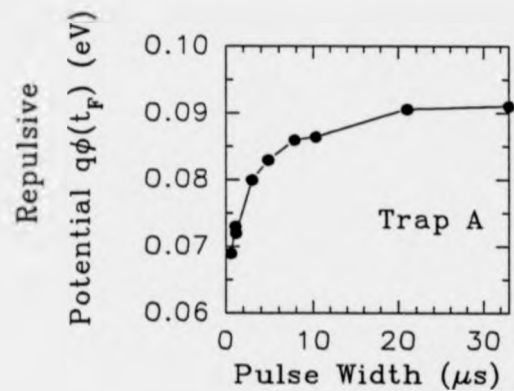


of filling time may be evaluated; this is shown in Fig 5.20a-c for deep states A, B and D respectively. It is observed that the repulsive potential becomes progressively larger for deeper traps and causes significant distortion to the band structure. Additionally, the charging of deeper states may cause variable occupancy of shallower states which are moved close to or below the Fermi level. Consider the coulomb potential associated with the filling of state D alone: a value of L_D is given by (5.9) and this allows the line charge, Q to be estimated from (2.3) since $q\Phi$ may be estimated for long filling times from Fig 5.20c. From (2.2), this gives $R \equiv 0.13\mu\text{m}$ (assuming a well defined space-charge cylinder); this is illustrated in Fig 5.21, where the band bending is associated with the filling of deep state D alone. If deep states A and B are present, then their energetic positions relative to the Fermi level will be lowered and it is clear that in this situation, neither A or B would ever act as trapping centres and, as a consequence, would not be observed by DLTS. However, both states A and B are observed by DLTS and this suggests that the different states are necessarily spatially isolated from each other. It is unlikely that point defects alone, at a concentration of $5 \times 10^{14} \text{ cm}^{-3}$, could cause the significant band bending, as suggested by the build-up of such a coulomb potential; this further strengthens the argument for the electrical activity being point defect/dislocation related. Hence, it is probable that the well defined peaks are associated with different types of defect/impurity interaction with dislocations in the epilayers, such that particular electrical activity will vary depending upon the local defect environment surrounding the dislocation. Note that distortion to the deep level spectra is less likely for such dislocation states in the bulk epilayers since the dislocations are threading up towards the surface and the associated band bending, although still present, does not have such a pronounced effect as it would if it were parallel to the extending depletion edge (as would be the case for misfit dislocations, parallel to the heterointerface; this assumes the observations made for dislocations in the bulk are directly applicable to dislocations at the heterojunction).

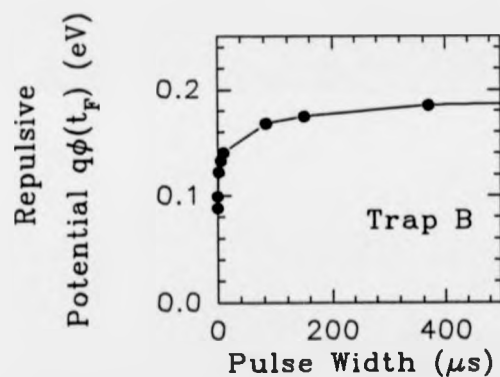
Thus a combination of dislocations and interface charge with the heterojunction band offset would cause complex distortion to the band structure in the vicinity of the

Fig 5.20

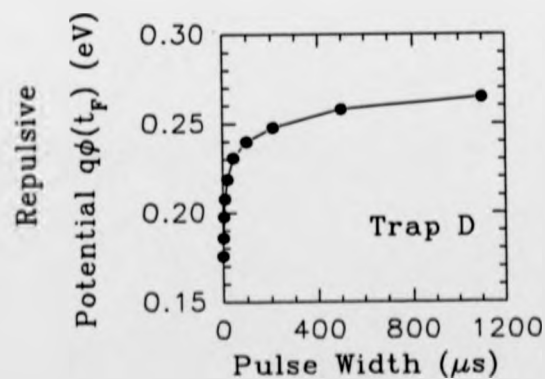
Saturated values of the repulsive coulomb potential determined experimentally for states: a) A, b) B and c) D.



a

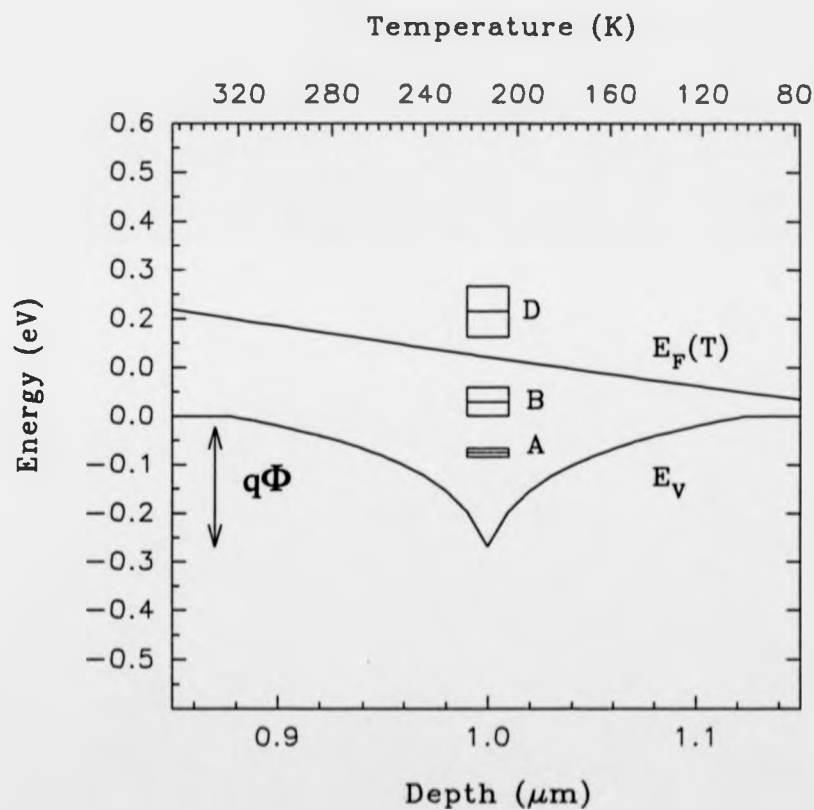


b



c

Fig 5.21 Band bending associated with the repulsive coulomb potential due to the increase in positive charge on state D (from Fig 5.20c).



heterojunction. Since the layers are in a metastable state, the degree to which local relaxation occurs will determine the extent of the distortion in the deep level spectra, assuming a corresponding increase in dislocation-related electrical activity. Neither TEM or X-ray diffraction measurements would detect misfit arrays where misfit spacing was $\geq 5\mu\text{m}$, and thus would be insensitive to such localised relaxation. In contrast, defect etching indicated misfit arrays were present, although it was observed that the misfit length was relatively short. This suggests that even if misfit dislocations were present at the heterointerface and accompanied by electrically active states, their effect would be reduced, since it was observed that the regions of relaxation were dispersed, and hence would not contribute significantly to distortion of the bands. It is also possible that if the average spacing between occupied trapping sites were larger for misfit segments, the build-up of a high line charge would be limited, so reducing the extent of the band bending associated with the coulomb potential as free carriers were trapped. Thus, it may be argued that the main cause of band bending in the heterojunction region should be attributed to the band offset and associated interface charge density. The spatial extent of the band bending corresponds closely to the spatial distortion in the deep level spectra observed for various Ge compositions; for the 3% Ge alloy, the distortion was reduced, reflecting the much smaller band offset and minimal band bending. For the relaxed sample #24/19, the reduced distortion on profiling through the first heterojunction suggests the increased mismatch has partially or completely removed the band offset associated with a coherently strained structure and fairly well defined deep level features are observed. Note the deep level spectra for this sample will be further complicated by the increased dislocation density.

Deep level profiling Fig 5.8a-e revealed uniform, low 10^{14} cm^{-3} apparent trap distributions in the Si epilayers (with the exception of sample #28/20) and Si cap of all metastable $\text{Si/Si}_{1-x}\text{Ge}_x/\text{Si}$ structures. At the first heterojunction, a step up was observed in the apparent trap concentration, the magnitude of which depended upon the Ge composition of the alloy layer: almost non-existent for 3% Ge whilst an order of

magnitude larger for 20% Ge. The clear trend was increasing Ge percentage produced an increase in trap concentration in the alloy; in some situations, the trap concentration was observed to fall towards the second heterojunction position. Incorrect lattice incorporation of the Ge adatoms in the growing epilayer, due to departures from 2D growth or Ge clustering, could produce non-crystalline regions within the alloy; the localised strain fields associated with such regions could getter impurities and point defects, in a similar manner to that considered for dislocations. Thus, the electrical activity would increase with increasing disorder ie. increasing Ge percentage, as is observed. It should be further noted that the source of the Fe contamination has been identified with the Ge charge; the higher Ge content layers may also have resulted in higher grown-in Fe contamination, further contributing to the electrical activity. The distortion observed in the first heterojunction region is not seen as the profiling is extended towards the second heterojunction and this also corresponds to a decrease in the trap concentration, indicating the top-most heterojunction to be the dominant electrically active region. Several effects may be occurring to cause this:

- (i) The onset of relaxation is to be expected at the first strained layer/Si buffer interface; the band offset is likely to be changed as a consequence of this and hence less distortion may be expected in the deep level spectra as the profiling technique is extended towards this region. This interpretation is verified by the much reduced peak and trough feature as observed by C-V profiling at the second heterojunction. From Fig 5.21, it is clear that significant band bending will occur in the vicinity of a charged dislocation-related state; making the assumption in (i) that the lower heterointerface has a higher degree of mismatch, the reason for minimal distortion in the deep level spectra may lie with the reduced spatial extent of the band bending, due to restrictions in the build-up of charge on such dislocation-related states and as a consequence of carrier spilling into the space-charge cylinder;
- (ii) Despite this onset of localised relaxation at the lower interface, the upper heterojunction maintains its coherency and the band-offset is still significant enough to cause the distortion observed in the deep level spectra;

(iii) The strain field at the upper coherent heterointerface may produce a more effective gettering region as compared to the dislocation array at the lower interface and hence the electrical activity show a maximum in the vicinity of the first heterojunction. However, the random distribution of precipitates, from TEM, indicate there is no preferential gettering of impurities to the upper heterointerface. Furthermore, the apparent compositional variations throughout the whole of the alloy layer does not reflect the observed electrical activity focused on the upper heterojunction region.

Defect/impurity interactions giving rise to deep states in MBE material may differ from those observed in material grown by different techniques or subject to different preparation and thus care should be taken in positive identification of the source of the electrical activity as determined from previous reports. However, restricting the possible sources to those defects/impurities already identified (O and Fe (from TEM), dislocations (from defect etching, TEM) and possible contamination from Cu diffusion through the charge liners), comparisons can be made and are shown in Table 5.4. Whilst this by no means provides a comprehensive review, it is clear that similarities exist and each source could be considered to contribute to the overall electrical activity observed. Note that considerable differences may exist between calculated and measured capture cross-sections since the former can be in error. Also, the comparison of states A, B, C and D, particularly to those attributed to O and the 3d transition metals in isolated point defect form, is not strictly correct since these reported states do not involve interactions with dislocations, as is considered in this work.

Based on the observed reduction in trap concentrations by an order of magnitude and apparently unchanged dislocation density following annealing of sample #24/21, the decrease in electrical activity is attributed to the removal of point defect species from the immediate dislocation environment into electrically inactive sites. An identical effect is observed on comparison of layers (both Si and Si/Si_{1-x}Ge_x/Si) grown at 530°C and 630°C - the higher growth temperature epilayers show an order of magnitude reduction in their deep level concentrations. Sidebotham [5.7] observed an identical

Table 5.4 Deep Level Parameters for states A, B, C and D compared to previously reported deep levels observed in Si. Capture cross section is either evaluated from the intercept (I) method or using a reduced fill pulse (F) (i, interstitial; s, substitutional; d, dislocation; p, precipitation).

Association	Activation Energy (eV)	Prefactor, A ($s^{-1} K^{-2}$)	Capture cross-section (cm^{-2})	Level type	Reference
A	$E_v + 0.195$	5.77×10^6	2.62×10^{-15} (I)	Donor	This work
B	$E_v + 0.306$	2.56×10^6	1.16×10^{-15} (I)	"	"
C	$E_v + 0.389$	2.48×10^6	1.13×10^{-15} (I)	"	"
D	$E_v + 0.482$	1.47×10^8	6.68×10^{-14} (I)	"	"
Fe(i)	$E_v + 0.425$	1×10^6	?	"	[5.40]
Fe(i)	$E_v + 0.44$?	"	[5.41, 5.42]
Fe	$E_v + 0.3$?, 1.4×10^{-15} (?)		[5.41, 5.43]
Cu	$E_v + 0.233$		0.14×10^{-13} (F), 6.1×10^{-13} (?)	Donor, ?	[5.44, 5.43]
	$E_v + 0.31$		1.2×10^{-16} (?)		[5.43]
	$E_v + 0.425$		7.4×10^{-15} (F)	Acceptor	[5.44]
O (p)	$E_v + 0.2-0.5$?	Acceptor (?)	[5.45]
O (s)	$E_c - 0.15$?	Donor	[5.46, 5.47]
Misfit (d)	$E_v + 0.51$		6×10^{-13} (?)		[5.11]
60° threading	$E_v + 0.38$		5×10^{-14} (?), 5×10^{-16} (F)		[5.11, 5.48]
(d)					
Deformation induced defects	$E_v + 0.21$	4×10^6	?	Donor	[5.26]
	$E_v + 0.29$?	"	
	$E_v + 0.33$?	"	
	$E_v + 0.39$?	"	
	$E_v + 0.49$?	"	

effect and attributed it to a change in incorporation of metal impurities for growth temperatures above 600°C due to the interaction between surface segregated impurities and step flow growth processes. RHEED was not used to monitor the growing epilayers and hence the growth mechanisms for these layers was not determined; however, the observation that s-pit density increased in the layers either annealed or grown above 600°C indicated a possible transition had occurred, with metals incorporated as point defects below, and as precipitates above, this temperature. Significant diffusion would be expected for both Fe and Cu present in the MBE layers at the elevated temperatures of growth [5.49]; this usually proceeds via an interstitialcy mechanism. On the termination of growth and the subsequent cooling of the epilayer, the interstitial atoms may be considered to become supersaturated since the extrapolated solubilities of both Fe and Cu are negligible at room temperature [5.49]. As DLTS measurements are carried out at or below room temperature, observation of electrical activity associated with these interstitial states can only occur if the diffusion coefficients of the metals are sufficiently low at room temperature to prevent further migration (note diffusion coefficients, unlike solubilities, do not vanish at room temperature). Because Cu has the largest diffusion coefficient in Si, its interstitial form is unstable and is more likely to diffuse and form precipitates; as a consequence, deep levels attributed to Cu have required rapid cooling (on diffusion of the metal into Si) in order to quench the Cu atoms onto interstitial sites [5.44], or have been an investigation into the electrical activity associated with precipitation [5.43]. Since post-growth cooling of the epilayers is a radiative process and is relatively slow, any Cu present is unlikely to remain on an interstitial site and, considering the efficiency with which dislocations and associated strain fields have been observed to getter metallic species, it is more likely to form precipitates preferentially in these regions. Although Fe precipitates have been observed via TEM, no evidence exists for Cu precipitates being present and it is concluded that Cu does not contribute to the observed electrical activity. In contrast, Fe, with its lower diffusion coefficient, is more likely to form an electrically active state in a stable interstitial form [5.41, 5.42]; whilst Fe precipitation will occur in localised regions

when its solubility is exceeded, a high proportion is expected to remain in solution and could give rise to the electrical activity observed. Indeed, deep states associated with Fe precipitation have also been reported [5.43]; however, the relative contributions of Fe in point defect form or as a precipitate to the electrical activity observed here is, at present, not clearly defined.

The obvious improvements in the use of charge liners preventing metallic contamination were discussed in Chapter 4; assuming minimal metallic indiffusion from the Cu hearth, the Fe contamination is considered to originate from the elemental Ge source material. Reductions in such contamination should follow with the use of higher purity Ge. Note, however, it is not clear, from the present work, whether use of graphite liners over Si liners is any more beneficial and requires further investigation.

TEM indicated O precipitates to be present at the Si buffer/Si substrate interface. O clusters have been observed to form in high interstitial O concentration Si wafers subjected to low anneal temperatures ($\approx 650^\circ\text{C}$) of typical duration 15-100 hours [5.50]; however, this extends well beyond typical thermal budgets experienced by the MBE layers (maximum 3 hours at approximately 530°C) studied here. And whilst high grown-in O concentrations are present in the bulk MBE material (10^{17} - 10^{18} cm^{-3} [5.51]), it is more likely that the source of the contamination lies at the Si substrate/Si buffer interface as a result of ineffective substrate preclean before growth commenced. These precipitates are located exclusively at this interface and, as such, do not appear to have provided nucleation sites for dislocations [5.50]; since they are far from the regions investigated, they are not considered to contribute to the observed electrical activity. Of greater importance is the possibility that the O present in the bulk epilayers will change from its normal interstitial lattice location to a substitutional location and thus become electrically active, producing a donor state [5.46, 5.47]. Since the optimum temperature for such O-related donor states is $\approx 450^\circ\text{C}$, it is quite possible such states will form during the growth of the epilayers. Higher temperature anneals remove the electrically active deep states attributed to O [5.52] and may be considered due to the O changing from a point defect into an electrically inactive precipitate form; such a

transition could also explain the decrease in electrical activity observed for the MBE layers subjected to growth/annealing $\geq 630^{\circ}\text{C}$. Hence O point defects could also contribute to the electrical activity thus far attributed to metallic point defect interaction with dislocations.

CONCLUSION

Electrically active deep states within Si and $\text{Si/Si}_{1-x}\text{Ge}_x/\text{Si}$ epilayers have been investigated for a variety of growth/anneal temperatures and Ge percentages. Whilst well defined features are observed in the bulk material, distortion is observed to the deep level spectra in the vicinity of the first heterojunction; this has been attributed to the band bending associated with the valence band offset and associated interface charge. The well defined deep level features show broadening effects which have been discussed in terms of energy bands formed as a result of trapped charge interaction on dislocation-related states. The extent of the broadening is evaluated using simulations based on a Gaussian distribution of energy band states. It is considered that all deep level features observed are probably related to the degree of decoration of dislocations by Fe and O point defects. An increase in deep level concentration is observed in the alloy layer which is seen to increase further for higher Ge compositions; this is attributed to the increasing disorder and the possible higher grown-in Fe content associated with higher Ge compositions, and also the tendency of the alloy layer to act as a sink for impurity species.

REFERENCES

- 5.1 A. R. Peaker, E. C. Sidebotham, B. Hamilton and M. Pawlik
Proc. 2nd Int. Symp. on Si MBE (Electrochem. Soc., New Jersey 1988) 392
- 5.2 Y. H. Xie, Y. Y. Wu and K. L. Wang Appl. Phys. Lett 48 (1986) 287
- 5.3 A. Sandhu, B. Hamilton, A. R. Peaker, R. A. A. Kubiak,
W. Y. Leong and E. H. C. Parker
Proc. 1st Int. Symp on Si MBE (Electrochem. Soc., New Jersey 1985) 78
- 5.4 E. C. Sidebotham, A. R. Peaker, B. Hamilton, M. Hopkinson, R. Houghton,
G. Patel, T. E. Whall and E. H. C. Parker
Proc. 2nd Int. Symp. on Si MBE (Electrochem. Soc., New Jersey 1988) 360
- 5.5 D. J. Gravesteijn, G. F. A. Van de Walle,
A. Pruijboom and A. A. Van Gorkum Mat. Res. Soc. Proc. 220 (1991) 3
- 5.6 Y. Ota Thin Sol. Films 106 (1983) 1
- 5.7 E. C. Sidebotham PhD. Thesis (UMIST) 1990
- 5.8 V. Nagesh, H. G. Grimmeiss, E. -L. Hellqvist,
K. L. Ljutovich and A. S. Ljutovich Semicond. Sci. and Technol. 5 (1990) 566
- 5.9 V. Nagesh, E. -L. Hellqvist, H. G. Grimmeiss,
K. L. Ljutovich and A. S. Ljutovich Sol. State. Comm. 75 (1990) 151
- 5.10 J. Vanhellemont, M. -A. Trauwaert, J. Poortmans,
M. Caymax and P. Clauws Thin Sol. Films 222 (1992) 166
- 5.11 G. Bremond, A. Souifi, T. Benyattou and D. Dutartre
Thin Sol. Films 222 (1992) 60
- 5.12 D. Biswas, A. Chin, J. Palmulapati and P. Bhattacharya
J. Appl. Phys. 67 (1990) 2450
- 5.13 J. F. Chen, J. C. Chen, Y. S. Lee, Y. W. Choi, K. Xie, P. L. Liu,
W. A. Anderson and C. R. Wie J. Appl. Phys. 67 (1990) 3711
- 5.14 Q-. S. Zhu, K. Hiramatsu, N. Sawaki and I. Akasaki
Jap. J. Appl. Phys. 28 (1989) L1326
- 5.15 S. R. McAfee, D. V. Lang and W. T. Tsang Appl. Phys Lett. 40 (1982) 520

- 5.16 P. S. Whitney and C. G. Fonstad J. Cryst. Growth 83 (1987) 219
- 5.17 H. Lefèvre and M. Schulz Appl. Phys. 12 (1977) 45
- 5.18 P. Omling, E. R. Weber, L. Montelius and H. M. Alexander
Phys. Rev. B 32 (1985) 6571
- 5.19 V. V. Kveder, Y. A. Ossipyan, W. Schroter and G. Zoth
Phys. Stat. Sol. (a) 72 (1982) 701
- 5.20 W. Schröter and M. Seibt J. Phys. Colloq. C4 (1983) 329
- 5.21 L. C. Kimerling and J. R. Patel Appl. Phys. Lett. 34 (1979) 73
- 5.22 H. Ono and K. Sumino J. Appl. Phys. 57 (1985) 287
- 5.23 P. Omling, L. Samuelson and H. G. Grimmeiss J. Appl. Phys. 54 (1983) 5117
- 5.24 T. Wosiński J. Appl. Phys. 65 (1989) 1566
- 5.25 A. Das, V. A. Singh and D. V. Lang Semicond. Sci. Technol. 3 (1988) 1177
- 5.26 C. Kisielowski and E. R. Weber Phys. Rev. B 44 (1991) 1600
- 5.27 C. Kisielowski, J. Palm, B. Bollig and H. Alexander
Phys. Rev. B 44 (1991) 1588
- 5.28 I. D. Hawkins PhD. Thesis (UMIST) 1989
- 5.29 E. Meijer, H. G. Grimmeiss and L. -A. Ledebø
J. Appl. Phys. 55 (1984) 4266
- 5.30 W. Kern and D. A. Puotinen RCA Review 31 (1970) 187
- 5.31 P. Y. Timbrell, J. -M. Baribeau, D. J. Lockwood and J. P. McCaffrey
J. Appl. Phys. 67 (1990) 6292
- 5.32 H. L. Fraser, D. M. Maher, R. V. Knoell, D. J. Eaglesham,
C. J. Humphreys and J. C. Bean J. Vac. Sci. Technol. B7 (1989) 210
- 5.33 P. I. Rockett and A. R. Peaker Electronics Lett. 17 (1981) 838
- 5.34 T. N. Morgan Phys. Rev. A 139 (1965) A343
- 5.35 A. G. Milnes "Deep Impurities in Semiconductors" (John Wiley & Sons Ltd
1973) 99-101
- 5.36 F. Stern Phys. Rev. B 2 (1974) 4597
- 5.37 A. Broniatowski Phys. Rev. B 36 (1987) 5895

- 5.38 Y. A. Ossipyan J. Phys. Colloq. C4 (1983) 103
- 5.39 A. Broniatowski and C. Haut Phil. Mag. Lett. 62 (1990) 407
- 5.40 E. R. Weber EMIS Datareview RN=17890 (1988) 236
- 5.41 J. Kaniewski, M. Kaniewska, W. Jung and T. Piotrowski
Phys. Stat. Sol. (a) 120 (1990) 531
- 5.42 K. Graff and H. Pieper J. Electrochem. Soc. 128 (1981) 669
- 5.43 W. Nitzsche, O. Brodersen, S. Hopfe, M. Reiche and I. Burck
Sol. St. Phen. 6/7 (1989) 49
- 5.44 S. D. Brotherton, J. R. Ayres, A. Gill,
H. W. Van Kesteren and F. J. A. M. Greidanus J. Appl. Phys. 62 (1987) 1826
- 5.45 F. D. Whitwer, H. Haddad and L. Forbes
Mat. Res. Soc. Symp. Proc. 71 (1986) 53
- 5.46 L. C. Kimerling and J. L. Benton Appl. Phys. Lett. 39 (1981) 410
- 5.47 K. V. Ravi EMIS Datareview RN=15730 (1987) 252
- 5.48 J. R. Patel and L. C. Kimerling J. Phys. Colloq. C6 (1979) 67
- 5.49 E. R. Weber Appl. Phys. A 30 (1983) 1
- 5.50 H. Bender, C. Claeys, J. Van Landuyt, G. Declerck,
S. Amelinckx and R. Van Overstraeten J. Phys. Colloq. C4 (1983) 261
- 5.51 As determined by SIMS (unpublished)
- 5.52 Y. Tokuda, N. Kobayashi, A. Usami, Y. Inoue and M. Imura
J. Appl. Phys. 66 (1989) 3651

CHAPTER 6

CONCLUSIONS AND FUTURE WORK

In this thesis, the electrical material quality of Si and Si/Si_{1-x}Ge_x/Si layers grown by MBE has been investigated with an aim to increasing our understanding of the factors limiting the material quality of both Si and the important SiGe heterosystem.

Following a period of exploratory investigation, sputtered Ti Schottky contacts were found to provide suitable rectifying barriers for the electrical characterisation of the MBE layers. However, problems associated with the fundamental material quality resulted in a dramatic increase in reverse leakage currents on extending the depletion edge through the Si/Si_{1-x}Ge_x heterointerface and into the Si_{1-x}Ge_x region. This restricted all capacitance-related measurements to the top-most Si cap - no meaningful information could be extracted on extending the depletion edge into either the heterointerfacial or bulk alloy regions. The work indicated that the source of the contamination was the Cu hearths in which the Si and Ge charges were contained. Subsequent use of liners around the Si and Ge charges prevented the indiffusion of Cu and dramatic improvements were observed in the material quality: Ti Schottky devices indicated small series resistance and low leakage (with no significant increase in leakage on extending the depletion edge into the alloy region) up to -20V reverse bias. Such devices are now of sufficient quality to allow the capacitance-related measurements to be extended into the heterointerfacial and bulk alloy regions. The large Schottky barrier height, as determined from C-V measurements, was found to be highly reproducible and stable. The exact nature of the Ti-Si contact and information on silicide formation, penetration depth of the metal into the epilayer and the extent of damage or defects induced as a result of the sputtering process could be investigated in future work.

Because interest lay primarily in capacitance-related measurements, current transport mechanisms over the Schottky barrier were not investigated in detail. Certainly, a considerable amount of information may be obtained from detailed characterisation of the forward and reverse bias I-V characteristics; the brief presentation of results and interpretation here are by no means definitive and peculiarities observed necessitate further work. However, in order to fully eliminate problems associated with Schottky barrier formation, it would be favourable to use PN junction diodes which should provide stable, very low leakage barriers and allow effects observed in the I-V characteristics, such as recombination-generation processes, to be attributed to bulk properties of the epilayers, with greater confidence.

C-V profiling allowed heterojunction features in the apparent free carrier distribution to be observed, for the first time, in Si/Si_{1-x}Ge_x/Si layers with $0 < x \leq 0.2$. Numerical integration of these profiles allowed extraction of the valence band offsets which were in good agreement with theoretically predicted values. The effect of traps were observed in both Si and Si/Si_{1-x}Ge_x/Si layers and considerable carrier compensation was apparent in the bulk regions. C-V simulations were used to reconstruct the apparent free carrier distributions, incorporating the experimentally determined valence band offsets, interface charge densities and trap distributions (as determined by DLTS). The simulations were further used to investigate the validity of numerically extracted heterojunction parameters in the presence of traps in the heterointerfacial region; the accuracy of the experimentally determined parameters was considered to be a consequence of the minimal distortion observed in the free carrier distributions as a result of the relatively low trap densities present. The extracted interface charge densities were believed to be of the fixed charge type and were acceptor-like in nature; these charge densities were seen to approximately scale with increasing Ge composition of the alloy layers. The fact that no reduction in interface charge was seen for higher growth temperature samples led to the conclusion that the origins of the electrical activity did not lie with metallic impurities, as was considered

for the deep levels observed by DLTS. Further work is required here to fully elucidate the nature and source of the interfacial charge - as the C-V technique provides a quick and easy assessment of such states, this could be readily investigated given a range of sample growth temperatures and different Ge composition. In this study, X-ray diffraction and TEM would be necessary to determine both the onset of relaxation of the metastable layers and as probes of the uniformity and integrity of the heterointerfacial and alloy regions. Thicker, uniformly doped Si buffer layers would allow an assessment of the second, deeper heterojunction, both in terms of the electrical activity of this region and the differences in band offset for increasing lattice mismatch as compared to the upper heterojunction.

Deep level distributions as determined by DLTS were complicated by the varying degrees of distortion which occurred in the deep level spectra. Clear trends were the increasing deep level concentrations on moving from the Si into the $\text{Si}_{1-x}\text{Ge}_x$ regions and a further, corresponding increase for higher Ge composition alloys. The distortion to the deep level spectra in the vicinity of the heterojunction was considered to be a result of the significant band bending which would have occurred in this region, due to the discontinuity in the valence band and the interfacial charge present. Observation of non-exponential capacitance transients initiated an investigation, via simulation, into the resultant broadening of the deep level spectra; such effects were considered in terms of carrier emission from a band of energies (as opposed to a discrete, single energy level) residing in the band-gap. Matching of the simulated and experimental deep level spectra allowed the width of the energy band to be assessed and also allowed corrections to be made to the apparent trap concentrations, which may have been underestimated. Interacting dislocation-related states have been considered to form such energy bands; the donor-like nature of the well-defined deep level features, as determined from the observed logarithmic filling and field-independent behaviour plus the reduction in deep level concentrations for higher growth temperatures or for samples subjected to post-growth anneals, suggested an interaction between point defects and

dislocations as the most probable source of the electrical activity. Both Fe and O have been identified in the MBE grown layers studied here and, in a point defect form, could interact with dislocations as suggested. However, this interpretation is not conclusive and requires further verification. Lower leakage PN devices would give access to the underlying Si buffer region, allowing deep level distributions around the second heterojunction to be fully evaluated. Different growth temperatures/anneal treatments would allow the changing electrical activity to be monitored in conjunction with structural techniques such as TEM and EPR to probe the nature of the band-gap states. Of particular interest is the deliberate contamination of Si and Si/Si_{1-x}Ge_x/Si layers with transition metals, providing information on metallic-induced band-gap states and possibly allowing comparison to the deep levels observed in this work. Further investigation of the proposed band of energies is necessary, either matching the experimental deep level spectra to simulations or via optical methods such as Photoluminescence (PL).

The findings presented in this work have gone a long way to increasing our knowledge of the MBE growth related properties of the Si/Si_{1-x}Ge_x/Si heterosystem. The use of the liners around the Ge charge dramatically reduced the Cu contamination originating from the electron beam evaporator hearth; the material quality was still impaired by the presence of Fe, which originated from the elemental Ge charge itself and is considered partly responsible for the observed electrical activity in this work. The value of this work, in routinely assessing the as-grown material, is readily apparent; further improvements may now be seen in the material quality, following the introduction of higher purity Ge, and perhaps allow better resolution of features associated with the alloy regions. Very little work had been published on the direct electrical assessment of the associated heterointerface prior to this work, suggesting the problems associated with unintentional contamination may be pervasive in other growth techniques.

APPENDIX A.

The built-in potential, $\Delta\phi$ associated with the charge dipole of the heterojunction is given by (3.38); the integral may be split into four parts thus:

$$\int_{x_1}^{x_2} p^*(x^*)x^*dx^* - \int_{x_1}^{x_2} p^*(x^*)x_I dx^* - \int_{x_1}^{x_2} N_A^*(x^*)x^*dx^* + \int_{x_1}^{x_2} N_A^*(x^*)x_I dx^* \quad (A1)$$

A B C D

The algorithms used in the integration program are as follows:

$$A: \int_{x_1}^{x_2} p^*(x^*)dx^* = \sum_{n_T=1}^{n_T-1} [p(n).x_A + p(n+1).x_B] \left(\frac{x_B - x_A}{2} \right) \quad (A2)$$

where n_T is the total number of data points between x_2 and x_1 ; $p(n)$ and $p(n+1)$ are adjacent apparent free carrier concentrations at x_A and x_B respectively.

$$B: \int_{x_1}^{x_2} p^*(x^*)x_I dx^* = \sum_{n_T=1}^{n_T-1} [p(n) + p(n+1)] \left(\frac{x_B - x_A}{2} \right) \quad (A3)$$

Combining C and D:

$$-\int_{x_I}^{x_2} N_A^*(x^*)x^*dx^* - \int_{x_1}^{x_I} N_A^*(x^*)x^*dx^* + \int_{x_I}^{x_2} N_A^*(x^*)x_I dx^* + \int_{x_1}^{x_I} N_A^*(x^*)x_I dx^* \quad (A4)$$

For a uniform doping level between the integration limits, this gives (for C and D):

$$-N_{A2} \left(\frac{x_2^2 - x_I^2}{2} \right) - N_{A1} \left(\frac{x_I^2 - x_1^2}{2} \right) + x_I [N_{A2}(x_2 - x_1)] + x_I [N_{A1}(x_I - x_1)] \quad (A5)$$

Collecting terms:

$$N_{A2}: -\frac{(x_2 - x_I)^2}{2} \quad N_{A1}: \frac{(x_I - x_1)^2}{2}$$

Thus, combining A, B, C and D allows $\Delta\phi$ to be evaluated. Similar considerations may be used to provide an algorithm for (3.40) to evaluate the interface charge density.

APPENDIX B.

MODEL I.

From (5.2):

$$\frac{dE}{dx} = -\frac{d^2V}{dx^2} = \frac{N(J)}{\epsilon_0 \epsilon_r} \quad (B1)$$

where $N(J) = N_A - N_T(J)$. In order to determine $V(J)$, the field, $E(J)$ must be found:

$$J=0: E(0) = \frac{q(N_A - N_T)L}{\epsilon_0 \epsilon_r} \quad (B2)$$

$$J=1: E(1) = \frac{qN(1)dx}{\epsilon_0 \epsilon_r} + E(0) \quad (B3)$$

The general case is given by:

$$E(J) = \frac{qN(J)dx}{\epsilon_0 \epsilon_r} + E(J-1) \quad (B4)$$

The valence band potential may be found from integration of the E-field ie. the area under the $E(x)$ curve. The area under the first increment is given by:

$$dV_{J=1} = \frac{[E(1) + E(0)]dx}{2} \quad (B5)$$

and the area under the Jth increment is:

$$dV_J = \frac{[E(J) + E(J-1)]dx}{2} \quad (B6)$$

Thus, the valence band potential at $J=1$ is: $V(1) = V(0) + dV_{J=1}$

and at the Jth point: $V(J) = V(J-1) + dV_{J=1}$

Hence, the potential at each point J may be found according to the corresponding space-charge density, $N(J)$ which will feature contributions depending upon the number of filled and empty traps.

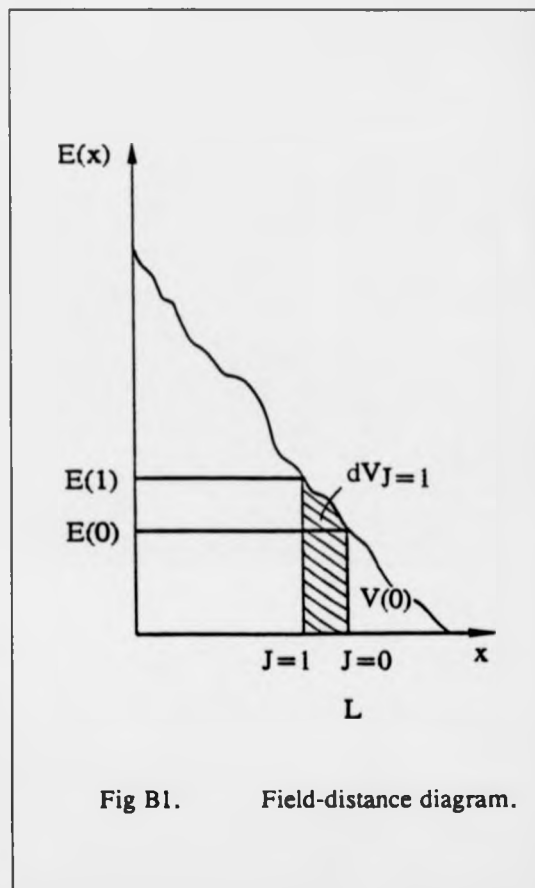
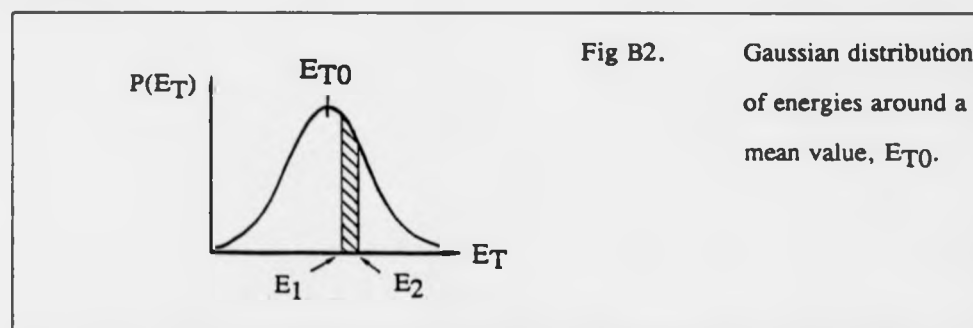


Fig B1. Field-distance diagram.

MODEL II.



The weighting function is obtained by determining the shaded area shown in Fig B2. for an incremental step, dE between E_1 and E_2 (where $E_2 = E_1 + dE$). Note the function $P(E_T) \rightarrow 0$ for $E_T > E_{T0} + 3\delta$ and $E_T < E_{T0} - 3\delta$. This area beneath the Gaussian distribution is given by:

$$P(E_1 < E_T < E_2) = \int_{E_1}^{E_2} \frac{1}{\sqrt{2\pi} \cdot \delta} \exp\left[-\frac{(E_T - E_{T0})^2}{2\delta^2}\right] dE_T \quad (B7)$$

From (B7):

$$P(E_{T0} - 3\delta < E_T < E) = \int_{E_{T0}-3\delta}^E \frac{1}{\sqrt{2\pi} \cdot \delta} \exp\left[-\frac{(E_T - E_{T0})^2}{2\delta^2}\right] dE_T \quad (B8)$$

which may be determined numerically [B.1]:

$$P(E_{T0} - 3\delta < E_T < E) = 1 - \text{INT} \cdot (C1 \cdot T1 + C2 \cdot T1^2 + C3 \cdot T1^3 + C4 \cdot T1^4 + C5 \cdot T1^5) \quad (B9)$$

where $\text{INT} = \frac{1}{\sqrt{2\pi} \cdot \delta} \exp\left[-\frac{(E_T - E_{T0})^2}{2\delta^2}\right]$, $T1 = \left[1 + P\left(\frac{E_T - E_{T0}}{\delta}\right)\right]^{-1}$ and coefficients

$P=0.2316419$, $C1=0.31938153$, $C2=-0.356563782$, $C3=1.78147937$, $C4=-1.821255978$ and $C5=1.330274429$. Clearly:

$$P(E_1 < E_T < E_2) = P(E_{T0} - 3\delta < E_T < E_2) - P(E_{T0} - 3\delta < E_T < E_1)$$

and hence, the strip area may be evaluated. Note this analysis is only valid for $E > E_{T0}$, but because of the symmetry of the Gaussian distribution, the weighting functions for $E < E_{T0}$ are readily determined.

References

B.1 CASIO fx 4500P Owners manual 136